Adaptive Optoelectronic Systems: From Bio-Sensing to Free-Space Optical Communication

Thesis by

Fatemeh Aghlmand

In Partial Fulfillment of the Requirements for

the Degree of

Doctor of Philosophy

CALIFORNIA INSTITUTE OF TECHNOLOGY

Pasadena, California

2024

Defended July 17, 2023

Fatemeh Aghlmand
ORCID: 0000-0002-5103-9314

To my parents

for their never-ending sacrifice, love, support, and belief in me.

ACKNOWLEDGEMENTS

My path to this point in my academic journey has seen many turns and starting overs. Even though the unpredictable life events sometimes made me hopeless in continuing this journey, my passion for electronics and its fascinating applications and the support of my wonderful family, friends, and advisor gave me the strength to never give it up.

I feel very fortunate and appreciative to Prof. Azita Emami for giving me a chance and for her trust in me. I cannot thank her enough for all of her support when I needed it the most. I never forget that when I was in a difficult family situation back in Iran and didn't think I could return to Caltech, I received an email from her telling me to stay strong and she would help me in any way she could. I am eternally grateful to her for giving me a chance for a new life. She has been a strong role model for me, and I have learned a lot from her both on the technical and personal levels. I am also extremely honored and grateful for our fruitful collaboration with Prof. Richard Murray. The opportunity to work on the Silicon-Cell project under the guidance of Prof. Murray and Prof. Emami gave me the courage to face new challenges, learn new subjects, and appreciate the beauty of combining several disciplines of science to create solutions for issues that are of great importance for both human and the environment. This wonderful collaboration has broadened the horizons of my knowledge of biomedical applications that can benefit from advanced integrated circuits and systems.

I am honored to have Prof. Richard Murray, Prof. Alireza Marandi, Prof. Axel Scherer, and Prof. Mohammad Mirhosseini on my Ph.D. defense/candidacy committee. Not only do I greatly appreciate their participation in examining my research work, but I also have always looked up to them in light of their dedication and contributions to the future of science and engineering. Looking further back, I must express my gratitude to my professors over the years who taught me that being smart without being hardworking and dedicated never succeeds. I especially would like to mention Prof. Omid Shoaie of the University of Tehran, who initiated a passion and love for electronics in me.

Caltech and Mixed-mode Integrated Circuits and Systems (MICS) Lab feels like home for me. I made friends who are like my family, and I know that whenever I face a challenge,

they are there for me. I know how rare this is and how fortunate I am to be part of this wonderful group. I like to thank Arian Hashemi, Steven Bulfer, Shawn Sheng, Ting-Yu Cheng, Hayward Melton, and Krishna Pochana for their friendship. I must express my gratitude and appreciation to my wonderful friend and lab-mate, Saransh Sharam, who was there for me from day one of our Ph.D. journeys.

Lastly, my gratitude to my parents, sisters, nieces, and nephews never be sufficient. Their endless and unconditional love is simply the best part of my life and has made the best part of me. During my studies at Caltech, I lost my dearest dad to Alzheimer's. Until the last moment he could talk to me, he was looking forward to seeing me achieving this goal, and I am sure he is still with me.

ABSTRACT

Portable and point-of-care medical devices are becoming an essential part of today's medical technology. An affordable personal device that can diagnose and monitor a medical condition in real-time will improve the patient's life quality in many ways. Additionally, by autonomously providing the suitable treatment, a universal healthcare device can be accessible to most of the population at a low cost. Despite considerable efforts and great outcomes, most of the prior arts in realizing these devices have limitations that hinder their widespread use in portable applications. On the other hand, comprehensive environmental sensing has drawn great attention in the last few years. Monitoring the quality of water, soil, air, and waste is of utmost importance to study their effect on human life and also to recognize the consequence of human actions on the planet.

The most important factors in developing a compact and portable device for medical and environmental applications are their integration level, ease of use with biomarkers, and reliability of the results. Detecting a specific chemical in the biology world relies on a biochemical reaction with a transducer that can convert the resulting signal into a measurable signal in various modalities, such as electrical, magnetic, or optical. Hence, the biosensing device is often a multidisciplinary apparatus that is not readily integrable due to the need for miniaturizing otherwise bulky optical or magnetic components. The key requirement in device miniaturization, though, is to use standard technologies to avoid extra cost and processing time for the device's mass production. The path towards achieving such a device needs revisiting the existing solutions and the capabilities of the powerful yet affordable CMOS technologies to seamlessly integrate various device components, namely electronics, biology, and optics/magnetics. This dissertation provides an overview of integrated biosensors and presents novel designs in optics and electronics to implement a fully integrated and miniaturized device for medical and environmental applications.

Fluorescence sensing is one of the most reliable and widespread detection methods with well-established tools in synthetic biology. Specifically, bacterial-based fluorescence sensors offer unsurpassed advantages to labeled detection since bacterial cells, when engineered, can

respond to various elements in their surroundings at a low cost and quite efficiently. The use of live bacterial cells is also of great importance in establishing the bidirectional link with the CMOS device. By monitoring the dynamics of the cells' growth and their protein expression, a desired biology response can be initiated upon receiving the stimulating signal from the device. The conventional methods in fluorescence sensing involve an elaborate setup with many external optical components unsuitable for portable and *in vivo* applications. Hence, integrating silicon chips and live bacterial biosensors in a miniaturized "Silicon-Cell" system can enable a wide range of applications for both sensing and remediation. Such integrated systems need on-chip optical filtering in the wavelength range compatible with fluorescent proteins, which are widely used signal reporters for bacterial biosensors.

In the first part of this dissertation, we introduce a fully integrated fluorescence sensor in 65nm standard CMOS process comprising on-chip bandpass optical filters, photodiodes, and processing circuitry. The metal/dielectric layers in CMOS are employed to implement low-loss cavity-type optical filters, achieving a bandpass response at 600/700nm range suitable to work with fluorescent proteins. The sensitivity of the sensor is further improved in the electrical domain by using a C-TIA with variable switched capacitor gain, a voltage-controlled current source (VCCS), and feedback-controlled low-leakage switches, resulting in a minimum measured current of 1.05fA with SNR >18dB. The sensor can measure the statics/dynamics of the fluorescence signal as well as the growth of living *E. coli* bacterial cells. Using a differential design and layout, the sensor can distinguish two biochemical signals by measuring two fluorescent proteins encoded in a single bacterial strain. Furthermore, a proof of concept is demonstrated to establish bidirectional communication between living cells and the CMOS chip, using a fluorescent protein regulated by an optogenetic control.

In the second part of this dissertation, we describe a fully integrated high-bandwidth optical receiver for RF-over-free-space optics (RoFSO). This work is motivated by the availability of a wide, unregulated bandwidth at the optical frequencies and the lower cost and setup time due to using atmosphere instead of fiber optics as the communication channel. Nonetheless, the atmospheric link poses serious challenges, including severe beam intensity and phase

distortions. Here we present novel solutions at the system and circuit level to make the receiver adaptive and resilient to the mentioned distortions. The chip is designed and implemented in a 28nm CMOS process, and it is shown to achieve a measured gain of 58dB and bandwidth of 18GHz. The link performance is assessed by exposing the system to more than 26dB of optical loss, equivalent to 3.5km of free space distance under moderate visibility conditions. For a proof-of-concept demonstration, an 8Gbps non-coherent DPSK signal with an RF bandwidth of 10GHz is transmitted, resulting in a BER of 1×10^{-4} for a minimum received power of -30dBm and while consuming 19.2mW power at the receiver.

PUBLISHED CONTENT AND CONTRIBUTIONS

F. Aghlmand, C. Hu, S. Sharma, K. Pochana, R. M. Murray, and A. Emami, "**A 65nm CMOS Fluorescence Sensor for Dynamic Monitoring of Living Cells**," in *IEEE J. Solid-State Circuits (JSSC)*, Invited paper (accepted).

F. A. participated in conceiving the ideas, was the lead designer of the CMOS chip, performed all the experiments, and co-wrote the manuscript.

F. Aghlmand, C. Hu, S. Sharma, K. Pochana, R. M. Murray, and A. Emami, "**A 65nm CMOS Living-Cell Dynamic Fluorescence Sensor with 1.05fA Sensitivity at 600/700nm Wavelengths**," in *IEEE Int. Solid-State Circuits Conf. (ISSCC)* Dig. Tech. Papers, Feb 2023, pp. 311–313. https://doi.org/10.1109/ISSCC42615.2023.10067325

F. A. participated in conceiving the ideas, was the lead designer of the CMOS chip, performed all the experiments, and co-wrote the manuscript.

F. Aghlmand, S. Sharma, and A. Emami, "**An 8Gbps Adaptive Receiver for RF over FSO in 28nm CMOS**," in *2020 15th European Microwave Integrated Circuits Conference (EuMIC)*, Jan. 2021, pp. 49-52. https://ieeexplore.ieee.org/document/9337441

F. A. participated in conceiving the ideas, was the lead designer of the CMOS chip, performed all the experiments, and co-wrote the manuscript.

TABLE OF CONTENTS

LIST OF ILLUSTRATIONS

Number *Page*

LIST OF TABLES

Number *Page*

Chapter 1

INTRODUCTION

Nowadays, biosensors are a ubiquitous part of our everyday life. They are used in a wide range of applications, including but not limited to detecting a specific substance in our bodily fluids' samples (blood, urine, saliva, etc.), diagnosing a medical condition, monitoring the quality of food and air, and sensing a specific biological/chemical reaction in drug discovery research. The development of these devices in an efficient and small form factor has been the focus of extensive research in the last decade. This chapter will introduce biosensors and their main components and discuss their two main applications.

1.1 Biosensors

The International Union of Pure and Applied Chemistry (IUPAC) defines a biosensor as "A device that uses specific biochemical reactions mediated by isolated enzymes, immune systems, tissues, organelles or whole cells to detect chemical compounds usually by electrical, thermal or optical signals" [1]. As shown in Figure 1.1, the biosensor's major components are analyte, bioreceptor, transducer, and electronics. An analyte is a substance of interest that needs to be detected in various environments. It can be the Phosphorus (P) in the soil to inform us of the required fertilization for healthy plant growth, or Thiosulfate (ThS) in our gut to alarm us of the gut inflammatory disease, or Arsenic (As) in our everyday water intake that can be fatal [2].

The next component in the biosensor is called the bio-recognition element or bio-receptor, a molecule that can recognize the analyte of interest. Proteins, enzymes, deoxyribonucleic acid (DNA), and cells are popular bio-receptors. Interaction of these elements with the analyte can generate a signal in various modalities, such as optical, electrical, or chemical domains in the process named bio-recognition. Then, a transducer converts the resulting signal into a measurable signal, commonly an electrical voltage or current. In the end, the low-level analog signal from the transducer is amplified, filtered, and digitized to be displayed.

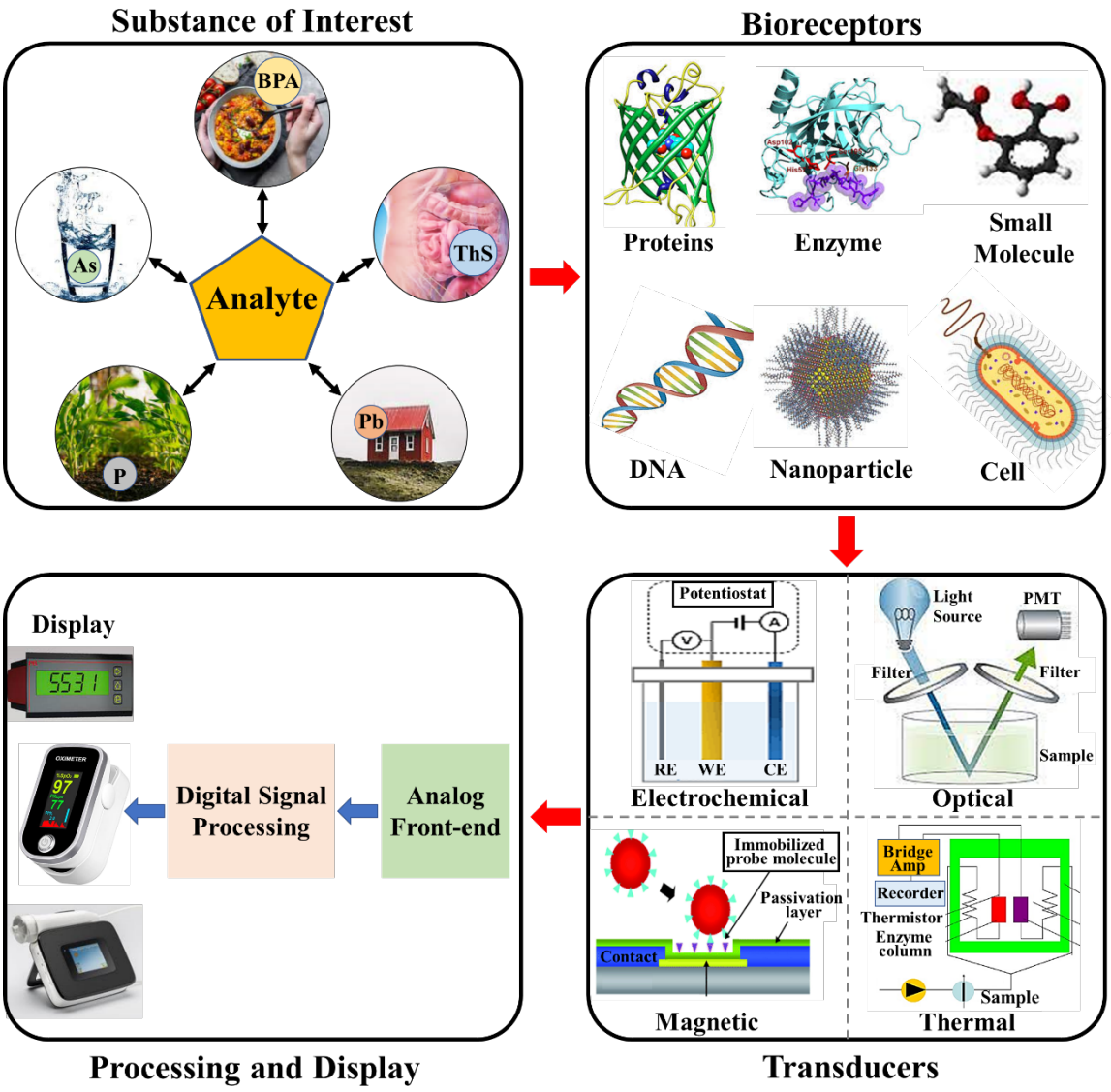

Figure 1.1: An overview of the biosensing process: the bio-recognition elements are extracted from various types of bio-samples, and subsequently transduced into various types of signals.

Based on their principle of bio-recognition, biosensors can be categorized as catalytic-based or affinity-based (Figure 1.2). In a catalytic biosensor (such as glucose sensing), an enzyme is used to convert a substance into a product, and a transducer detects the formation of this product. In an affinity sensor (such as DNA and antibody sensing) in a process called selective binding, a complementary capture probe is used to capture the target analytes since

it has a much higher affinity to the target than other interfering molecules [3]. After capturing the target analyte, a transducing method in either labeled or label-free form is used to read the associated signal. Fluorescent and magnetic tags are popular choices in labeled detection. They are added to the liquid solution and, by a diffusion process, bind to the target-capture pair on the surface. In the label-free case, the solution's altered electrical characteristic due to the analyte-capturing process is detected. Though direct and straightforward, this method is less sensitive than labeled detection.

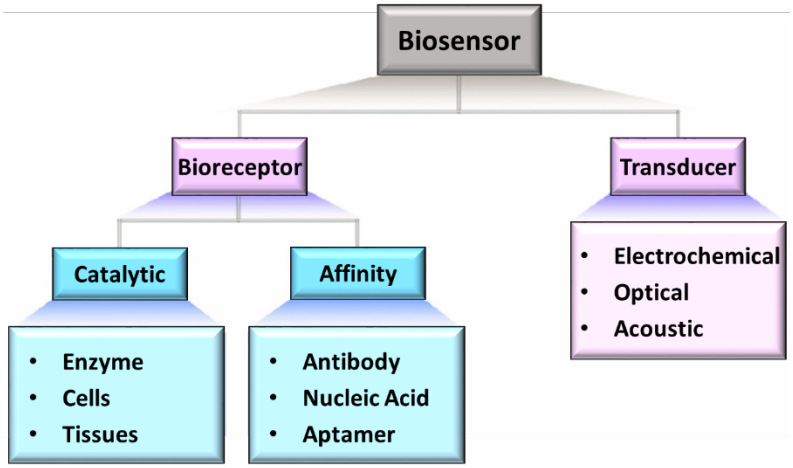

Figure 1.2: Biosensors categories based on principle of the bio-recognition process.

1.2 Personal, Portable Healthcare

Even though developing a portable, personal health monitoring system has been the focus of extensive research efforts in the last decade, the advent of the pandemic and its overwhelming effects on the healthcare system has expedited these efforts. Other than the concern of fast access to a reliable and real-time diagnosis, the cost of such access is a significant factor in today's devastating economy. Developing countries, conflict zones, and areas facing natural disasters can specifically benefit from such low-cost and accessible devices. On the other hand, chronic diseases such as heart disease, cancer, and diabetes are among the most demanding conditions requiring ongoing medical attention, limited daily activities, or both. As the leading causes of death and disability in the United States [4], patients with these

chronic diseases periodically undergo clinical monitoring, generally through laboratory procedures costing both time and money.

Therefore, creating bio-molecular sensors to perform minimally invasive health monitoring and point-of-care diagnosis is a solution that can revolutionize personalized medicine. An efficient biosensor includes various parts and is a multidisciplinary device combining elements of biochemistry, nanotechnology, photonics, and electronics. The continuous advances in these fields have encouraged researchers to propose new techniques and sensing modalities for diverse applications. For instance, nucleic acids and proteins are powerful bio-elements that can be used for detecting HIV, tumors, cancers, gut, or cardiovascular diseases, etc. Hence, developing a device that can efficiently work with these bio-elements is essential in realizing a comprehensive personal healthcare device. [5].

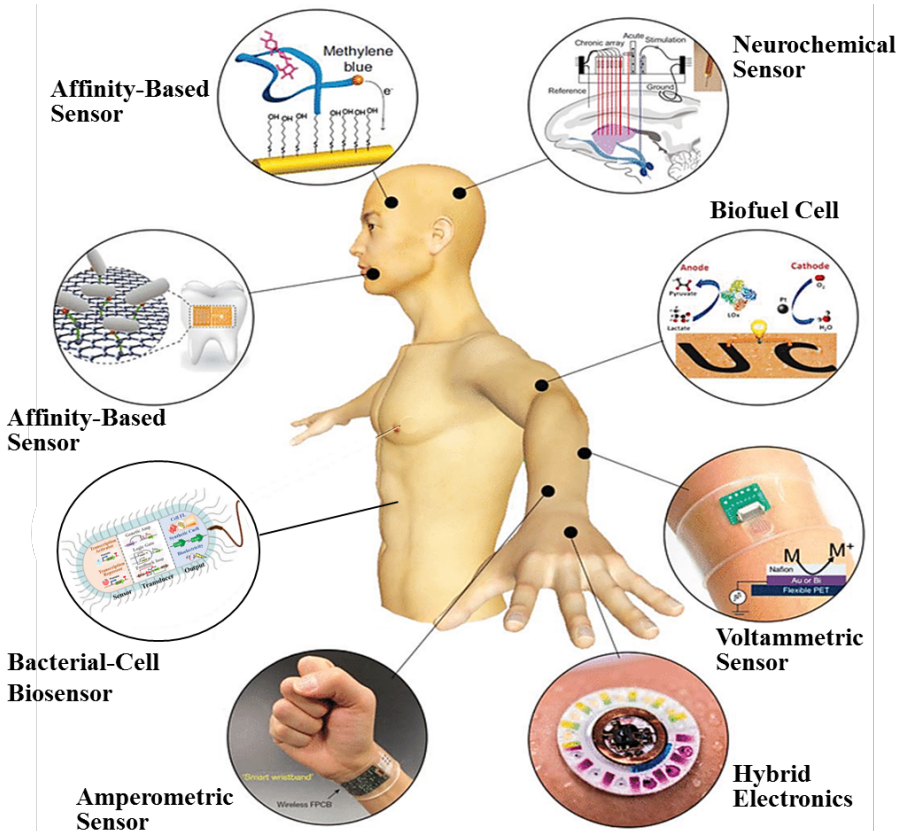

Figure 1.3: Multiple variation of wearable biosensing devices for portable healthcare [6].

Figure 1.4: Several categories of environmental monitoring.

1.3 Environmental Monitoring

The undeniable impacts of climate change worldwide have put a great demand on finding solutions to protect our environment. While, as per IPCC's (The Intergovernmental Panel on Climate Change) assessment report, many countries are struggling to be prepared for climate impacts, the efforts for environmental monitoring have been accelerated [7]. Continuous environmental monitoring can help us understand the environment's complexity and the harmful effects of human activity on it, leading to improved life quality for the present time and effective planning for the future.

There are several categories of environmental monitoring, including air, soil, water, waste, etc. Soil monitoring has drawn considerable interest in the last few years. The health of soil affected by climate change, water shortage, and vulnerable ecosystems is of great importance now more than ever. Establishing the tools for real-time soil monitoring enables managing soil moisture and fertilization needed for the plant's growth and helps us better understand

water resources locally and regionally. For instance, plants such as wheat are grown in large fields, and their healthy growth strongly depends on Phosphorus (P) availability, which needs to be measured close to the plant's roots. Conventionally, random soil samples are taken to the laboratory for a point measurement of the P level in the soil. Based on the results, a decision on fertilizing the field is made. This process is non-optimum in cost, time, and precision. A biosensor packaged in a small form factor can be buried under the soil to monitor the points in the field in real-time. An array of sensors connected to the cell tower can cover the whole field and indicate the areas lacking the P for optimum and adequate fertilization.

1.4 Contributions

In this dissertation, we propose novel approaches to miniaturize and integrate optical/electrical components required in a biosensing device specifically for biomedical and environmental applications. In particular, we demonstrate a fully integrated bacterial-based fluorescence sensor without any external passive optics other than mm-sized SMD LED sources for excitation. This is achieved by manipulating electromagnetic fields to realize optical filtering using nanostructures in the standard CMOS process. This level of miniaturization enables the device to fit in a small pill for *in vivo* use, opening a new class of opportunities and applications.

The complete integration of the fluorescence sensor is achieved by taking advantage of the standard CMOS process as a robust and efficient platform to co-design the optical and electrical functions. Using available metal routing layers in the CMOS, plasmonic-based bandpass optical filters in the visible wavelength range of the spectrum are achieved. This specific wavelength range is critical in empowering the sensor to use engineered bacterial cells as natural biosensors, reducing the biology side's complexity, and expanding the device's capabilities. The seamless integration of optical/electrical parts in a single chip is advantageous in providing additional filtering (other than optical filters) since the fundamental limitations of the available materials for filter implementation avoid achieving the needed extinction ratio solely using optical filters.

We show that another level of filtering can be achieved by designing a bandpass photodiode using the silicon's wavelength-dependent absorption length. A triple-junction vertical photodiode is designed to specifically collect the minority carriers generated due to photon absorption at the desired depth in the substrate. In the circuit design domain, we use the concept of common-mode rejection in the differential design to remove the remaining excitation light that reaches the detector. Several circuit techniques are used, including low-leakage switch implementation, high adaptive gain capacitive TIA, and correlated double sampling.

We present extensive biological experiments to show the capability of our device in not only detecting fluorescence signals of engineered bacterial cells but also in communicating with these living cells. This bidirectional communication with cells enables various controlling functions in a biological process. We show that the dynamics of cell behavior, both in terms of their growth and protein production, can be monitored and modulated via optical signaling.

Furthermore, this thesis presents a wide-dynamic range adaptive receiver for RF over free-space optical communication. The prototype chip is designed and implemented in a 28nm CMOS process. It includes several automatic controlling loops to compensate for the severe distortions in the signal due to atmospheric channels. We show that choosing the suitable modulation type in both RF and optical domains allows the receiver to be free from heavy digital signal processing, making it low power and cost.

1.5 Organization

This thesis is organized as follows. Chapter 2 briefly reviews the basics of the common modalities used in biosensing devices and discusses prior art challenges in integrating the sensors. Fluorescence sensing is introduced as one of the most common and reliable sensing methods. The advantages and applications of a bacterial-based fluorescence sensor for biomedical and environmental applications will follow.

Chapter 3 introduces the overview of the proposed Silicon-Cell system as a miniaturized device to facilitate bidirectional communication between live cells and the CMOS chip. To prove the concept, we will show the experiments' results of a handheld prototype device. Furthermore, the theoretical analysis of the system and its components is discussed, including the fundamentals of optical resonances to create integrated optical filters. The design and implementation of the integrated sensor are described in chapter 4. Concepts and design insights on the optical and electrical domains are discussed, and simulation results are shown. Chapter 5 presents the fabricated Silicon-Cell chip's characterization and measurement results, including optical/electrical and biological experiments. The results show that we could achieve a sensitivity of 1.05 fA with more than 18dB SNR while integrating the signal for 1 sec.

In chapter 6, we move from integrated medical devices to integrated receivers for communication to discuss a fully integrated RF over free space optics (FSO) receiver in a 28nm CMOS process. The system's requirements and overall architecture are shown along with the simulation and measurement results. Conclusions of the work and future directions are given in chapter 7.

Chapter 2

BACKGROUND

In this chapter, we review the operation of biosensors in the common modalities and their integration and miniaturization challenges. Bacterial-based biosensors are introduced next to be used specifically in the optical domain. A description of the main signal reporters for these sensors, namely fluorescent and luminescence proteins, will follow. We conclude the chapter by mentioning the promising applications and benefits of an integrated cell-based biosensing device.

2.1 Integrated Biosensors

In the current era of smart healthcare, there is a rising demand for portable, low-cost, and personal wearable biosensing devices that can continuously monitor, detect, and analyze biological signals essential for the early diagnosis of diseases. As such, bioelectronics has seen considerable advances in realizing miniaturized biosensing devices, mainly using CMOS technology for a low-cost and portable solution. Figure 2.1 shows some of these recent efforts in transforming complex bulky setups to fully integrated solutions, mainly in optical and magnetic modalities.

The choice of the bio-detection method, specifically for affinity-based sensors, depends on whether the labels are used or not. In the label-free technique, the biochemistry transduction is detected by measuring the electrical properties of the solution using impedance spectroscopy, dielectric measurement, or electric potential read-out (electrochemical). On the other hand, in labeled detection, magnetic or fluorescent labels can cause a slight variation in the electromagnetic fields near the sensing device, which is then read out by electronic circuitry. In what follows, we briefly review some of the most popular methods for biosensing and the prior efforts in integrating them using CMOS technology.

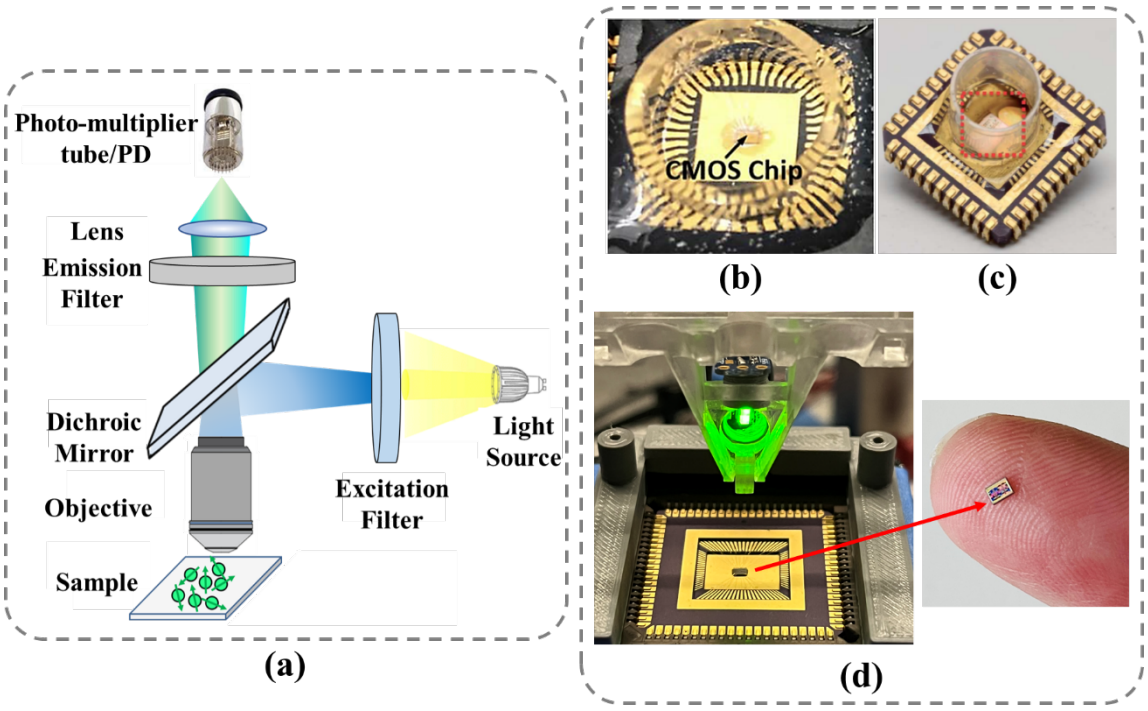

Figure 2.1: (a) A typical commercial fluorescence-based microarray reader. (b) Prior art on integrating fluorescence sensing in CMOS process [8]. (c) Prior art on integrating magnetic sensor in CMOS process [9]. (d) This work demonstrates extreme miniaturization of a fluorescence biosensor to mm-sized CMOS chip.

2.2 Electrochemical Biosensors

One of the popular label-free biosensing devices is the electrochemical sensor which directly converts a bio-recognition process into a measurable signal in the electrical domain. This sensor works based on the principle that through binding reactions biomolecules consume or generate ions or electrons that will change the electrical properties of the solution, which can be detected using conductive and chemically stable electrodes [10].

An electrochemical cell includes three types of electrodes: working electrode, reference electrode, and counter or auxiliary electrode, commonly made from platinum, gold, or carbon (graphite) (Figure 2.2). The bioreceptor is immobilized on the working electrodes to capture the analyte in the liquid solution. The reference electrode is kept away from the

reaction location to keep its potential at a known stable level. The role of the counter electrode is to provide a connection to the electrolyte solution such that electrical charges resulting from the binding process can flow to the working electrode. Based on the implementation, the electrochemical sensor can be categorized as potentiometry, voltammetry, or impedance spectroscopy [11].

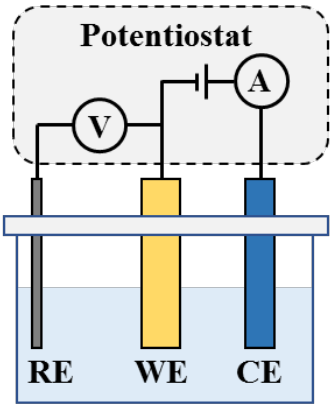

Figure 2.2: Principle of electrochemical detection. Each electrochemical cell includes three electrodes: working electrode, reference electrode, and counter or auxiliary electrode.

Electrochemical biosensors, while simple and direct, have several drawbacks. Since the only available exposed metal in the standard CMOS process is the aluminum bonding layers, integrating these sensors in CMOS requires post-processing steps to implement the electrodes with suitable meals (Au, Pt). These post-processing steps are complicated and add extra cost to the sensor. Furthermore, due to the background noise, offset, and biological shot noise resulting from the hybridization process, the detection limit of these sensors is significantly higher than fluorescence and magnetic sensors [12].

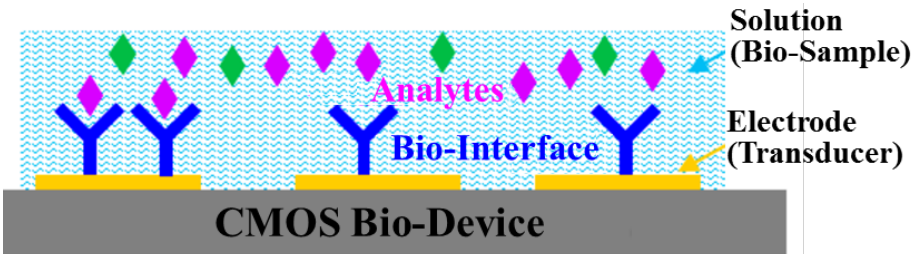

Figure 2.3: A generic schematic of a typical electrochemical sensor implemented in the CMOS process [13].

2.3 Magnetic Biosensors

Magnetic sensors are commonly labeled biosensors that can achieve high sensitivity. The unique properties of magnetic materials, such as paramagnetic or super-paramagnetic particles, are used to develop these sensors. In principle, the magnetic sensor works by detecting the induced changes in the solution's magnetic properties (coil inductance, resistance, or magneto-optical properties) due to biological interactions. The nanometer size particles in these sensors are coated in the bioreceptor (antibody, nucleic acid, etc.), and upon interaction with the target, their physical properties change. Several techniques, including coils, Hall effect devices, giant magnetoresistance (GMR) devices, and imaging, are used to detect the mentioned changes [14].

Magnetic biosensors can accelerate the binding interaction by manipulating the paramagnetic particles in a magnetic field. This will move the particles to the sensor surface where the interaction is happening, speeding up the detection of the target. Since the biological samples usually do not contribute to the magnetic signals (compared to the magnetic particles), these sensors may have a high signal-to-noise ratio.

The early development of these sensors needed an externally generated magnetic biasing field which increased their size and cost and limited their usage in portable health monitoring applications. [15, 16, 17, 18, 19]. In a more recent implementation [9], researchers employed a frequency-shift detection method where a free-running resonator is built using an on-chip LC tank. Then, by passing an AC current through the inductor, a magnetic field is created, which in turn interacts with the magnetic labels. This reaction causes a subtle increase in the inductance value lowering the LC tank's resonance frequency. This slight shift in the oscillation frequency is detected and correlated with the number of magnetic beads (Figure 2.4).

Although fully CMOS integrated, this implementation suffers from the following drawbacks. For accurate measurements, the oscillation frequency needs to be very stable with variations in time and temperature. While for temperature stabilization, the sensor can be left to warm up for some time (30 min) before the measurements, a more complex

solution handles the sensor's drift in time. A correlated double sampler circuit was applied, with the first measurement performed right after the assay and the second after all the magnetic beads were either manually removed from the chip or manually "frozen" by placing a permanent external magnet nearby.

The signal strength in these sensors is directly related to the size of the beads, meaning that smaller particles result in lower SNR. On the other hand, since the size of most common bio-receptors is in the nm range, using large beads in biological assays is not desirable as it can result in non-specific binding to the various substrate and non-optimum binding of the beads. Therefore, there is a tradeoff in choosing the size of the beads relative to the size of typical bio-receptors.

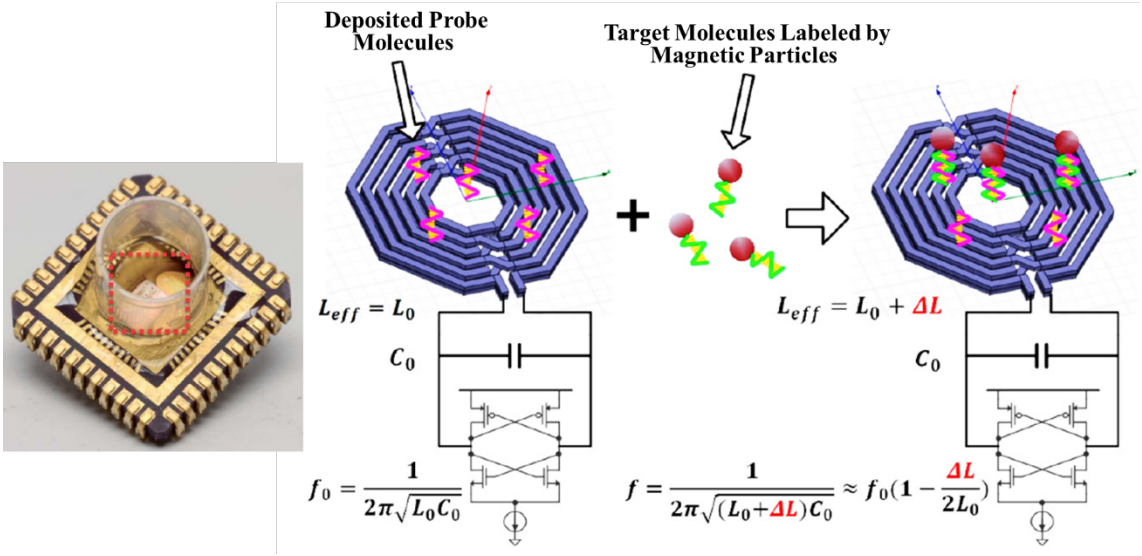

Figure 2.4: A frequency-shift-based magnetic biosensor implemented in the CMOS process [9].

2.4 Optical Biosensors

Optical biosensors are the most common sensors in biomedical research and diagnostics. They offer high sensitivity and specificity, and more importantly, they benefit from well-developed biochemistry. Over the last decade, advances in several fields of science, including integrated circuits, microelectromechanical systems (MEMS), nano-optics,

molecular biology, and biotechnology, have been driving great efforts in the research and development of new technologies for optical biosensors [20]. These biosensors are powerful tools for measuring both catalytic and affinity reactions. In the catalytic case, they can measure a change in the emitted or absorbed light caused by the products generated due to the catalytic reaction. On the other hand, affinity reactions can measure the induced changes in the optical properties of the sensor surface due to the binding process [21].

Implementing a miniaturized system using CMOS technology to read out and process a weak optical signal from these sensors is challenging as they often need to include on-chip optical elements. The only readily available optical component in the standard CMOS process is the photodiode which converts the optical power to an electrical current. Since the most common optical biosensors need an excitation source, high-performance optical filters and collimators are required to separate and focus the emission light from the bio-element.

The researchers in [22,23,24] present systems with optical components being externally grown on top of the CMOS chip. Specifically, in [22], the researchers have shown the fabrication of passive optical elements on the surface of the CMOS chip. An optical interference-based thin film filter including 20 layers was grown on top of a 56-pixel CMOS image sensor to work as an emission filter. The excitation light was provided by a laser source emitting perpendicular to the chip surface. Also, an extra fiber optical faceplate was used to improve the collimation to reduce the laser source scattered light due to the CMOS chip's bonding wires and pads. Such a system, even with acceptable performance, involves heavy post-fabrication steps and additional external optical components, which limits their use in low-cost and portable applications.

In a novel approach, researchers in [8] demonstrated a single-chip device able to detect the fluorescence response of quantum dots (QD) with high sensitivity. This fluorescence sensor integration in the CMOS process is accomplished by realizing on-chip high-pass optical filters using metal routing layers. By designing a very dense array of metallic structures and relying on copper's different intrinsic loss for 400nm vs. 800nm, the high pass behavior

for the filters is achieved. Since the physical mechanism of the filters is not based on any optical resonance, the filters are very robust against variation in the process and angle of incoming light. Being one-dimensional, the filters are not polarization-insensitive since they are designed to obliterate the TE polarization, reducing the filter efficiency (Figure 2.5). The high extinction ratio of this sensor mainly results from optical filtering, which makes the working range of the sensor quite limited. On the other hand, even though QDs are bright, durable synthetic labels, being inorganic, they are unsuitable signal reporters for living cells. Therefore, as the reported wavelength range of this work is limited to the very high end of the visible spectrum (800nm), this sensor is not equipped to work with fluorescent proteins, which are between 400nm -700nm [25].

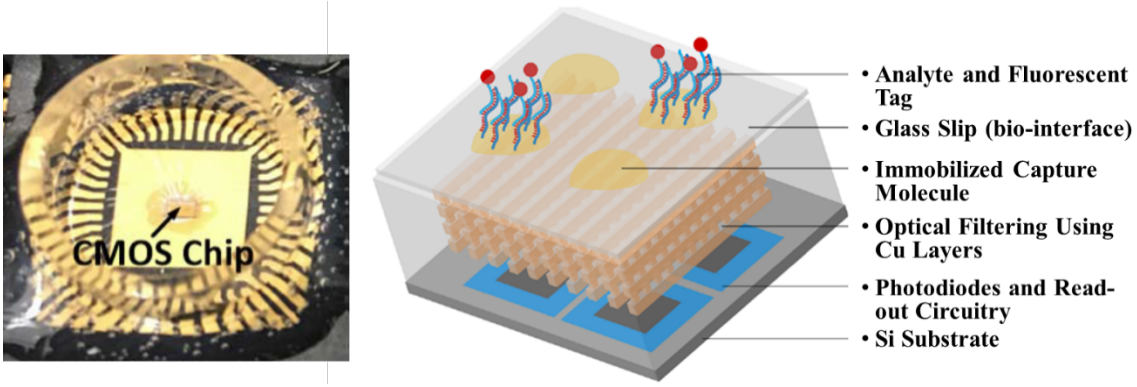

Figure 2.5: A Single-chip fluorescence sensor with high-pass on-chip filtering implemented in the standard CMOS process [8].

Another considered technique to implement a CMOS optical biosensor uses time-resolving measurements with synchronized sources [26, 27, 28, 29]. When fluorophores are excited by a source, they start to emit light. If the excitation light turns off, the fluorophores continue to emit exponentially decaying light for a limited time. This time is called the characteristic lifetime and is in the range of 1-10ns (Figure 2.6). The general idea is to employ a fast pulse laser source for excitation. With picosecond range turn-off time for the laser, a fast photodetector can be enabled to start integrating light right at the beginning of the fluorescence decay time. This method facilitates measuring only the emitted light from the fluorophores and removes the emission filter requirement. Work in [26] shows

implementing this method in an imager array. Using a picosecond laser source system, they have demonstrated an impulse response time constant of 800ps for the photon sensing and processing circuitry and better than 150ps timing resolution.

This time-based method can be complicated and costly due to the need for high-speed and power-hungry driving circuitry, high-accuracy timing synchronization, a high-speed photodetector, and an expensive sub-ns pulsed laser. Additionally, since the lifetime of fluorophores is in the ns range, the integration time for the photon detection in this method is severely limited compared to the fluorescence sensors employing filters, which enables integrating the weak signal up to the sec range.

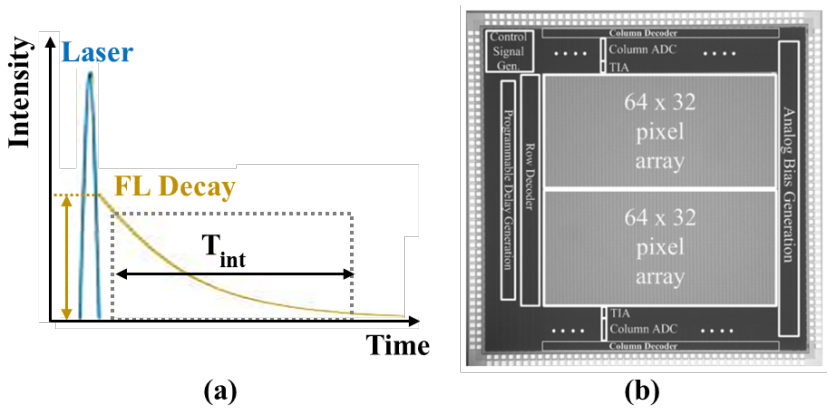

Figure 2.6: (a) Concept of fluorescence detection using time-resolving technique. (b) Prior work of miniaturized fluorescence sensor utilizing filter-less time-gated approach [26].

2.5 Bacterial-Based Biosensing

As we have seen up to now, traditional biosensors heavily rely on biochemical reactions with a transducer that converts the chemical signal into a measurable signal in the electrical, magnetic, or optical domains [8,9,30,31,32]. Incorporating biochemical components within a transducer is often challenging and costly. Bacterial cells, on the other hand, are natural biosensors due to their ability to respond to the changes in their environment, ranging from our gut to our houses [33,34,35,36,37] (Figure 2.7). These cells have evolved to detect and respond to various chemical and physical signals in their surroundings, such as nutrient availability, temperature, and pH.

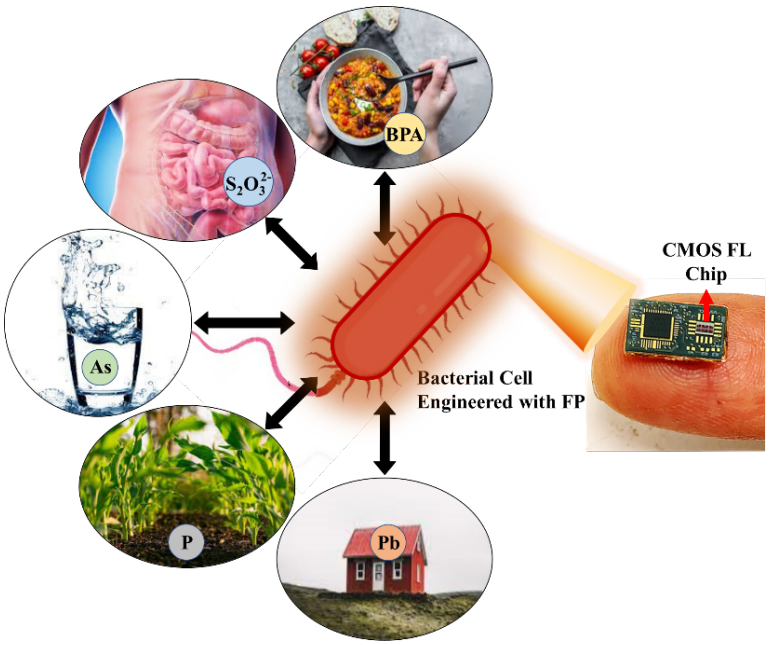

Figure 2.7: Applications of a bacteria-based integrated CMOS fluorescence sensor for detecting biochemicals in various environments.

The first kind of cell-based biosensors [38] coupled the cell's respiratory activity changes with an electrochemical transducer to measure these phenomena within the cell. While the early cell-based biosensors offered a more cost-efficient solution than enzyme-based sensors, their lower sensitivity hindered their widespread use until recombinant DNA technologies were introduced. Researchers then used these new powerful tools to engineer micro-organisms with various proteins of interest to generate a measurable signal in response to the target analytes.

Returning to the definition of a biosensor as a device that includes a biological sensing element (bio-receptor) and a transducer, we see that bacterial cells can be considered natural biosensors (Figure 2.8). They are capable of integrating the sensing elements with a transducer to directly convert the recognition event into a measurable output for detecting a target molecule(s). The bacteria cells mostly execute this task through specialized receptor proteins located on the cell surface. When these receptors interact with their corresponding ligands, they trigger a signaling cascade within the cell, leading to a cellular response [39].

Specifically, the engineered cells typically include modified genomic or plasmid DNA with genes for sensing proteins that regulate the production of a reporter protein in response to a target analyte.

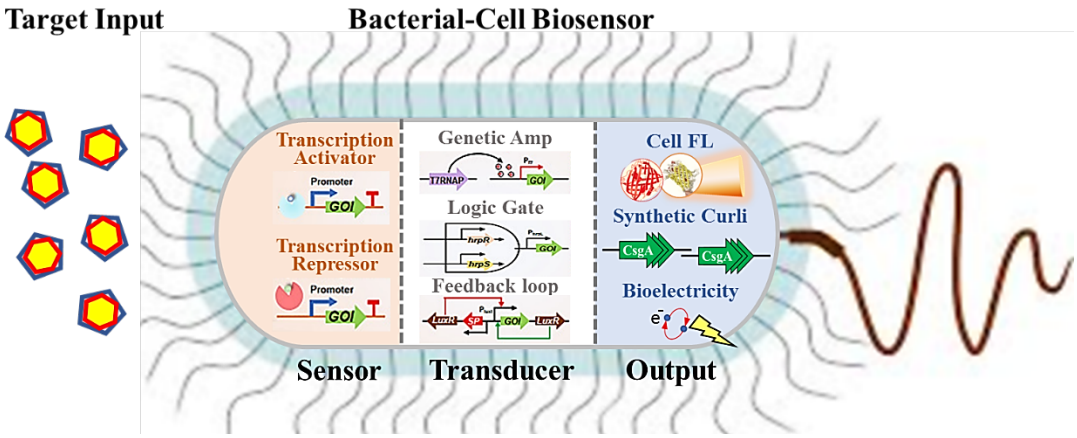

Figure 2.8: Concept of using bacterial cells as natural biosensors since they can integrate a sensing element with a transducer to directly convert the recognition event into a measurable output for detecting a target molecule(s).

Unlike other protein-based sensors, bacterial biosensors are typically inexpensive to prepare and store and can be conveniently engineered for miniaturized, high-throughput analysis and multiplexing purposes [40]. Synthetic biology has been repurposing these cellular components by genetically engineering the bacteria to detect a wide range of analytes. For instance, using reporter genes, the cells can produce a measurable signal in response to the presence of the target molecule, such as heavy metals [41], biotoxins [42], and inflammations. The most common choices for the reporter proteins used in synthetic biology are fluorescent and luminescent proteins that generate a measurable signal in the optical domain. In the next section, we will briefly introduce the principle of working for these two protein types.

2.5.1 Fluorescent Proteins

Fluorescent proteins are versatile and well-adopted signal reporters in synthetic biology with diverse optical profiles, allowing the detection of multiple signal outputs [43]. The read-out

mechanism for these proteins is called fluorescence, a category of luminescence processes in which specific molecules respond to an external excitation by emitting light after a brief interval [44]. Exciting a material with light (λ_1) causes electrons in the stable states to acquire energy and transition to the higher energy bands. Due to heat and collisions with other electrons, the unstable electrons lose energy and return to their stable states. In this process, a weak light at slightly higher wavelength ($\lambda_2 > \lambda_1$) is released, indicating the presence of the desired molecules (Figure 2.9).

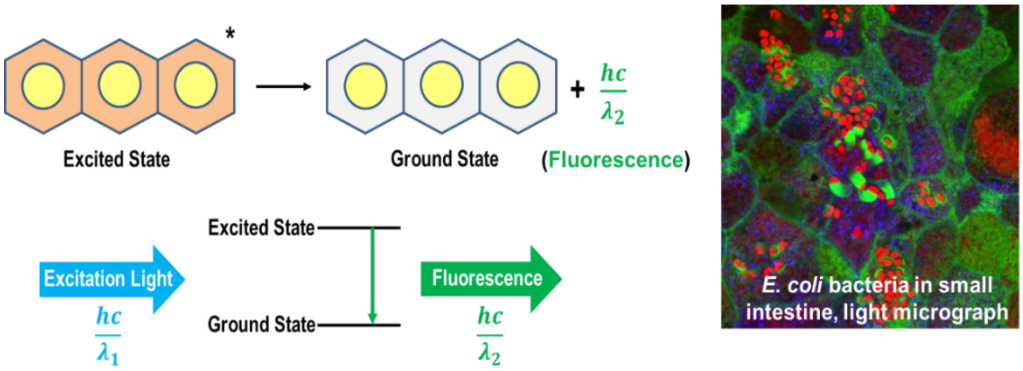

Figure 2.9: Principle of fluorescence detection.

The emitted light intensity, I_f is proportional to the excitation light intensity I_0 as:

$$I_f = kI_0\Phi[1 - 10^{-\varepsilon bc}] \tag{2.1}$$

in which, Φ is the fluorescence quantum yield, ε is the molar absorptivity, b is the path length, and c is the culture concentration [44].

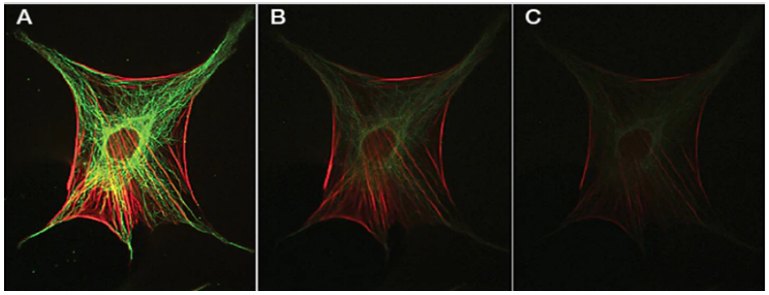

Figure 2.10: Photobleaching of fluorescein in cells after A) 0 sec. B) 5 sec. C) 15 sec. The fluorescein is almost destroyed after 15 sec.

Even though (2.1) suggests a stronger excitation light results in a higher emission signal, high-intensity illumination may cause photobleaching. The fluorophore's structural instability during the excited lifetime makes it susceptible to degradation. Therefore, high-intensity and/or long-time illumination can cause the fluorophore to change its structure so that it can no longer fluoresce; this degradation of fluorophores is called photobleaching [45].

Most common fluorescent proteins extensively used with live bacterial cells (GFP, YFP, RFP) lie in the lower range of the visible wavelength spectrum with a slight Stokes shift. Hence, to differentiate between strong excitation light and weak emission signal, conventional fluorescence sensors require an elaborate and bulky setup with several optical components such as lenses, objectives, thin film or dichroic filters, precision mechanical scanners and high-performance photon detection units, including CCDs, photo-multiplier tubes (PMT) or avalanche photodiodes (Figure 2.11). Although highly precise, these systems are used in lab settings and are not practical for *in vivo* and portable applications [46].

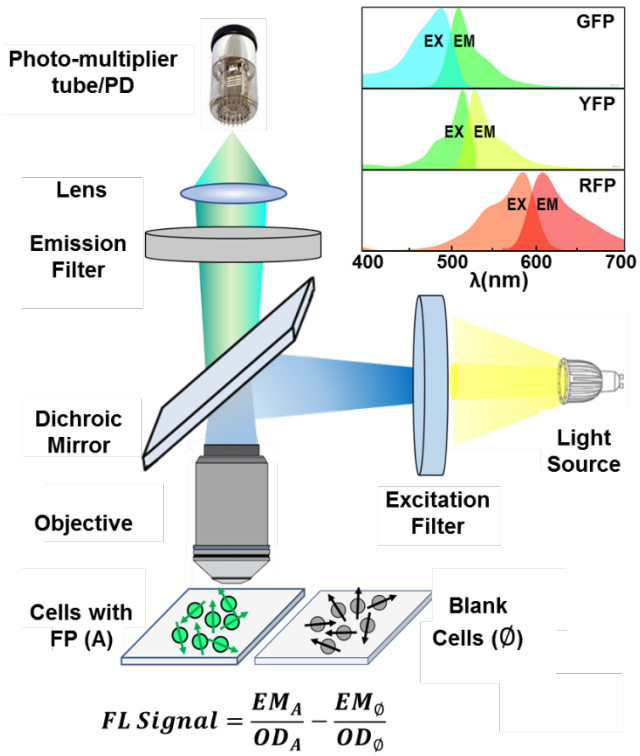

Figure 2.11: Conventional fluorescence sensor and spectrum of common fluorescent proteins.

Measuring the fluorescence signal of a protein involves using two cultures, the control culture (ϕ), containing blank bacterial cells to account for their auto- fluorescence response, and the primary culture (A), which includes bacterial cells engineered with the desired fluorescent protein. The fluorescence signal is calculated by subtracting the auto-fluorescence signal from the emission of culture A after being normalized to their respective optical density (OD).

OD is a measure of the cell population that can be measured optically. In OD measurement, light at a specific wavelength (usually 600nm) is transmitted through a sample of cells and subsequently collected by a photodetector. Based on Beer-Lambert law, more light is absorbed and scattered as bacterial cells grow, resulting in less light reaching the detector [47]. By recording OD over time, the growth curve of the bacteria is achieved, showing the status of cells during their life cycle, starting from the lag phase to death in the decline phase. The most important part of the curve that shows the healthy growth of cells is the exponential phase (Figure 2.12).

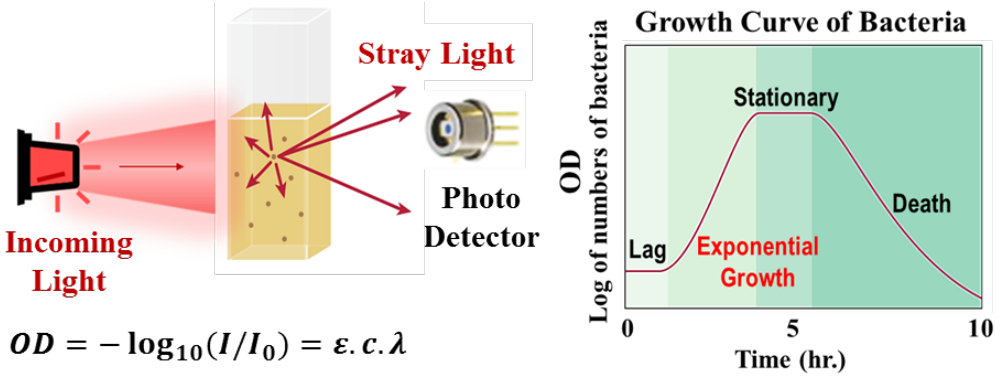

$$OD = -\log_{10}(I/I_0) = \varepsilon.c.\lambda$$

I : Intensity of light passed through cell sample
I_0 : Reference value for the medium without cells
ε : Molar absorption coefficient

Figure 2.12: OD definition and measurement principle.

2.5.2 Luminescence Proteins

Another class of signal reporter used for bacterial cells are luminescent proteins that emit light without a light source (excitation). This feature can be beneficial in bioimaging

applications where high sensitivity is required while being as invasive as possible. Furthermore, using these proteins eliminates the problems associated with the fluorescence process, such as auto-fluorescence, photo-induced damage, or an undesirable physical reaction to the sample caused by an excitation source [48]. The main protein of this family is luciferase which generates light by catalyzing the oxidation of luminescent chemicals such as luciferin (Figure 2.13).

However, while luminescent proteins are suitable outputs for genetically modified biosensors, they are energy-consuming for the host cells and would become dimmer over time. Additionally, since a light source is not required to activate their light emission, the luminescence signal would interfere with the optical density detection, which is needed to monitor cell growth in real-time applications. One recent biosensor implementation using these proteins is reported in [49], where a single-chip sensor assays the biological output signals while avoiding the challenge of integrating optical filters on-chip.

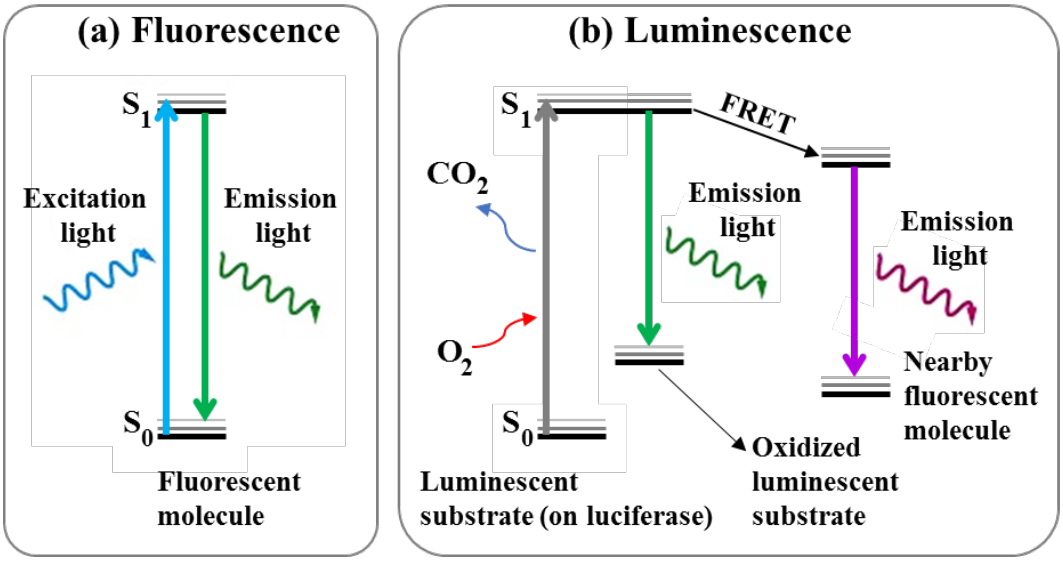

Figure 2.13: The difference between fluorescent and luminescent process, (a) A fluorescent dye excited by external light source. (b) S_0–S_1 transition of luminescent substrate by oxidation reaction.

2.6 Miniaturized Bacterial-Based Sensor

The motivations to develop a miniaturized system that can integrate versatile sensing capabilities of live bacterial cells with the processing circuitry of a CMOS chip are twofold. First, real-time and reliable signal measurement and reporting in medical diagnosis and environmental sensing can be achieved. Second, gene expression control via CMOS chips can be enabled, creating a promising platform for developing future closed-loop therapeutics and environmental remediation applications.

Encoding the genetically engineered bacterial cells with designed DNA sequences can enable the production of desired enzymes, nucleic acids, and small molecules in these cells in response to stimuli (optical). However, optimizing gene expression dynamics through feedback control has been a significant challenge in synthetic biology due to the difficulty in real-time monitoring of cell dynamics [50]. Therefore, a Silicon-Cell system has considerable potential for enabling feedback control of living cell dynamics. This feedback control function could have applications in medicine where bacteria may be employed for delivering anti-cancer [51] or anti-inflammatory [52]-[53] compounds to treat diseases, or in environmental remediation, where bacterial cells can produce enzymes to degrade contaminants such as plastic [54] and oil spills [55]. In the next chapter, we introduce the concept of the Silicon-Cell device in more detail.

Chapter 3

INTEGRATED SILICON-CELL DEVICE TO USE LIVING BACTERIAL CELLS AS BIOSENSORS

Chapter 3 introduces the Silicon-Cell as a miniaturized biosensing device that, beyond fluorescence detection, facilitates bidirectional communication between the CMOS chip and living bacterial cells. The theoretical analysis of the system and its components is discussed, including the fundamentals of optical resonances used to realize integrated optical filters insensitive to the incoming light's polarization and angle of arrival.

3.1 Silicon-Cell for Bidirectional Communication

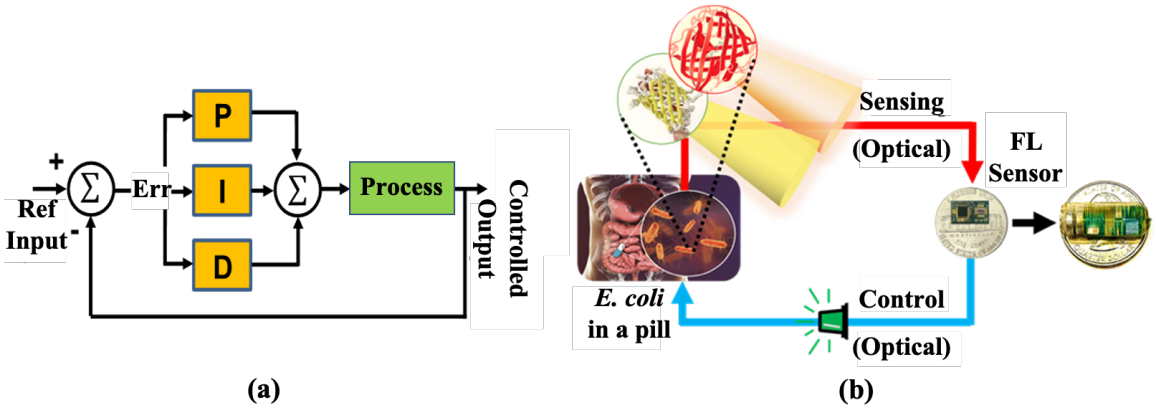

Figure 3.1: (a) Block diagram of PID loop. (b) Bidirectional communication between the CMOS fluorescence chip and living cells packaged inside a pill for detecting gut inflammatory disease.

The idea of communicating with living cells and controlling their dynamic behavior was a huge motivation for this work. A closed-loop system can be implemented by real-time monitoring the cell's growth and fluorescence expression and applying a promoter in response to the detected changes. For example, the promoter can make the cells start/stop producing desired enzymes, nucleic acids, and small molecules for various applications. This bidirectional communication with cells provides the opportunity to implement control

mechanisms, such as the proportional (P), integrating (I), or derivative (D) type (Figure 3.1(a)). In a conceptual diagram shown in Figure 3.1(b), a two-way communication link between engineered cells and a CMOS fluorescence sensor can be established to sense and treat a patient's gut swelling, where both sensing and control functions are done via optical signaling.

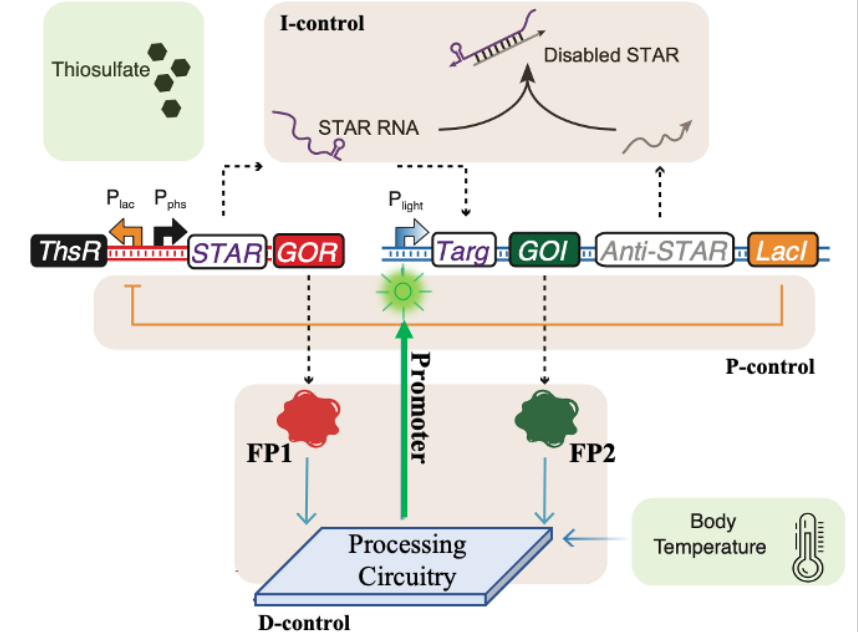

Figure 3.2: Concept of complete PID loop implemented by P and I control in biology and D control in electronics.

The detailed biology process for this application is shown in Figure 3.2. Thiosulfate (ThS) is a chemical that shows signs of swelling in the patient's gut. A process in synthetic biology is designed that uses two fluorescent proteins to report the presence of the gene of reference (GOR) and gene of interest (GOI), respectively, by FP1 and FP2. In this terminology, GOR is the gene we want to detect and control (associated with ThS), and GOI is the gene we instruct the cells to produce (by applying a promoter) to reduce swelling. The amount of provided GOI needs to be regulated via a control loop, for instance, in the most complete form using a PID loop. As shown, some part of the control loop is implemented in the biology domain (P and I), and the D control, which can't be done in the biology domain, is easily

implemented in electronics. Hence, to implement a closed-loop system, the CMOS fluorescence sensor must measure two fluorescent proteins and the cell's growth dynamics while small enough to fit inside a pill.

3.2 Proof-of-Concept System

Before proceeding to the design of the fully integrated Silicon-Cell device in the CMOS process, using off-the-shelf components, a prototype was built to prove the concept. Several static/dynamic fluorescence measurements were performed to gain practical knowledge of cell measurements and get insights into designing a more efficient integrated sensor. The prototype is shown in Figure 3.3, and it includes exciting LEDs on top, a 4-reservoir sample chamber (3D printed), an emission filter, and a 4-channel photodiode and processing circuitry. We started with the static fluorescence measurements for two selected fluorescent proteins, namely LSSmOrange [56] and miRFP [57], with their respective spectrum shown in Figure 3.4. The measured responses of the cultures to the blue excitation (450nm) and UV excitation (380nm) are presented in Figure 3.5.

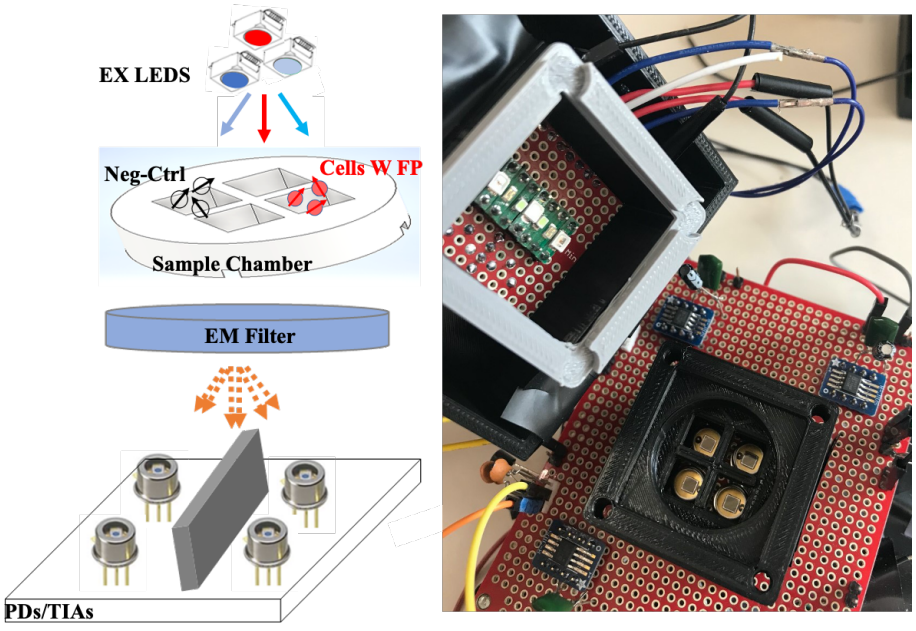

Figure 3.3: A 4-channel prototype for static fluorescence measurements.

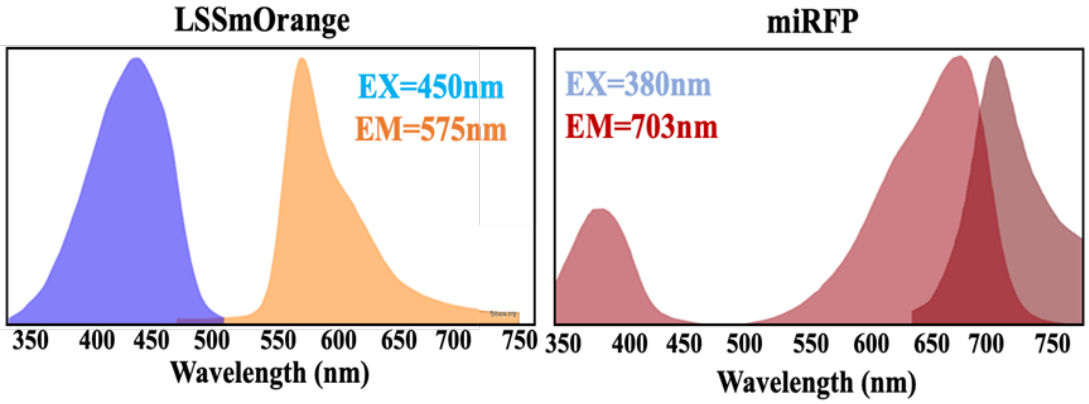

Figure 3.4: Spectrum of miRFP and LSSmOrange proteins.

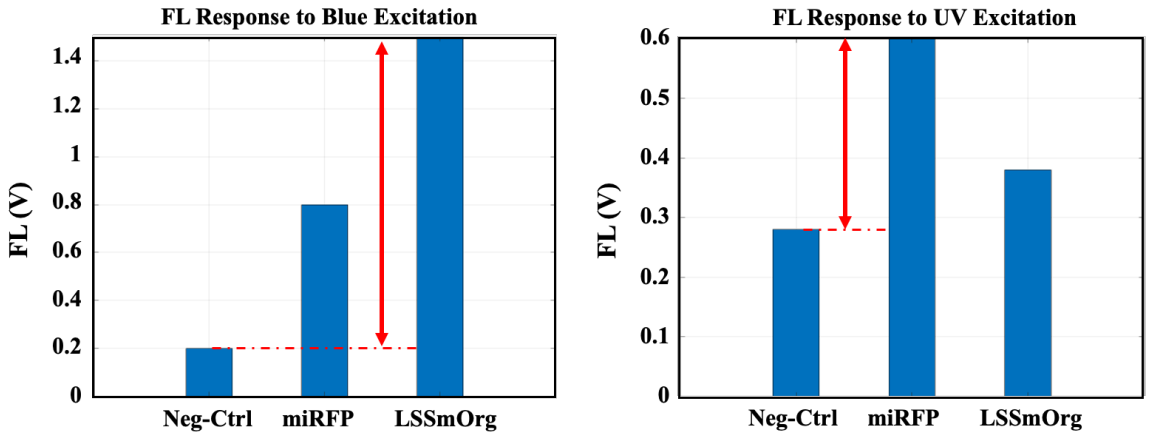

Figure 3.5: Measured fluorescence responses of selected fluorescent proteins to Blue/UV excitations.

Since LSSmOrange mainly responds to blue light and miRFP to UV light, the red arrow in each plot shows the fluorescence signal strength for the responding protein. The plots also show the crosstalk response of the two proteins, which is essential information for performing the mixture experiments.

The second set of experiments was designed to show that even with the crosstalk between two proteins, we could detect the presence of one fluorescent protein in a mixture. As shown in Figure 3.6, we have a main culture containing an equal mix of two selected fluorescent proteins and two subsequent cultures; in each, one of the proteins is replaced

with the Neg-Ctrl sample. The plots in Figure 3.7 show the measured responses of each culture to two excitations. We see that the main culture and the culture containing LSSmOrange have around the same signal level response to the blue excitation, while the culture missing LSSmOrange, is weaker. This result confirms that the main protein responding to the blue excitation is the LSSmOrange, and its presence decides the signal level. Figure. 3.7 also shows the same behavior for the miRFP protein and the UV excitation.

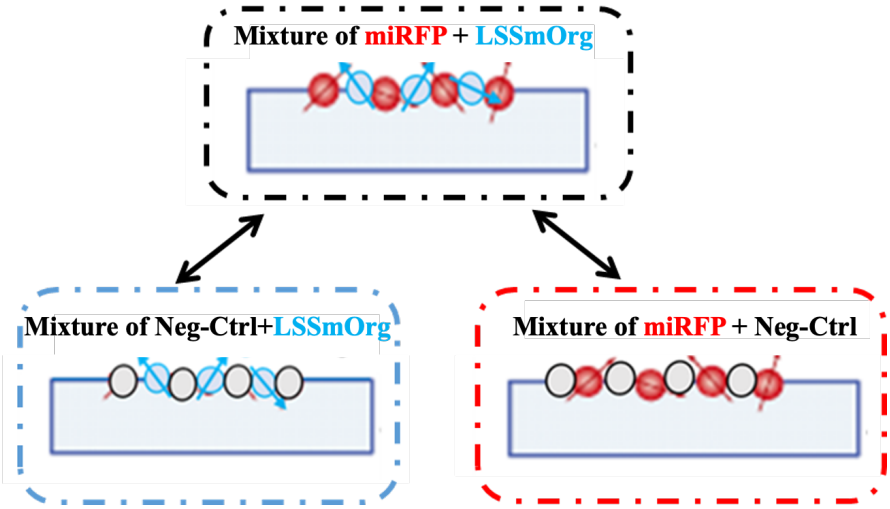

Figure 3.6: Cultures used for mixture fluorescence measurements.

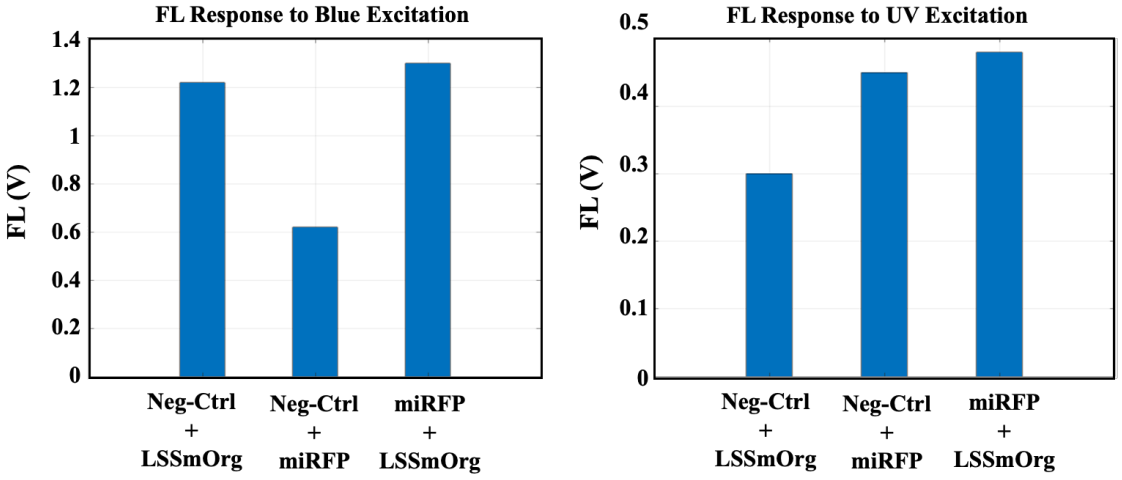

Figure 3.7: Measured fluorescence responses of fluorescent protein mixtures.

The last experiment with the prototype device is designed to study the feasibility of two-way communication between living cells and the processing circuitry. The GFP [58] protein was selected for this step due to its fast folding response and compatibility with the green promoter. To accommodate this fluorescent protein, the setup needed some modifications, including adding an excitation filter to reduce the leakage of the excitation light, which otherwise could quickly saturate the single-ended receiver, and moving the green promoter and the red LED for the OD measurement to the PCB surface. Even though this is not an optimum placement for the OD LED, as shown, the device still worked, though with lower sensitivity for OD measurement. To start these dynamic experiments, we first grew bacterial cells engineered with GFP in a rich media overnight to their stationary phase. Then the following day, we diluted them with a 1:50 ratio using a clear media solution and grew them for another 4 hours to have the cells in the middle of their growth phase. Next, we dilute the cells to a very low OD value and start the dynamic experiment in an incubator overnight while measuring their OD and fluorescence every 20 minutes.

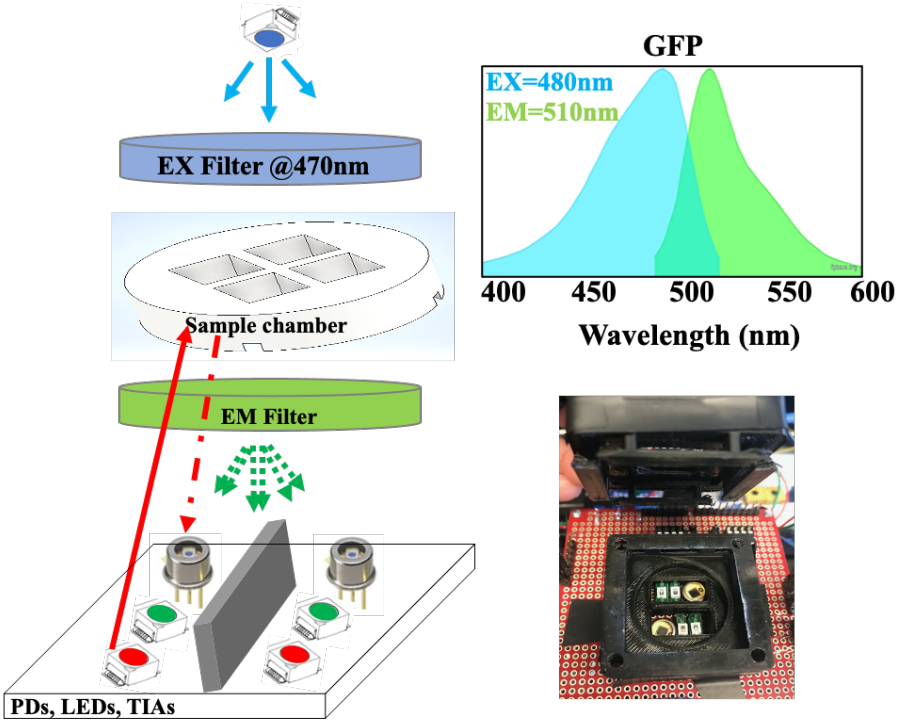

Figure 3.8: Modified prototype setup for dynamic fluorescence/OD measurement of GFP.

As shown in Figure 3.9, two sets of experiments were performed. Figure 3.9 (a) shows the cell's OD and normalized fluorescence /OD results for GFP and Neg-Ctrl cultures while the green light promoter is present, resulting in strong protein production. On the other hand, when there is no promoter, the fluorescence expression of the cells is minimized. By subtracting the fluorescence/OD of the Neg-Ctrl from the GFP culture, the difference in the protein expression level in the two cases is more evident, as shown in Figure. 3.10. These results confirm the feasibility of protein expression control via applying an appropriate promoter signal, enabling a closed feedback loop realization.

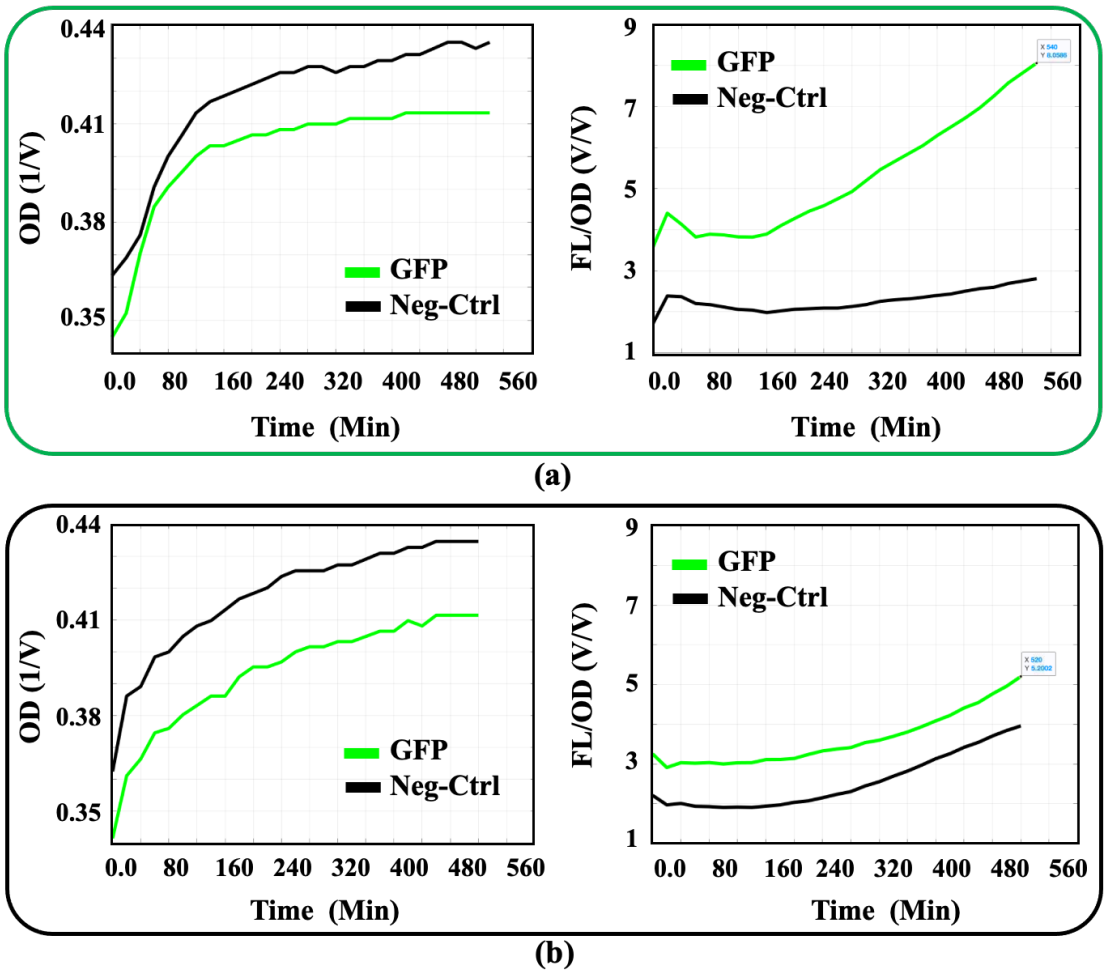

Figure 3.9: Measured OD and fluorescence/OD response of GFP when (a) green promoter is present and (b) in the dark (w/o green promoter).

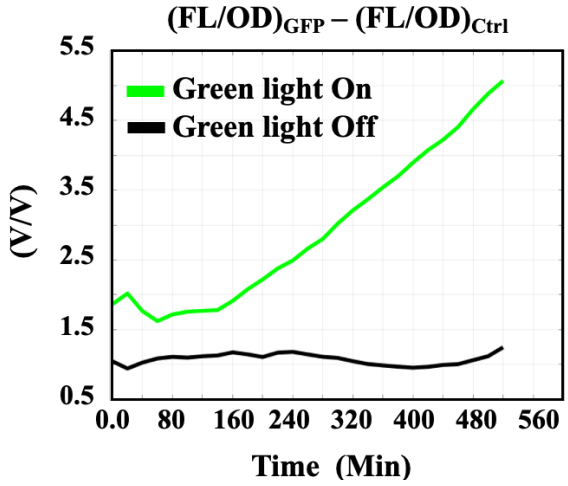

Figure 3.10: Modulation of fluorescence production using optical signaling.

3.3 CMOS Fluorescence Sensor

After confirming the possibility of bidirectional communication with the cells, we proceed to implement a fully integrated fluorescence sensor required for a portable Silicon-Cell device. The CMOS process offers an exciting and efficient platform for implementing all the components of fluorescence detection in a single chip. Using a standard CMOS process without additional fabrication steps, the sensor can be low-cost and miniaturized enough to be suitable for *in vivo* applications. As shown in the conceptual Figure 3.11, the idea is to implement optical filters using available CMOS metal/dielectric layers, photodiodes using various P and N doping layers, and sensitive circuitry to process the signals, all in the same chip.

The most critical task in realizing a fully integrated fluorescence sensor in the CMOS process is implementing narrowband optical filters to reject the strong excitation light close (in wavelength) to the weak emission signal. Conventionally, high-quality optical filters are made by custom nano fabrication tools and using arbitrary geometries in low-loss metal or all-dielectric layers [59,60,61,62]. In one such implementation, using subwavelength metal/dielectric gratings with different periods, a multiband filter is achieved in a single layer [60]. The structure includes a silica substrate and ultra-thin metal (silver) patches where for each filter the structure needs to be multiple wavelengths in size laterally (Figure 3.12).

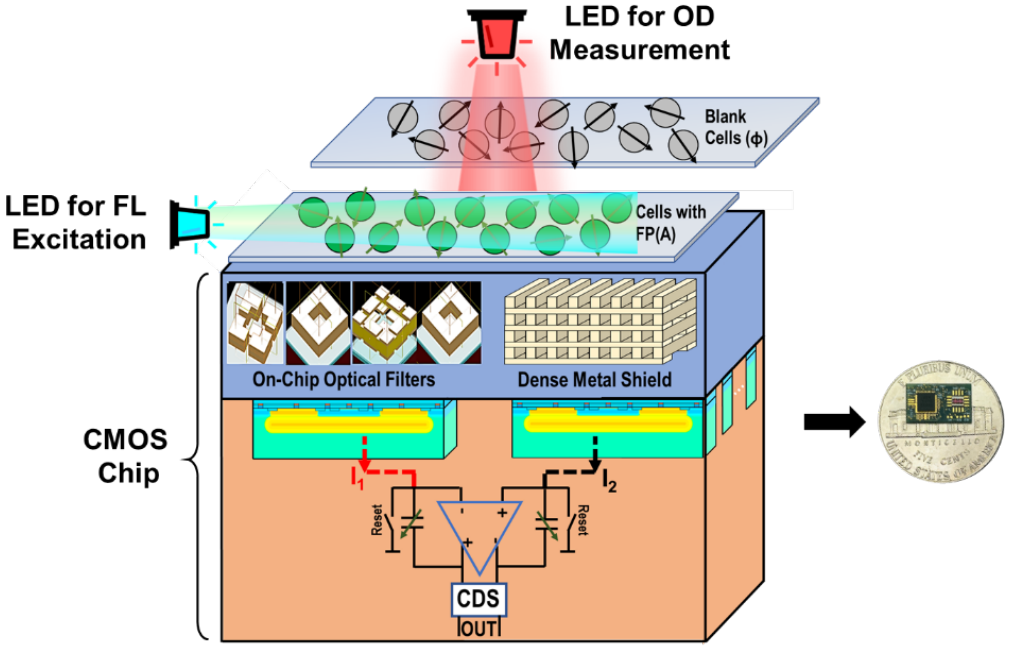

Figure 3.11: Conceptual overview of the integrated fluorescence sensor implemented in the standard CMOS process and the optimal placement of LEDs for fluorescence and OD measurements.

Another work [63] shows that to increase the efficiency of the filters and reduce metallic loss, filters can be implemented using subwavelength dielectric gratings in an all-dielectric design. In this work, the poly-silicon film is patterned on a SiO_2 spacer layer in subwavelength size to achieve a multicolor filter in one structure (Figure 3.13).

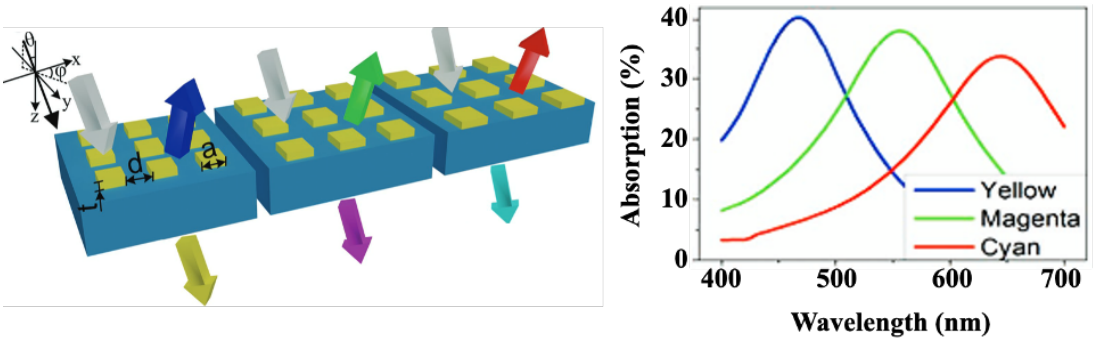

Figure 3.12: Prior art on implementing multi-color optical filtering using gratings with different periods in a single layer [60].

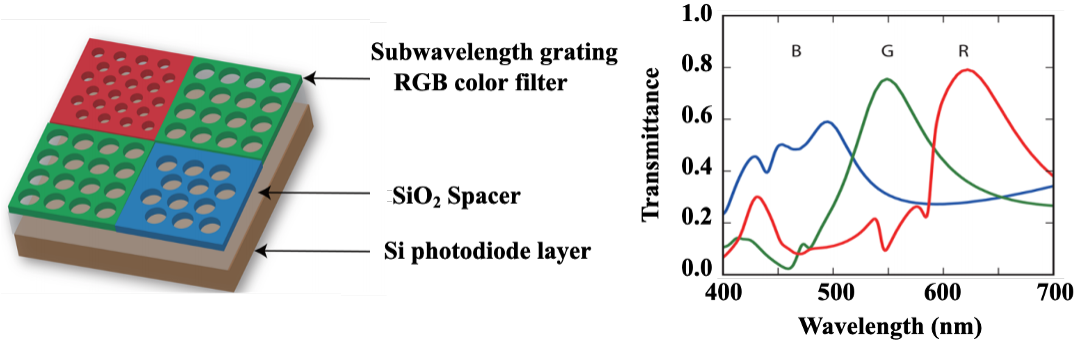

Figure 3.13: Prior art on high-efficiency optical filters using all-dielectric materials [63].

The high transmission of these filters in the desired wavelength is ensured by using low-loss material and arbitrary geometries, none of which are available in a standard CMOS process with a fixed stack-up and rules (Figure 3.14).

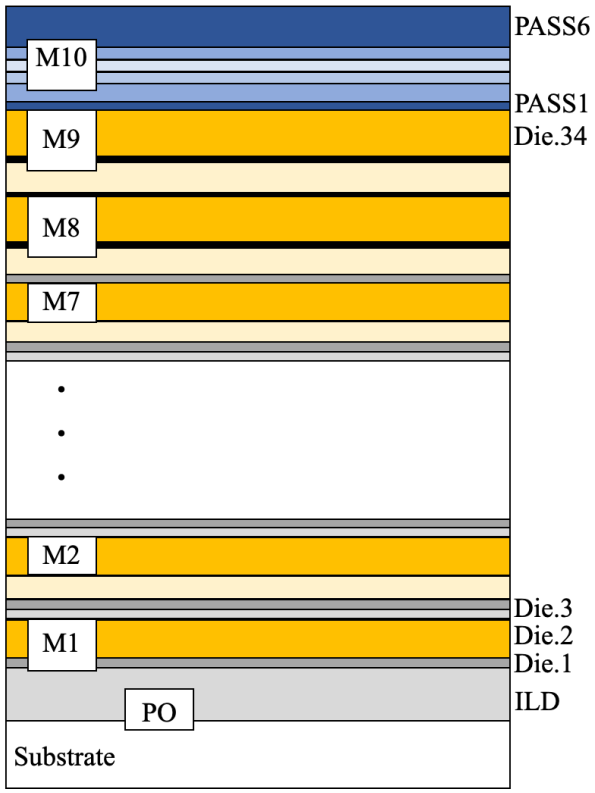

Figure 3.14: Sample stack up of 65nm CMOS process, showing several metal/dielectric and passivation layers.

3.3.1 Optical Filter Realization in CMOS

Advanced CMOS technologies have multiple routing metal (Cu) and dielectric (variations of Sio2) layers and allow sub-wavelength feature sizes with high precision. Hence, fundamentally we have the required materials and tools to implement optical filters. However, CMOS poses several challenges in implementing efficient filters in the wavelength of interest, including fixed material of the stack-up, lack of information about all the used layers in the stack-up, and strict design rules check (DRC) of CMOS that avoids designing arbitrary geometries in shapes and dimensions. Since DRC enforces using metal layers in the filter geometry by applying the minimum metal area rule, studying the behavior of metals at optical frequencies is imperative [64].

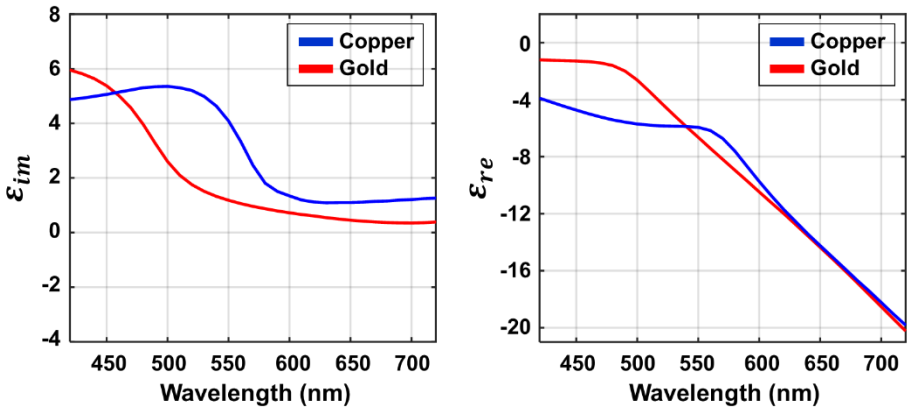

Figure 3.15: Comparison of optical properties of copper vs. gold.

Optical properties of metals vary significantly over a wide frequency range, from being highly reflective in the microwave and far-infrared range up to a near-dielectric behavior in the UV range [65]. At higher frequencies, field penetration into metal increases resulting in more dissipation and attenuation. The metal's complex dielectric function $\epsilon(\omega)$ can completely describe these various dispersive properties. The real and imaginary components of the dielectric function can be derived as:

$$\epsilon_{re}(\omega) = n^2(\omega) - \kappa^2(\omega) \tag{3.1}$$

$$\epsilon_{im}(\omega) = 2n(\omega)\,\kappa(\omega) \tag{3.2}$$

in which $n(\omega)$ is the real part of the complex refractive index and κ is the extinction coefficient determining the optical absorption of electromagnetic waves propagating in a medium. Hence, $\epsilon_{im}(\omega)$ can be used as an indicator of the metal absorption level of the optical wave. Figure 3.15 compares the real and imaginary parts of $\epsilon(\omega)$ for copper as the available metal in CMOS, and gold as the standard and low-loss metal, showing a much higher loss of copper than gold for wavelength range lower than 600nm. This observation helps decide the best type of dominant resonance mechanism for the bandpass optical filter in terms of metallic loss. Additionally, the selected resonance type should have low sensitivity to the incoming light's angle of arrival (AOA) and polarization since cells in a biological culture are considered unpolarized light dipoles emitting in random directions and polarizations. Next, we will review the main optical resonance types that can be used to implement optical filters in the CMOS platform.

3.4 Review of Optical Filter Design

Three main categories of optical resonances that can be used in implementing the filters are plasmonic resonance, guided-mode resonance, and cavity-mode resonance.

3.4.1 Plasmonic Resonance

The history of creating light effects using nanostructures dates back to the Roman Empire when artists incorporated gold particles in glass artwork to create numerous colors in different light settings. One famous example is the Lycurgus cup, which is green when observed in the reflecting light and red when placed in the transmitting light. (Figure 3.16).

Figure 3.16: Lycurgus cup as seen in different colors based on the light conditions.

The scientific investigation of the electromagnetic properties of metals goes back to the works of Gustav Mie (1908) and Rufus Ritchie (1957). Since then, the studies of the interaction of electromagnetic waves with metal/dielectric interfaces, called Plasmonics, have steadily gained considerable interest [66,67,68]. Developing nanofabrication and characterization techniques, such as electron beam lithography and near-field microscopy, further motivated Plasmonics. Various optical functions can be implemented by manipulating the electric field through metallic nanostructures. A wide range of applications includes the development of nano-antennas/arrays for biological and chemical sensors [69,70], sub-wavelength waveguides [71], efficient solar cells [72], and narrowband optical filters [73, 74, 75].

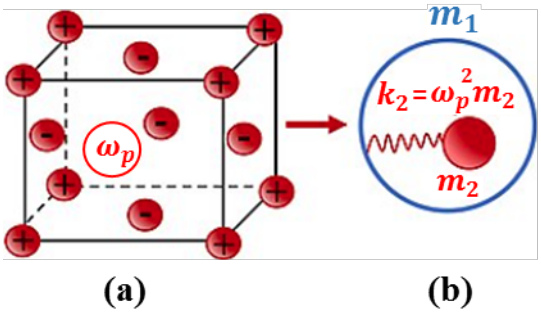

Figure 3.17: (a) Free e^- gas m_2 embedded into an ionic lattice m_1. (b) The equivalent mechanical scheme of the plasma model.

The optical properties of metals and their interaction with electromagnetic fields can be described using classical Maxwell equations and considering the plasma model for metals. In this model, it is assumed that an electron gas (effective electron mass M), with density N, freely propagates behind a background of positively charged atom cores. Then, in the presence of an electromagnetic field, the electrons start to oscillate, and their movement is damped with the characteristic time τ. The electron motion in the plasma model can be achieved using the below equation:

$$m\ddot{x} + \frac{m\dot{x}}{\tau} = -eE(t), \qquad E(t) = E_0 e^{-i\omega t} \tag{3.3}$$

which is solved to give the following solution for the electron's motion:

$$x(t) = \frac{e}{m(\omega^2 + i\omega/\tau)}\, E(t) \tag{3.4}$$

The displaced electrons (relative to the atom core) then generate a polarization vector $P = -Nex(t)$, which results in the dielectric displacement D in a linear, isotropic, and non-magnetic media as:

$$D = \epsilon_0 E + P = \epsilon_0 E + \left(-Nex(t)\right) \tag{3.5}$$

Replacing the electron motion x(t) from (3.4) and nothing that $D = \epsilon_0 \epsilon E$, we achieve the frequency-dependent dielectric constant of metals that can describe their behavior in a wide frequency range.

$$D = \epsilon_0 (1 - \frac{\omega_p^2}{\omega^2 + i\omega/\tau}) E \tag{3.6}$$

$$\epsilon(\omega) = 1 - \frac{\omega_p^2}{\omega^2 + i\omega/\tau} = 1 - \frac{(\omega_p \tau)^2}{(\omega\tau)^2 + i\omega\tau} \tag{3.7}$$

in which $\omega_p = \sqrt{Ne^2/(\epsilon_0 m)}$ is called the plasmon frequency. Considering (3.7) at large frequencies, $\omega \gg 1/\tau$, the damping term in the denominator can be neglected, resulting in the approximately real $\epsilon(\omega)$ as:

$$\epsilon(\omega) \approx 1 - \frac{{\omega_p}^2}{\omega^2} \tag{3.8}$$

Next, using the wave vector equation, $k^2 = \epsilon(\omega).\frac{\omega^2}{c^2}$, and substituting $\epsilon(\omega)$, the dispersion relation of the electromagnetic field can be achieved as below:

$$\omega^2 = {\omega_p}^2 + k^2/c^2 \tag{3.9}$$

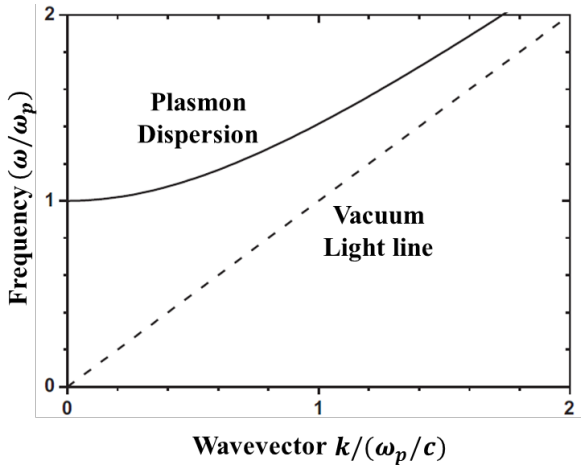

Figure 3.18: Dispersion relation of the free electron gas.

As shown in Figure 3.18, there is no electromagnetic wave propagation for the frequencies lower than the plasmon frequency ($\omega/\omega_p < 1$). However, when the damping is low (i.e., $\epsilon(\omega_p) \approx 0$), a collective longitudinal oscillation of the conduction electron gas with respect to the fixed background of positive atom cores is formed at the plasmon frequency. This charge oscillation is called bulk plasmons which cannot couple to transversal EM fields and hence cannot be excited from direct irradiation. In contrast to bulk plasmons, surface plasmons polaritons (SPP) are electromagnetic excitations that propagate along the interface between a metal and a dielectric medium [65]. The starting point to derive these excitations is again Maxwell's equations which must be solved separately at the metal and dielectric parts of the interface.

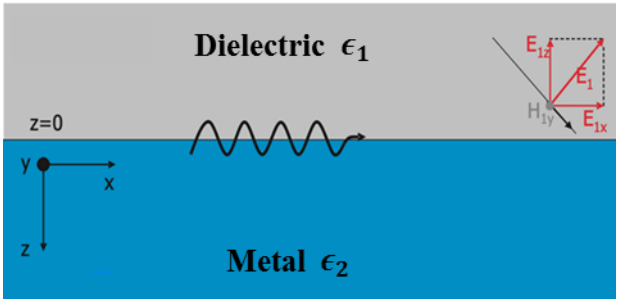

Figure 3.19: Interface along the x-y plane between a dielectric and a metal.

Referring to the geometry of Figure 3.19, the following boundary conditions for the normal and transversal field components at the interface need to be satisfied:

$$D_{1,z} = D_{2,z} \quad , B_{1,z} = B_{2,z} \tag{3.10}$$

$$E_{1,x/y} = E_{2,x/y} \, , H_{1,x/y} = H_{2,x/y} \tag{3.11}$$

where indices (1) and (2) indicate the components of the fields at the dielectric and metal mediums. It is shown that these conditions are only met for a field with transverse-magnetic (TM) mode propagating along the x direction with the following field descriptions [66]:

$$E_i = (E_{ix}, 0, E_{iz}) e^{i(k_i r - i\omega t)}, i = 1,2. \tag{3.12}$$

$$H_i = \big(0, H_{iy}, 0\big) e^{i(k_i r - i\omega t)}, i = 1,2. \tag{3.13}$$

in which $k_i = (\beta, 0, k_{i,z})$ is the wavevector with the x component named β, the wave propagation constant along the x direction. Next, in the absence of free charges and currents at the interface ($\rho = J = 0$) and using Maxwell's equations (3.14 and 3.15), a relationship between z components of the wavevector and the medium's dielectric constants is achieved.

$$\nabla . D = \rho \tag{3.14}$$

$$\nabla \times H = J + \partial D / \partial t \tag{3.15}$$

$$\frac{k_{1,z}}{k_{2,z}} = \frac{\epsilon_1}{\epsilon_2} \tag{3.16}$$

Since we are interested in the solutions that result in the modes bound to the interface, the components of $k_{i,z}$ must be imaginary and of opposite sign. The achieved fields then have exponentially decaying characteristics in each half-space, with the field's penetration depth of δ_1 and δ_2. Therefore, considering equation 3.17, it is evident that the dielectric constants of two half-spaces should also be of opposite signs (i.e., $\epsilon_1 = -\epsilon_2$), meaning that surface plasmons can only exist at the interface of a metal ($\epsilon < 0$) and a dielectric ($\epsilon > 0$).

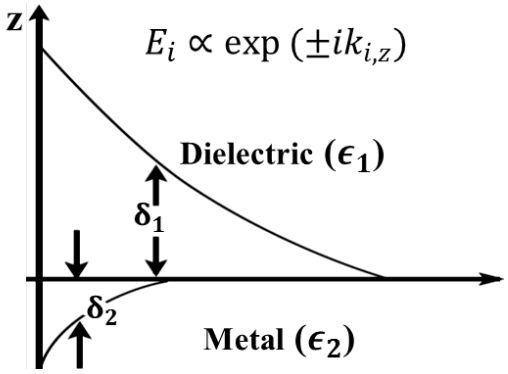

Figure 3.20: The decaying evanescent characteristics of fields at the interface.

As shown in Figure 3.21, SPP comprises an electromagnetic wave in the dielectric medium and an oscillating electron plasma in the metal, where both modes have exponentially decaying evanescent characteristics. Substitution of equation (3.16) in the wave vector gives the propagation constant of the surface wave in terms of the two medium's dielectric constants.

$$\beta = k_0 \sqrt{\frac{\epsilon_1 \epsilon_2}{\epsilon_1 + \epsilon_2}} \tag{3.17}$$

Using the frequency-dependent $\epsilon_2(\omega)$ for the metal above the plasmon frequency and noting that the $\epsilon_1(\omega)$ for dielectric is approximately constant, the SPP dispersion relation of Figure 3.22 is obtained, which is seen to be below the light cones at all nonzero frequencies. Therefore, SPP cannot be excited by direct light illumination as energy and momentum conservation cannot be satisfied simultaneously, and a momentum transfer is needed [76].

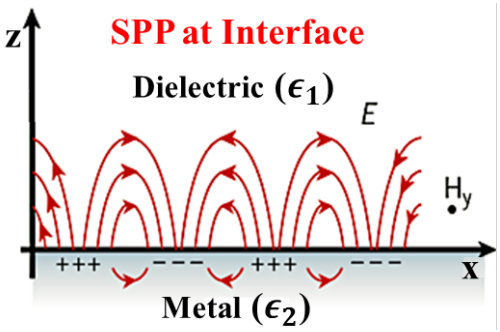

Figure 3.21: Composed character of SPPs at the interface between dielectric and metal.

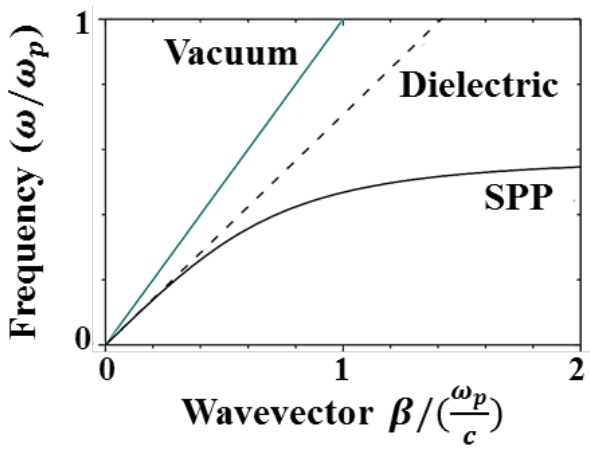

Figure 3.22: Dispersion relation of SPP vs. to light in vacuum and in the dielectric medium.

Metallic features such as periodic gratings are the most common ways of meeting the momentum mismatch [77]. The grating equation in (3.18) shows the relationship between β, the structure period (a), and the electromagnetic wave incident angle (θ):

$$\beta = k_0.\sin\theta \pm 2\pi n/a, \quad n = 1,2,\ldots \tag{3.18}$$

Even though the SPP resonance can be very sharp, the strong dependency between its resonance wavelength and θ makes it unsuitable for the fluorescence sensor with the random incident angle. Additionally, the metallic loss is a significant concern for SPP since part of this wave needs to propagate inside the metal, making it less attractive in CMOS with copper as the available metal and due to strict DRC enforcing minimum metal area usage.

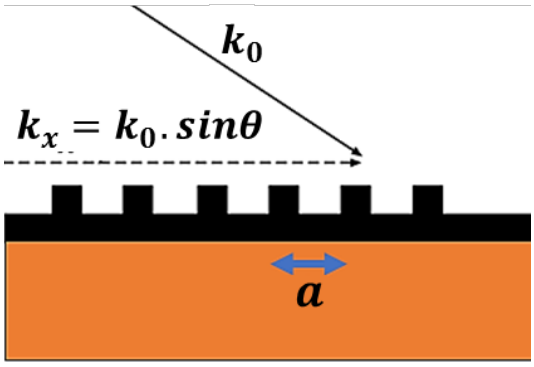

Figure 3.23: 1D periodic grating as a popular way of satisfying momentum mismatch for SPP excitation.

3.4.2 Guided Mode Resonance

It is instructive to consider the single grating structure in TE polarization, where SPP cannot exist. As shown in Figure 3.24, while the TM transmission of this structure is relatively high (due to SPP), the TE wave is mainly reflected. Adding the second row of the identical grating on top introduces constructive interferences of transmitted and reflected light by two consecutive structures. As a result, at some opto-geometrical parameters, the double grating structure can achieve high transmission and support guided mode in TE polarization [78]. For the double grating design (Figure 3.24 (b)), surrounded by medium n_2 and infinite in the y direction, the following holds [79]:

$$n_2^2 k_0^2 = k_x^2 + k_y^2 + k_z^2, \quad k_y = 0 \tag{3.19}$$

The grating structure shifts k_x to $k_0 \sin\theta + \frac{2\pi n}{d}$, and at the same time, the transverse resonance condition to support the guided mode in medium n_2 roughly requires $k_z = \frac{\pi m}{t}$ [80].

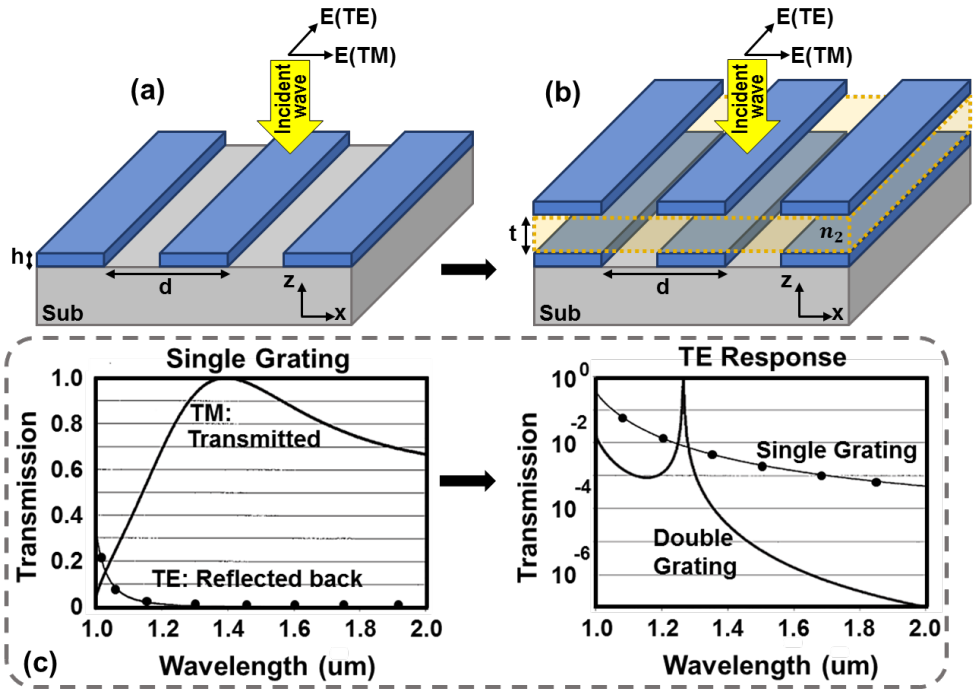

Figure 3.24: (a) The single grating structure supporting SPP. (b) The double grating structure supporting guided mode. (c) TM and TE responses of two structures.

For the normal incident ($\theta = 0$), by replacing these components of the wave vector with their equivalent values, we get the following:

$$\left(\frac{2\pi n_2}{\lambda}\right)^2 = \left(\frac{2\pi n}{d}\right)^2 + \left(\frac{\pi m}{t}\right)^2 , n, m = \text{integer} \tag{3.20}$$

which shows that the m^{th} mode of the slab can be excited through the n^{th} order of grating. Solving (3.20) using n=m=1 gives the thickness (t) for the presence of the guided mode through 1^{st} order of gratings [78]. Since the wave propagates in the dielectric area surrounded by the metal and is not coupled to the interface, this resonance is less lossy than the SPP. In this structure, a narrow spectral response can be achieved by closing the resonator (i.e., decreasing the aperture) as it reduces the coupling with the incident light [81]. While this is desired for implementing sharp bandpass filters, exciting the waveguide mode through the 1^{st} diffraction order of gratings links the incident angle θ to the wave propagation constant and hence λ. Therefore, the narrow spectrum in the wavelength results in a narrow response to the θ, which is undesirable due to the lack of collimated incident light in fluorescence sensing.

3.4.3 Cavity Mode Resonance

The mentioned challenge in the linked $\lambda - \theta$ responses of the previous two resonances can be suppressed using cavity resonances [78]. Figure 3.25 shows the double grating structure with added vertical metallic walls between adjacent cells. We call this structure the one-sided, one-dimensional (1D) cavity design to distinguish it from the double-sided cavity of Figure 3.26. The primary function of the walls is to isolate the field inside each cell, suppressing the guided mode and supporting the cavity resonance. Extensive finite-difference time-domain (FDTD) simulations considering all known dielectric layers in CMOS stack-up have been performed to achieve optimized structures in one- or two-sided cavities. As the electric field patterns show, while for the TE polarization, there is a strong field enclosed by the cavity, the wave in the TM polarization is coupled to the interface and can hardly propagate up to half of the structure.

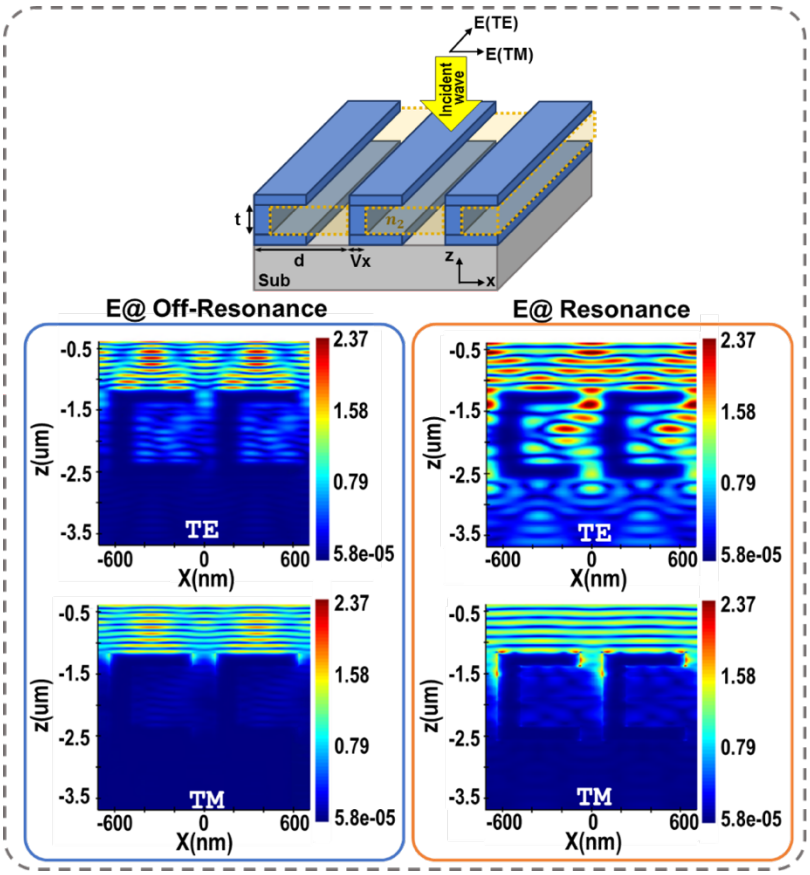

Figure 3.25: Ones-sided 1D cavity structure and simulated E field in TE/TM polarizations.

Choosing a large enough lateral distance between adjacent cells minimizes the overlap of the effective transmission cross-section of cavities [81, 82]. This results in less coupling between the resonant cells and avoids propagative wave hopping from one cavity to another; hence the angle dependency due to the guided mode is reduced. Similar to the waveguide structure, closing the cavity by decreasing the aperture size reduces the spectral bandwidth; however, the response of the cavity can be narrowband in λ and broader in the θ. This is achieved since this resonance mainly depends on the opto-geometrical properties of the cavity, and the incident angle plays a minor role. As we will see in the simulations (next chapter), the main effect of the incident angle variation is the change in the strength of the resonance and not the resonance wavelength [78].

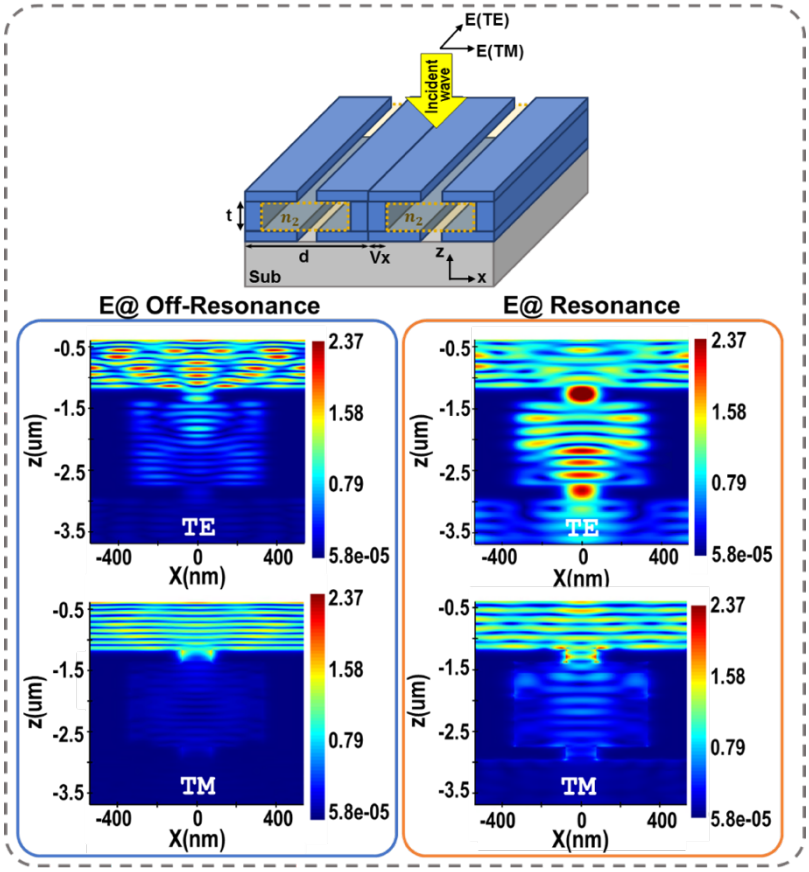

Figure 3.26: Double-sided 1D cavity structure and simulated E field in TE/TM polarizations.

3.5 Receiver Readout Methods:

In this section, we briefly review the main choices for the front-end circuitry to convert the electrical current resulting from the photodiode to a voltage. Resistive trans-impedance (R-TIA) is the most common optical receiver used when a steady light level is present. Using a resistor in the feedback path of an amplifier, this circuit continuously converts the generated current of the photodiode to voltage and samples the result over time. When the signal of interest is small, the receiver must provide high gain, which translates to a large resistor R in the feedback. In addition to a large area associated with a big resistor, the thermal noise of R can overwhelm the small signal of interest. The electrical current resulting from fluorescence sensing includes multiple components as below:

$$I_{PD} = I_{FP} + I_{Dark} + I_{Background} + I_{Excitation} \quad (3.21)$$

in which the signal of interest (I_{FP}) is much smaller than other components, which can cause fast saturation of the receiver.

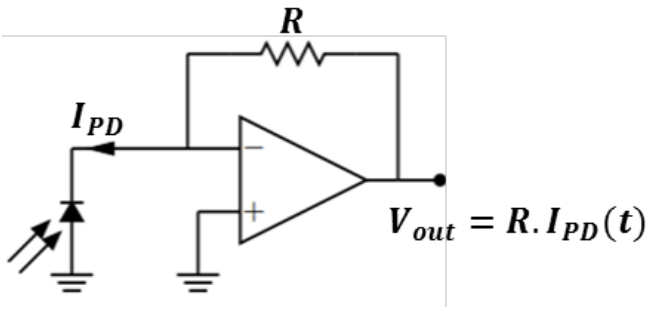

Figure 3.27: Resistive trans-impedance receiver.

Capacitive trans-impedance (C-TIA) is the preferred choice for the optical receiver when measuring a low-level light in the presence of a significant background signal. The receiver's gain is controllable using two parameters, integration time T_{int} and the capacitor in the feedback. This design is more area efficient since a higher receiver gain is achieved by using a smaller capacitor. Increasing the integration time improves the signal-to-noise ratio (SNR), resulting in higher receiver sensitivity when measuring a small fluorescence signal.

The circuit shown in Figure 3.28 includes the C-TIA and the sample-and-hold block and works in two main phases. In the reset phase, the feedback switch is connected, which places the first amplifier in the unity-gain feedback and resets the integrating capacitor. At the same time, the sample-and-hold circuit holds the previously sampled signal. In the integration phase, the feedback capacitor converts I_{PD} to the voltage V_{int} which is then stored in C_H. Increasing T_{int} to improve SNR has the challenge of receiver saturation, especially when the integrating capacitor is small to provide a high gain. One remedy to this problem, as shown in the next chapter, is to subtract the background light using a variable current source at the input node.

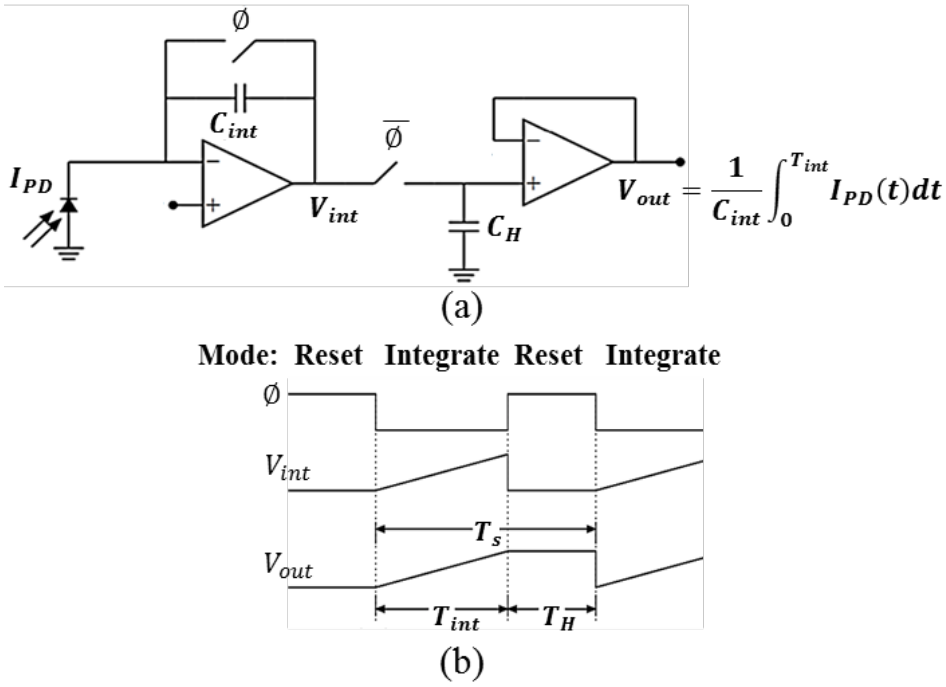

Figure 3.28: (a) Capacitive trans-impedance receiver. (b) General timing diagram of C-TIA.

Chapter 4

SILICON-CELL: DESIGN AND IMPLEMENTATION

This chapter describes the design and implementation of the optics/electronics targeting the Silicon-Cell device. We cover design concepts and insights from the system architecture to the block level. Analysis and simulations are given and explained to understand the reasoning behind our assumptions and decisions.

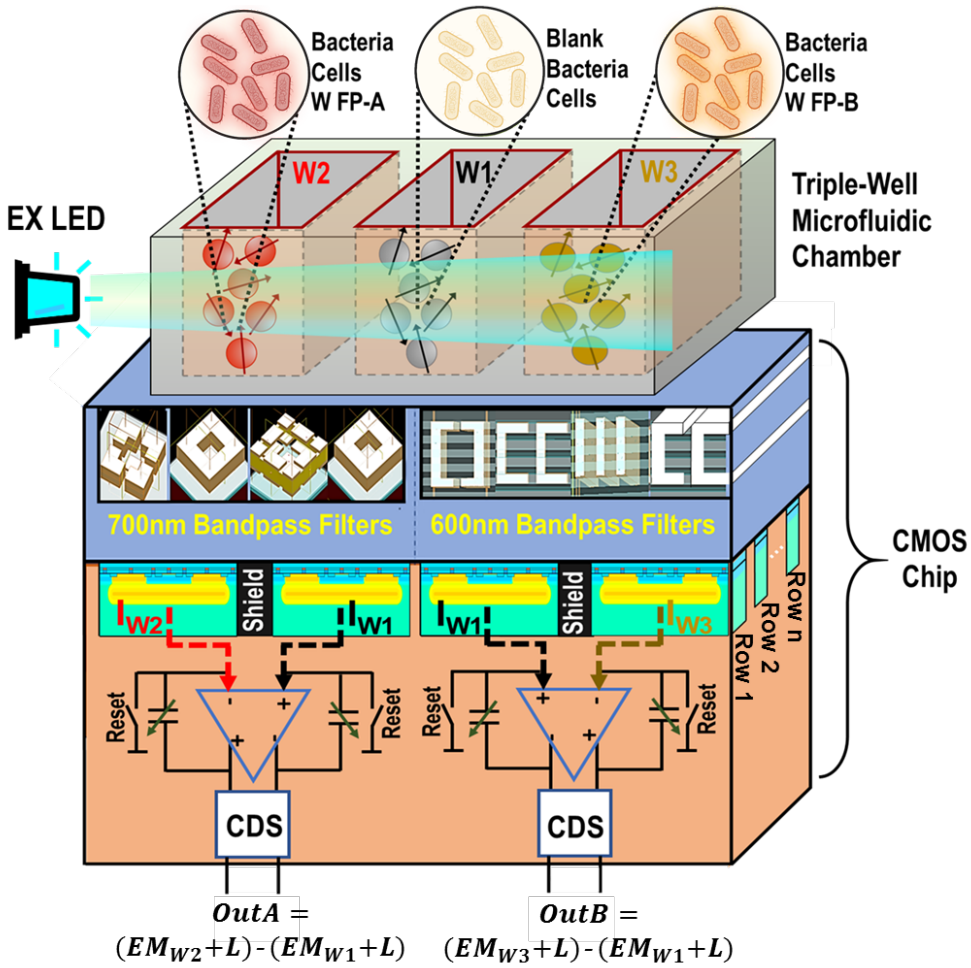

Figure 4.1: Detailed overview of the proposed differential fluorescence sensor, including the CMOS chip and the MF chamber aligned on top.

4.1 System Architecture

An overview of the Silicon-Cell device is shown in Figure.4.1. Revisiting the definition of the fluorescence signal (Figure 4.2), we recognize that fluorescence detection is fundamentally considered a differential operation between blank bacterial cells and engineered cells. Hence, this can be used to relax the stringent optical filter extinction ratio requirement, as explained next. The chip is designed in a complete differential fashion, both in footprint and circuit. The chip's differential floor-planning is done so that it covers three wells where the center well (W1) contains the blank bacterial cells to provide the reference for the differential fluorescence measurements of the right/left wells. This design makes any remaining excitation light leakage appear as a common-mode signal between two adjacent wells and uses the differential front-end circuitry to reject it. Furthermore, since any control loop requires measuring at least two substances, the reference and the target, the sensor is designed to detect two fluorescent proteins simultaneously. The next section will describe the design and implementation of different sensor parts, including optical filters, photodiodes, and CMOS circuitry.

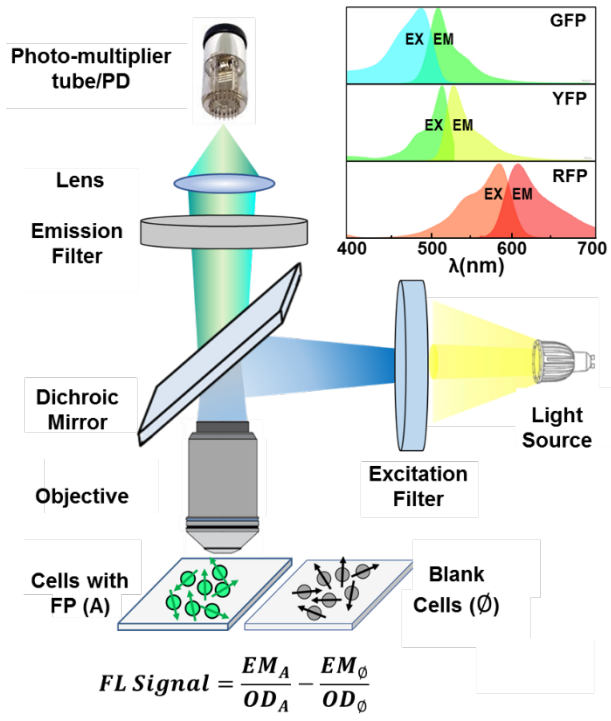

Figure 4.2: Revisiting fluorescence measurement principle as a differential detection.

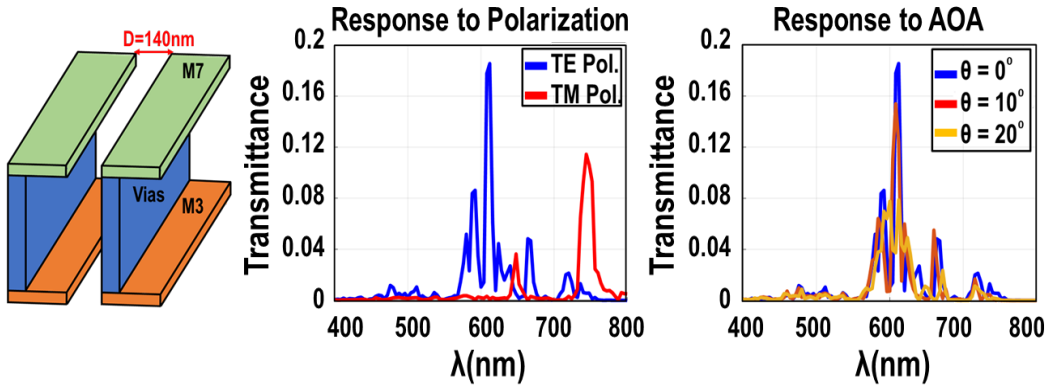

Figure 4.3: 1D cavity implemented in CMOS and its response to the variation of polarization and angle of arrival.

4.2 Bandpass Integrated Optical Filters in CMOS

4.2.1 1D Filters With 600nm Passband

Following the concept of the cavity optical filters from the previous chapter, the 1D cavity resonator is shown in Figure 4.3. It is implemented between CMOS metal layers M7-M3 and using dense via arrays as vertical walls. Using FDTD simulations, the response of the one-sided cavity to the polarization and angle of arrival (AOA) variation is shown in Figure 4.3. As expected, the primary transmission peak located at lower wavelengths is due to cavity mode at TE polarization, and TM response happens at higher wavelengths where the loss of copper is lower. Furthermore, we observe that variation of the incident angle (θ) primarily results in the variation of the resonance peak intensity rather than its wavelength.

4.2.2 Polarization-Insensitive 2D Filters With 700nm Passband

To achieve polarization-insensitive optical filters, geometrically symmetric structures are required. By converting the mentioned 1D cavity to a fully symmetric structure, the 2D hollow square design of Figure 4.4 (a) is achieved. Due to the minimum enclosed area rule enforced by DRC, the central open area of this cavity is forcibly large, causing the filter's response to be very wideband in the wavelength of interest.

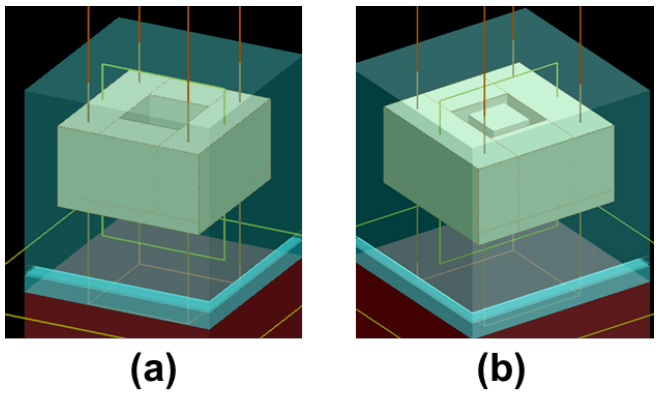

Figure 4.4: (a) 2D hollow cavity. (b) 2D coaxial cavity.

Alternatively, the 2D coaxial design [85] supporting the cavity mode in the coaxial aperture is considered next (Figure. 4.4(b). The coaxial structure was first designed and simulated using metal layers M1 and M2 to see the response we could achieve while using minimum metal. Even though with the selected dimensions, as shown in Figure 4.5, there could be a strong resonance at 670nm, the CMOS DRC doesn't allow this design. By DRC, w1 needs to be larger than 210nm to satisfy the minimum metal area, and w2 must be larger than 150nm due to the minimum enclosed area rule. With these constraints on the dimensions, the resulting resonance has a wavelength at the far end of the visible spectrum with low intensity. Therefore, we must explore other solutions for a polarization-insensitive bandpass filter with a reasonable signal level.

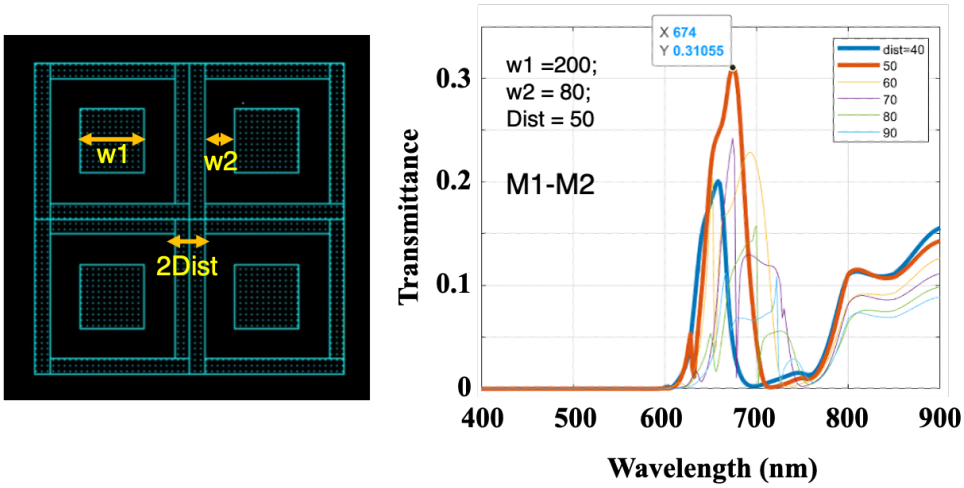

Figure 4.5: Layout and simulation result of a 2D coaxial cavity implemented between M1-M2 layers.

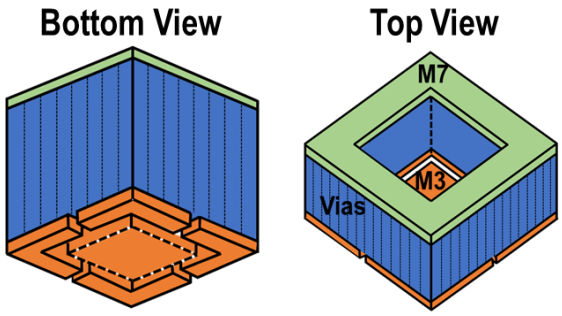

Figure 4.6: The proposed 2D cavity implemented in CMOS.

Considering the combination of the two mentioned structures, one very wideband and the other very lossy, we achieve the new cavity as shown in Figure 4.6, which works by the following reasoning. The symmetric geometries can only resonate at a wavelength where both TE and TM polarizations can propagate.

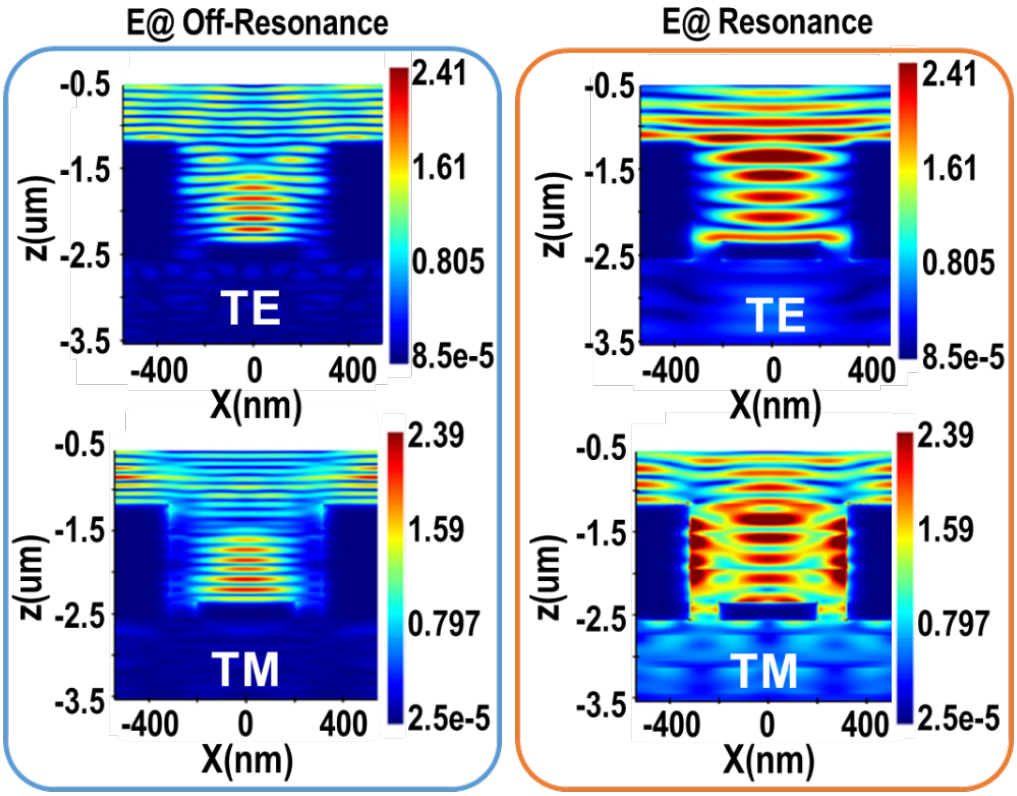

Figure 4.7: Simulated E field in TE/TM polarizations for the proposed 2D cavity implemented in CMOS.

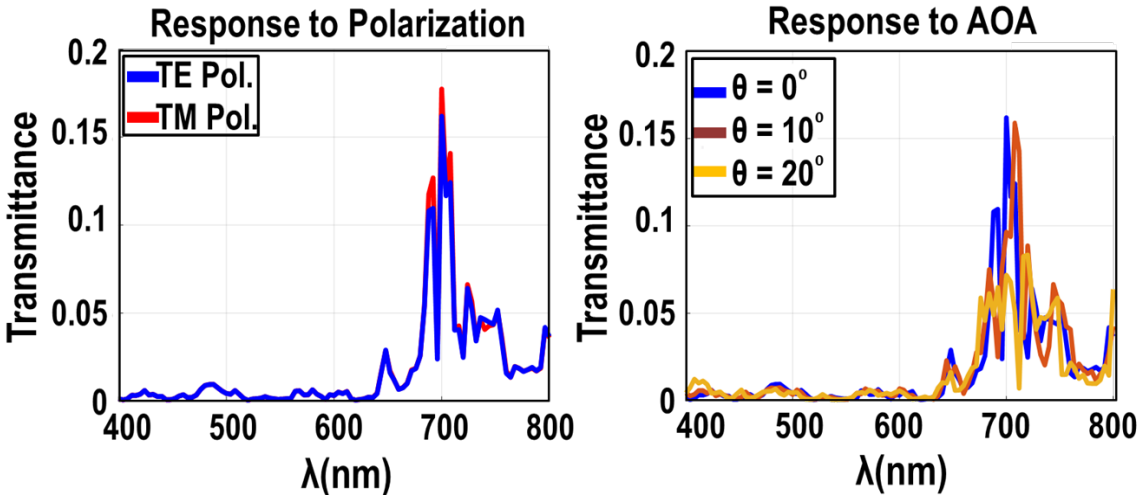

Figure 4.8: Response of the proposed 2D cavity filter to the variation of polarization and angle of arrival.

Therefore, to make the coaxial structure a viable filter, the loss associated with its TM transmission must be lowered, possibly by minimizing the total metal usage of the design. However, we know a large lateral distance between cavities is still required for a low-angle dependency. Hence, we surmise that the use of central metal should be reduced while the surrounding metal is kept wide. Nonetheless, due to DRC rules, the minimum area of the central metal in the XY plane still causes high loss for a cavity implemented between M3-M7 layers. Therefore, by keeping the central metal just in the lowest layer (M3), the metal usage in the Z direction is lowered, allowing transmission of both TE and TM polarizations.

As the simulated electric field patterns show (Figure 4.7), at TE polarization, a cavity mode exists in the coaxial gap, and in TM polarization, the field is coupled to the external metal interface. The simulated response of this 2D cavity to the variation of the polarization and AOA is shown in Figure 4.8, confirming its polarization-insensitive response and tolerance to 20 degrees of AOA variation without creating new resonance peaks.

4.3 Integrated Photodiode Design in CMOS

The standard CMOS process is the most cost-effective silicon technology, making integrating complex systems into one platform feasible. Realizing the photodiodes (PDs) in

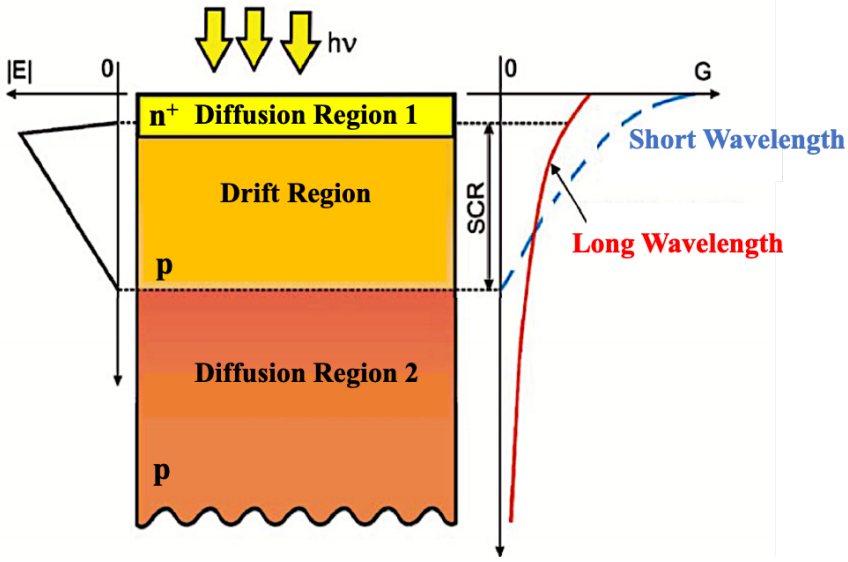

Figure 4.9: Drift and diffusion regions with the photodiode's electric field and photo-generation distribution characteristics.

CMOS using several doped layers available in the process is well-established. However, advanced CMOS technologies continue to shrink the channel size to increase the speed of the circuits, and in doing so, the doping level of layers increases which is not a desirable outcome for PD realization. A high level of doping for P and N layers makes the width of the PD's space-charge region small, resulting in an inefficient design due to the required large penetration depth of light in silicon. Therefore, exploring deeper junctions to increase the PD's responsivity at longer wavelengths is essential [86].

Moreover, as the technology scales down, the number of metal /dielectric layers increases, which causes more optical reflection and interference within the stack, decreasing the optical quantum efficiency and responsivity. Additionally, it is essential to use minimum metal layers to route the PD's signal while satisfying the metal density rule and not covering the PD's active area with light-absorbing metal.

4.3.1 NW/Psub Photodiode

The CMOS process offers various N/P doping layers such as source, drain, N-well, and P-substrate for creating a PN junction needed for a photodiode. The NW/Psub photodiode is

the most popular choice in CMOS and is designed and simulated using TCAD Synopsis tools. The doping concentration and simulated responsivity of this PD are shown in Figure 4.10.

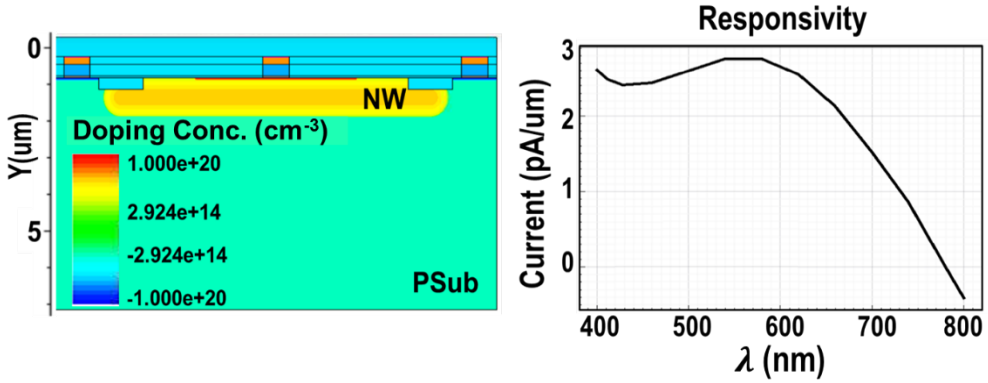

Figure 4.10: Psub/NW PD design and responsivity.

While designing this PD, we noticed that we could use the silicon's wavelength-dependent absorption length, the length a photon needs to travel into the silicon to get absorbed and generate an electron/hole pair contributing to the electrical current (Figure 4.11). The simulated optical generation of the designed PD at short and long wavelengths confirms that the density of the electron/hole pairs generated from absorbed photons at 400nm is maximum at areas close to the surface of the substrate. On the other hand, for longer wavelengths, photons must travel more deeply in the substrate to be absorbed and generate carriers (Figure 4.12).

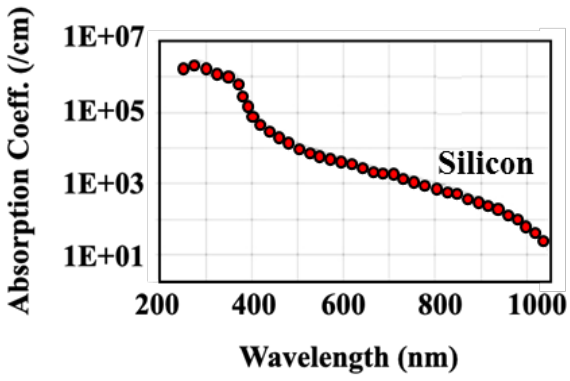

λ(nm)	(1/α)
400	83 nm
500	565 nm
600	1.7um
700	4.5um
800	9.7um

Figure 4.11: Silicon absorption coefficient and absorption length.

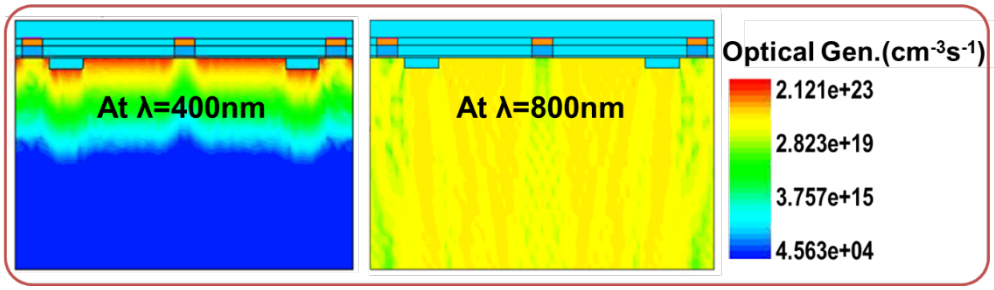

Figure 4.12: Different profile of the optical generation for the Psub/NW PD at short and long wavelengths.

4.3.2 N+/PW/DNW Photodiode

The observation about the wavelength dependency of silicon light absorption led to the design of a triple junction vertical PD of N+/PW/DNW, as shown in Figure 4.13. The shallow junction made of an N+ layer on top of the PW is used to collect and discard the short wavelength light, which helps in providing another level of optical filtering around 400nm. The two deeper junctions of PW/DNW and DNW/Psub convert the mid and high wavelengths of light to the electrical current.

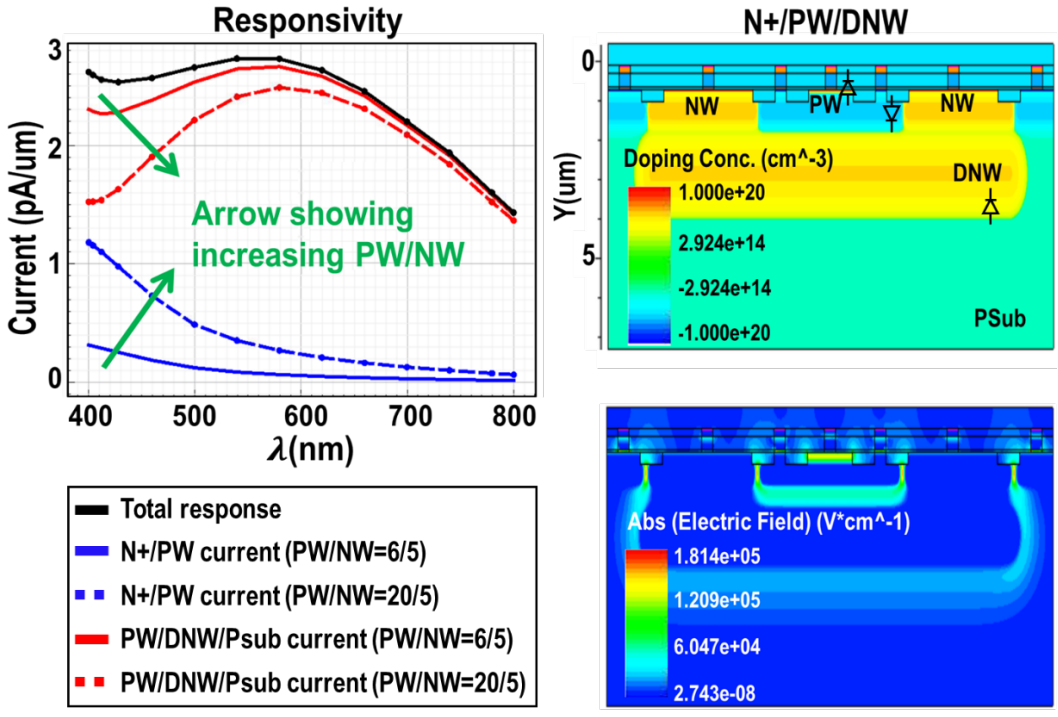

Figure 4.13: N+/PW/DNW PD design, responsivity, and E field.

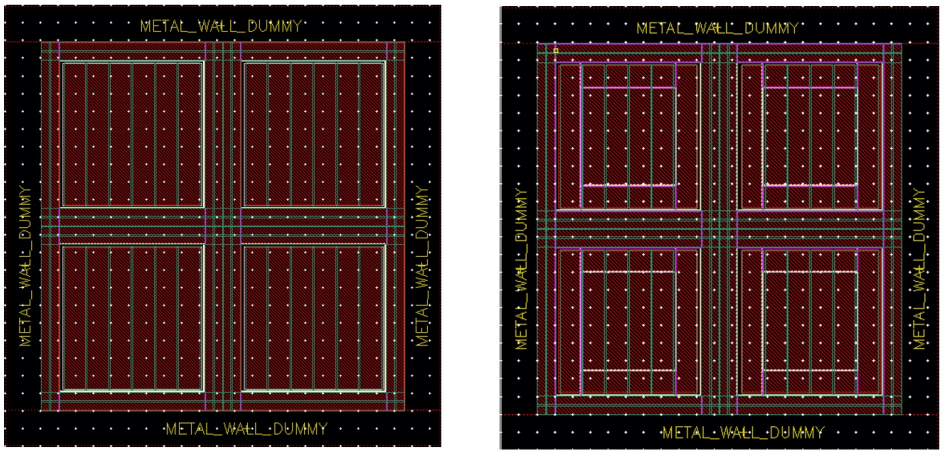

(a) **(b)**

Figure 4.14: Layout of (a) NW/Psub, (b) N+/PW/DNW.

As shown in Figure 4.13, increasing the PW/NW area in a fixed DNW dimension results in a more passband response for this PD. Moreover, for both PDs, the dark current is minimized by optimizing their depletion layers dimension and noting that the primary current contributor for the PD working at a slow speed is the diffusion process rather than the drift, while most of the dark current is generated in the depletion region.

Figure 4.14. shows the layout of the two designed PDs. Each unit cell has a dimension of 50x50um, and each PD has 4 units for a total PD area of 100x100um. Additionally, each PD is surrounded by minimum metal dummy layers for isolating photodiodes from each other and satisfying the density rules, helping to avoid heavy metal usage in the PD active area.

4.4 Sensor Circuitry and Architecture

The architecture of the CMOS fluorescence sensor is shown in Figure 4.15. The chip contains 6 rows of front-end circuitry to process the signal of various optical filters and PDs, which are placed differentially between the chip's center and right/left columns. In each row, a capacitive trans-impedance amplifier (C-TIA) with a variable capacitor bank in the feedback is used to convert the differential PD current to voltage. A correlated double sampler (CDS) block samples the buffered output of the C-TIA twice to remove the offset and the low-frequency correlated noise components [87].

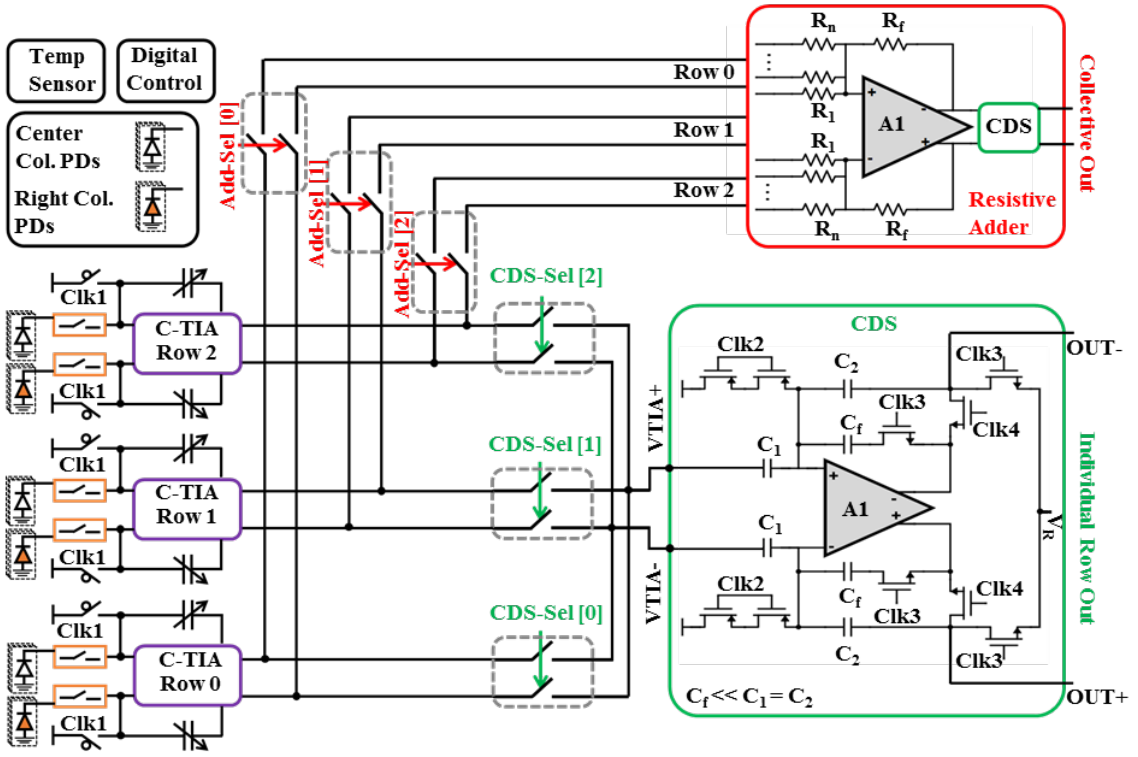

Figure 4.15: Architecture of the CMOS fluorescence sensor circuitry, showing 3 rows of C-TIAs, CDS, and adder blocks.

One CDS block is shared for every 3 rows using CDS-Sel switches to save area and reduce power consumption. Additionally, a resistive adder block is designed to combine the response of several rows of the chip to gain a stronger signal, if desired. The sensor also includes an on-chip temperature sensor, a clock generator, and a digital scan chain block to distribute all the digital control bits of the circuit.

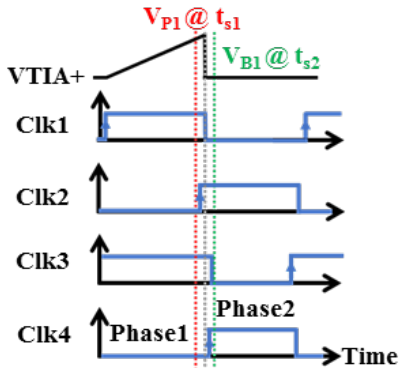

Figure 4.16: The circuit timing diagram.

4.4.1 Correlated Double Sampler Circuit Design

The timing diagram of the circuit is shown in Figure 4.16. During phase 1, the C-TIA integrates the PD current on the feedback capacitor bank resulting in a sawtooth voltage (VTIA), while the CDS circuit is in reset mode. Next, during phase 2, C-TIA is in reset mode while the CDS output is ready to use. The CDS takes the first sample at the end of phase 1 (t_{s1}), storing the peak value of the VTIA+ /VTIA- (V_{P1}, V_{P2}) on C_1 capacitors and the second sample at the beginning of phase 2 (t_{s2}) to capture the lower value of the VTIA+/- waveforms (V_{B1}, V_{B2}). Writing the charge conservation equations at these two sampling times at the input nodes of the CDS, we get the following equations:

$$Q_{IN+}(t_{s1}) = Q_{IN+}(t_{s2}) \tag{4.1}$$

$$C_1(V_{CDS} - V_{P1}) + C_2(V_{CDS} - V_R) + C_f(V_{CDS} - V_{OUT-}) \\ = C_1(V_{IN+} - V_{B1}) + C_2(V_{IN+} - V_{OUT-}) \tag{4.2}$$

and

$$Q_{IN-}(t_{s1}) = Q_{IN-}(t_{s2}) \tag{4.3}$$

$$C_1(V_{CDS} - V_{P2}) + C_2(V_{CDS} - V_R) + C_f(V_{CDS} - V_{OUT+}) \\ = C_1(V_{IN-} - V_{B2}) + C_2(V_{IN-} - V_{OUT+}) \tag{4.4}$$

Defining the differential amplitude of VTIA as:

$$V_{Diff} = [(V_{P1} - V_{B1}) - (V_{P2} - V_{B2})] \tag{4.5}$$

and substituting $(V_{IN+} - V_{IN-}) = (V_{OUT+} - V_{OUT-})/A_{v1}$ and $C_1 = C_2 = C$, we get:

$$V_{Diff} = \left[1 + \frac{2}{A_{v1}} - \frac{C_f}{C}\right](V_{OUT+} - V_{OUT-}) \approx (V_{OUT+} - V_{OUT-}) \tag{4.6}$$

The result in (4.6) shows that the output of the circuit is the differential signal of the C-TIA free from the offset. Even though the small C_f in the feedback path of amplifier A_1 is used mainly to avoid its open-loop configuration at any time, the C_f/C can be chosen to remove

the error associated with the finite open-loop gain of the OTA (i.e., $2/A_{v1}$).

4.4.2 Front-end Circuit Design

The detailed circuit diagram of each sensor row is shown in Figure 4.17. The differential C-TIA can be connected to one or multiple PDs using designed low-leakage switches. The CMOS transistor in its off state has a leakage current that can be larger than the desired input current to the sensor. This leakage is significantly suppressed if the voltage across the switch is kept close to zero. A closed-loop feedback circuit using a compact buffer is designed and shared between 4 switches at each input of the C-TIA. If any of the switches are off, their complement control signal is active, placing the respective switch in the controlled loop.

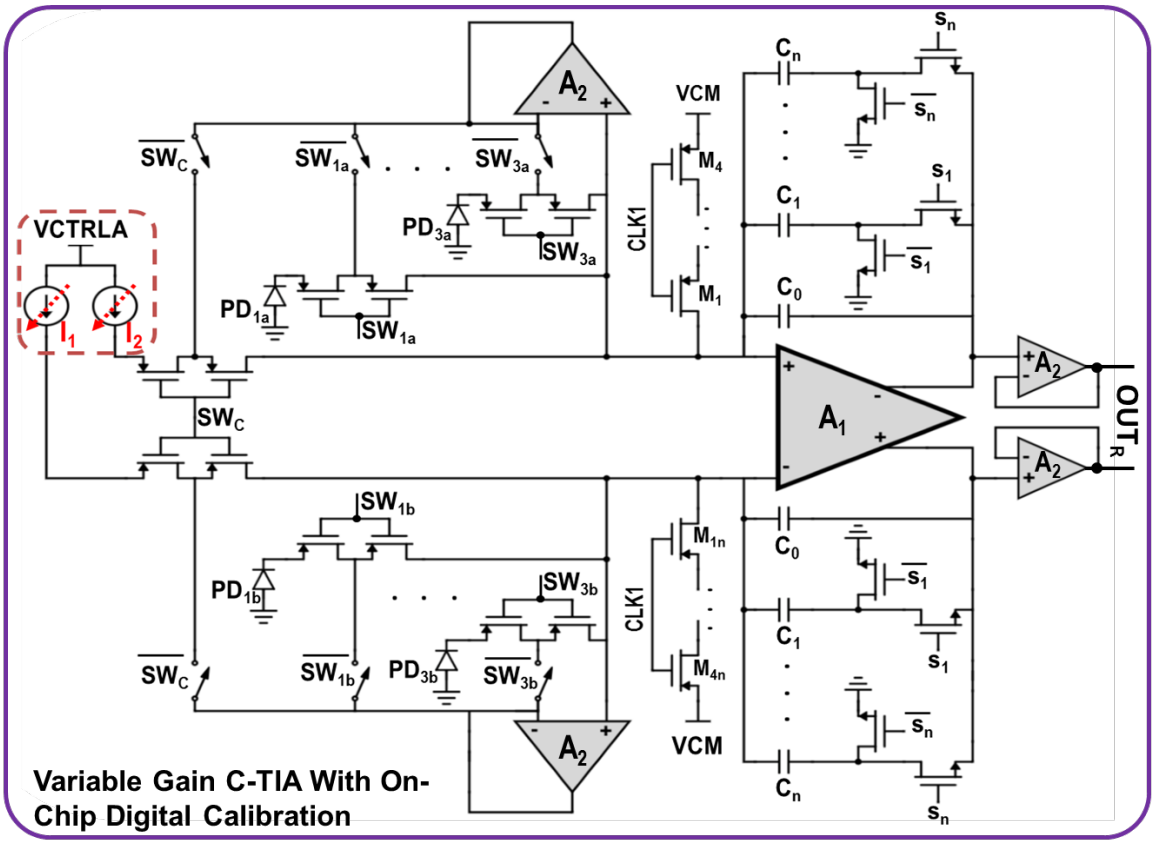

Figure 4.17: Detailed circuit diagram of the variable-gain C-TIA with low-leakage switches.

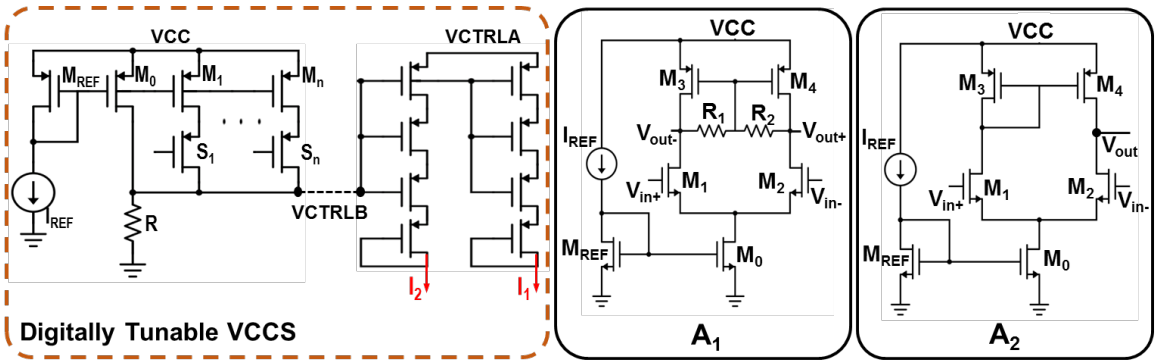

Figure 4.18: Detailed circuit diagram of the digitally tuned VCCS, and amplifiers.

Also, thick oxide transistors are used in the switches to reduce their leakage current further. As previously mentioned, the proposed sensor is designed to measure the fluorescence signal differentially. By making any background light appear as the common-mode signal and suppressing it electronically, the sensor rejection ratio will be drastically improved compared to relying solely on optical filtering. Therefore, using SW_C, one of the inputs in each C-TIA is connected to a tunable voltage-controlled current source (VCCS) to compensate for the common-mode currents originating either from imperfect optical filtering of the excitation light or the common-mode dark current of the PDs. The tunable VCCS is designed using a compact current source with one external course tune (VCTRLA) and one on-chip fine tune (VCTRLB) controlled via 6 digital bits. As the simulation results show, even with the rough removal of the large common-mode current, the circuit's sensitivity is improved, and there is no need for complete current subtraction.

To apply the required fluorescence normalization to the respective OD of each culture in the closed-loop operation, the C-TIA is designed with individually controlled switched capacitor banks to provide independent variable gain for each feedback path. Using switches s_1 to s_n, each capacitor is either placed in the feedback path to contribute to the gain or is in the reset mode connected to the ground. Finally, the output of C-TIA is buffered using low-power A_2 amplifiers to interface with the CDS and adder blocks.

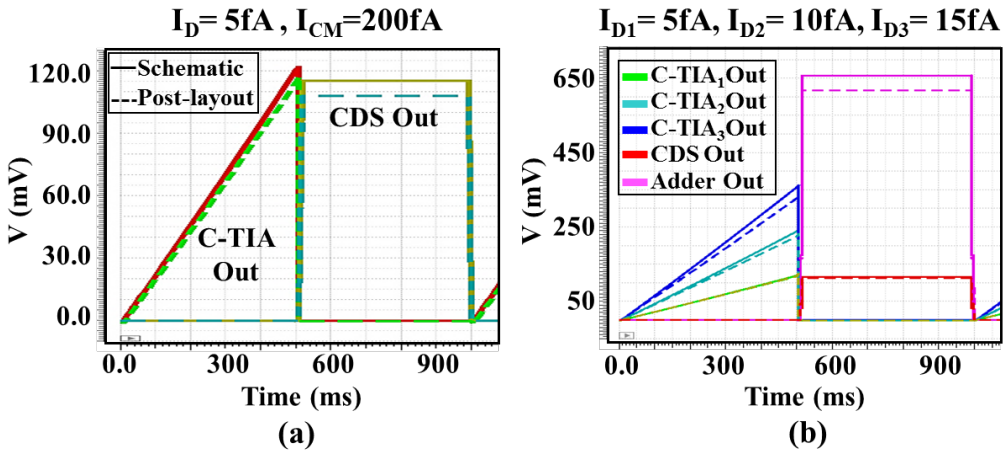

Figure 4.19: (a) An example of the transient waveforms of C-TIA and CDS. (b) Combining the response of 3 rows of C-TIA in the adder.

4.4.3 Circuits Simulation Results

The circuit is simulated at both schematic and post-layout levels to see the effect of interconnect parasitic on the signals. As shown in Figure 4.19, in response to the differential current of 5fA on top of a moderate common-mode current (200fA) and using an integration time of 0.5s, the CTIA integrates the current linearly to achieve the signal peak of 120mV. The CDS then samples the peak value of the sawtooth waveform of CTIA and holds it in a pulse shape. Figure 4.19 shows the signals of 3 individual rows, each with a different input signal level, and the linear addition of those three rows in the resistive adder to achieve a stronger signal.

Figure 4.20 shows the simulation results of the C-TIA and the effects of the variable switched-capacitor bank and VCCS block when a large common-mode current is present. When the LSB capacitor is used to achieve the highest gain settings in the C-TIA, the circuit remains almost linear for the small differential current of I_D=5fA, even for a large common-mode current of I_{CM}=1pA. On the other hand, for a higher differential current (I_D=50fA), the circuit starts to saturate for moderate I_{CM} values. While using an MSB capacitor can mitigate this problem by reducing the gain (Figure 4.20 (b)), the VCCS gives us another degree of freedom in extending the dynamic range of the sensor. As shown in Figure 4.20(c), the circuit

is not entirely linear, even for a small I_D, when a common-mode current of I_{CM}=900fA is present. Using the VCCS to partially compensate for this I_{CM} current, the circuit can provide high gain while staying linear for larger I_D currents (Figure 4.20(d)).

The effect of the CDS block in reducing the sensor's offset is shown using Monte Carlo simulations in Figure 4.21. While the peak output of C-TIA has a standard deviation of > 100mV, the CDS block samples the peak amplitude of the C-TIA and achieves a standard deviation of < 7mV.

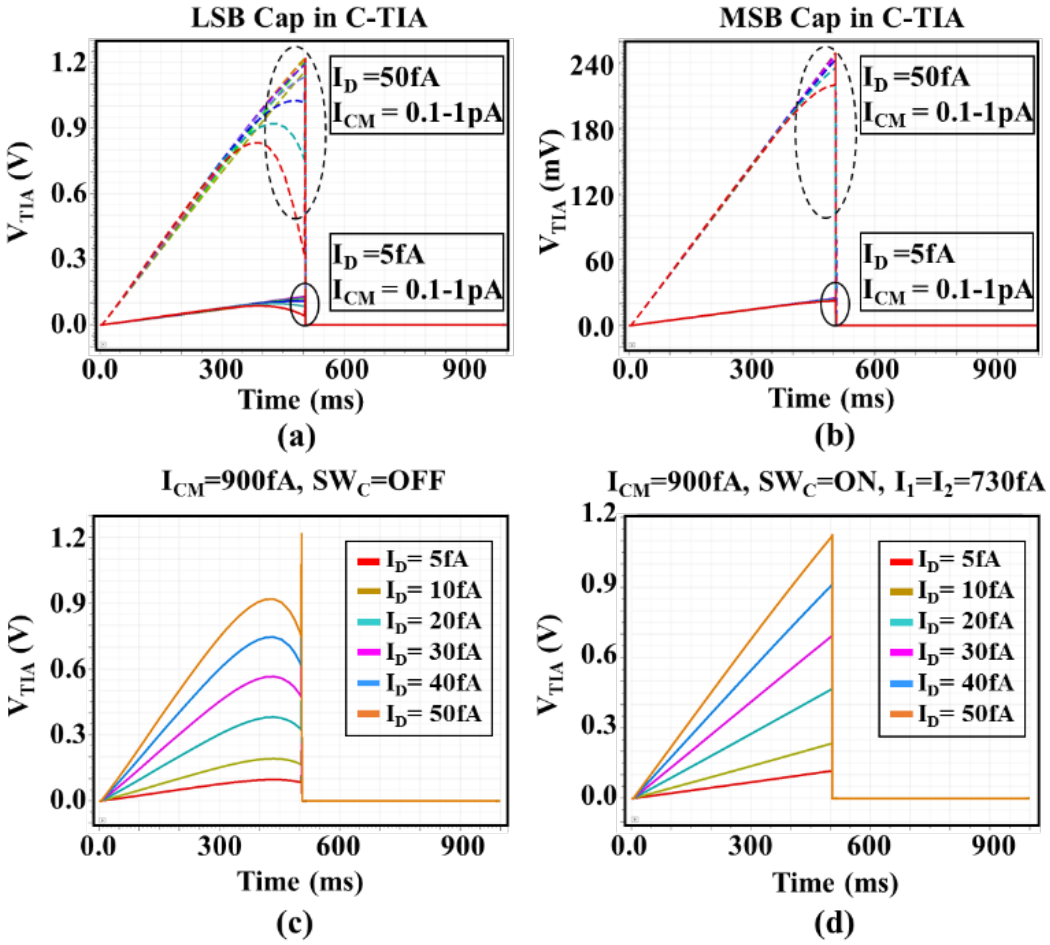

Figure 4.20: C-TIA output with (a) LSB capacitor in the feedback. (b) MSB capacitor in the feedback. (c) Large I_{CM}, without compensation. (d) Large I_{CM}, with partial compensation.

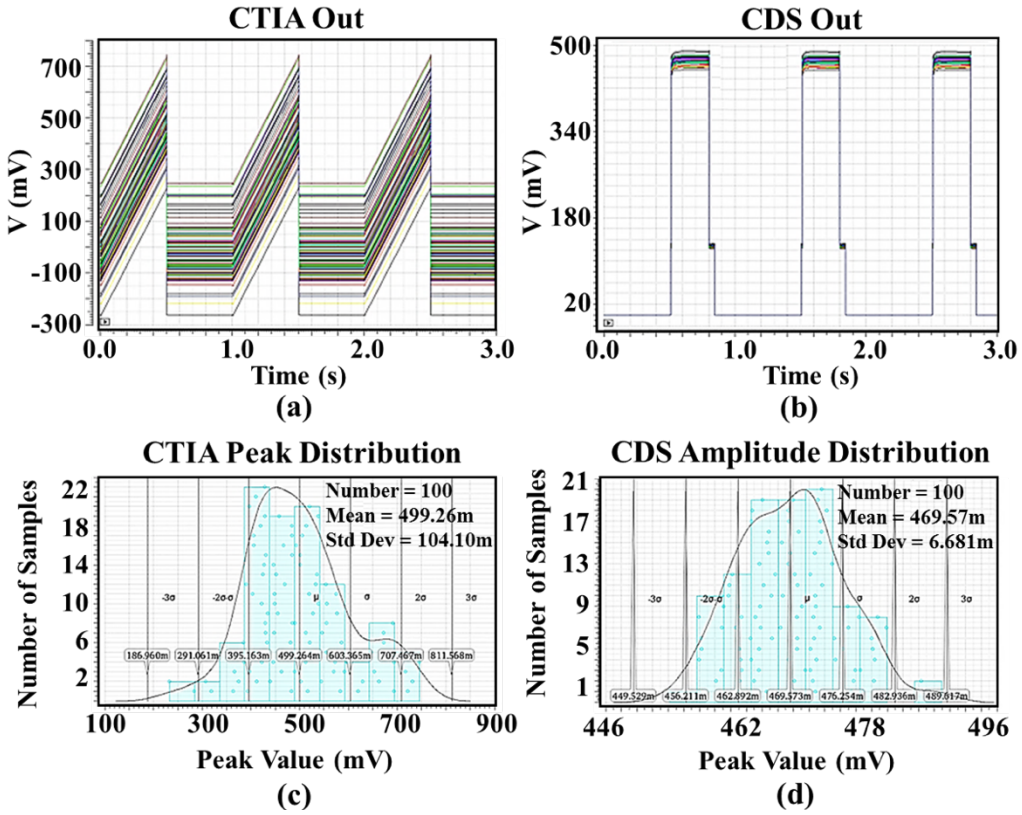

Figure 4.21: Results of Monte-Carlo simulations showing the effect of CDS in reducing the offset of the C-TIA's output amplitude.

4.4.4 Noise Components

The signal-to-noise ratio (SNR) at the sensor input and in the presence of the fluorescence signal is defined in (4.7). The primary noise sources of the sensor are the circuit thermal noise (referred to the input), PD's dark shot noise, and photon shot noise due to fluorescence excitation and emission lights. In the equation, P_F and P_L are the fluorescence emission and excitation leakage, I_D is the dark current, T is the integration time, R_F is the PD's responsivity, and γ is the combined sensor rejection in the optical and electrical domains.

$$SNR \approx \frac{P_F R_F}{\sqrt{I_{Th,in}^2 + 2qI_D/T + 2q\left(P_F + \frac{P_L}{\gamma}\right)R_F/T}} \tag{4.7}$$

Since the most dominant noise source during fluorescence measurement is the photon shot noise, (4.7) can be simplified to:

$$SNR \approx I_{in}\sqrt{\frac{T}{2q(I_{in}+I_L)}} \tag{4.8}$$

in which $I_{in}= P_F\ R_F$, $I_L = P_L\ R_F/\gamma$. As seen in (4.8), with the fixed sensor rejection (γ), the SNR can be improved by increasing the integration time (T). A very long T can cause saturation of the front-end by the PDs common-mode current, which is avoided by using the tunable VCCS and switched-capacitor bank in the C-TIA. On the biology side, however, there is a limit on the maximum value of T due to the possible photobleaching of the proteins.

4.5 Chip Layout and Footprint

The layout of the sensor, along with the zoomed view of its one row, is shown in Figure 4.22. Underneath each well are a column for the absolute OD measurement and two PD variations for each filter type. In summary, this chapter described the proposed fully integrated fluorescence sensor in the standard CMOS process for a low-cost biosensor solution. CMOS metal/dielectric layers are used to implement low-loss cavity-type bandpass optical filters. The sensor's sensitivity is enhanced by designing bandpass photodiodes, the sensor's differential measurement scheme resulted in the electrical common-mode rejection, implementing low-leakage CMOS switches, and digitally controllable voltage-controlled current source.

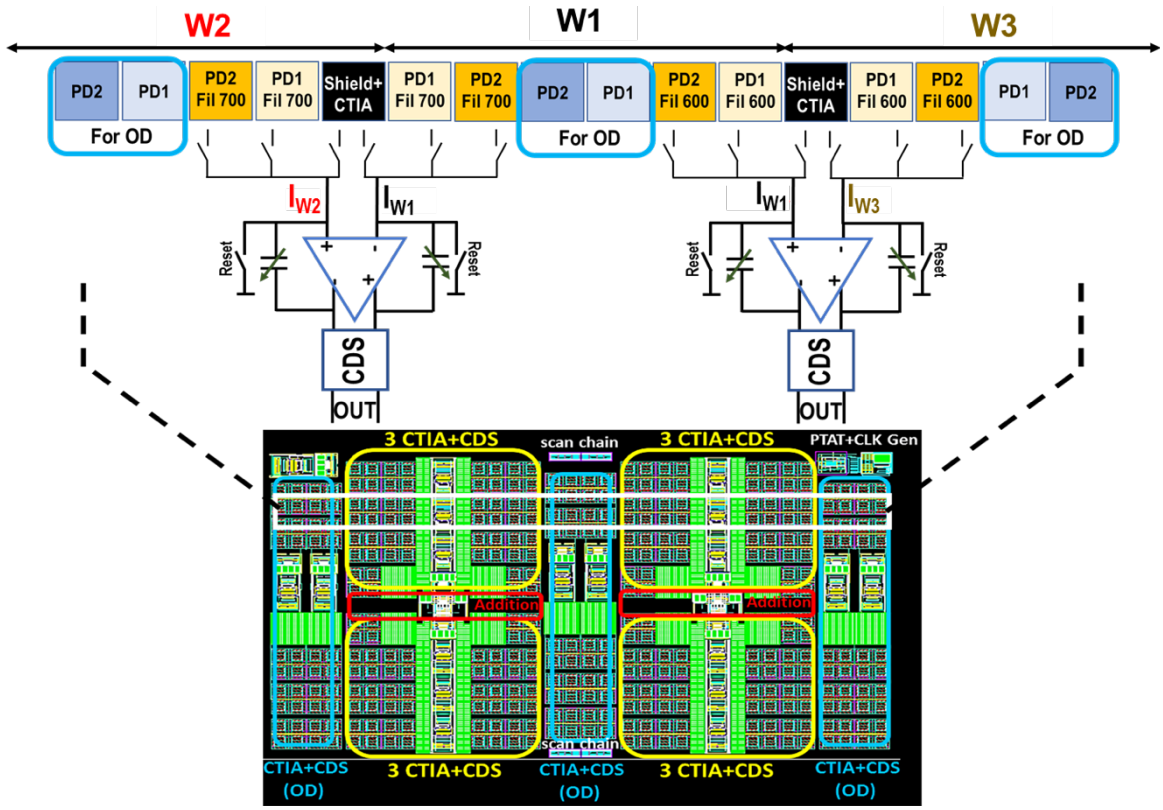

Figure 4.22: The chip layout and a zoomed view of one row of the fluorescence sensor.

Chapter 5

SILICON-CELL: MEASUREMENT RESULTS

This chapter presents the characterization setup and the measurement results of the implemented fluorescence sensor in the Silicon-Cell system. The measurements have been done in optical, electrical, and biological domains. In addition to the static detection of the various fluorescent proteins (individually and in a mixture), continuous dynamic measurements of bacterial cells (OD and fluorescence signal) were performed. The results confirm the functionality of the bidirectional communication between the CMOS chip and engineered bacterial cells.

5.1 Electrical Characterization

The chip is fabricated in a standard 65nm CMOS process, and its die micrograph is shown in Figure. 5.1. The setup shown in Figure 5.2 characterizes the sensor regarding responsivity, sensitivity, and noise. The measured results show that the bare photodiode PD1 achieves the responsivity of 24 mA/W at 700nm while the sensor's responsivity (including an optical filter) is reduced to 1.2 mA/W.

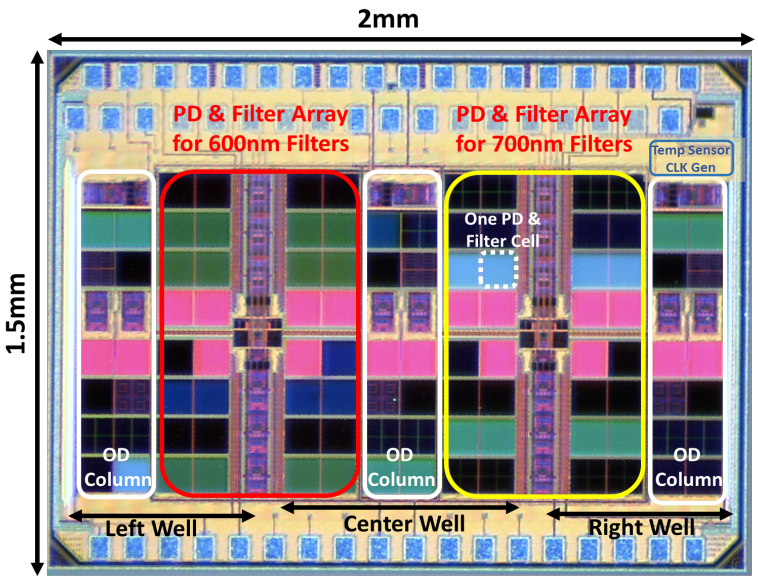

Figure 5.1: 65nm CMOS chip micrograph.

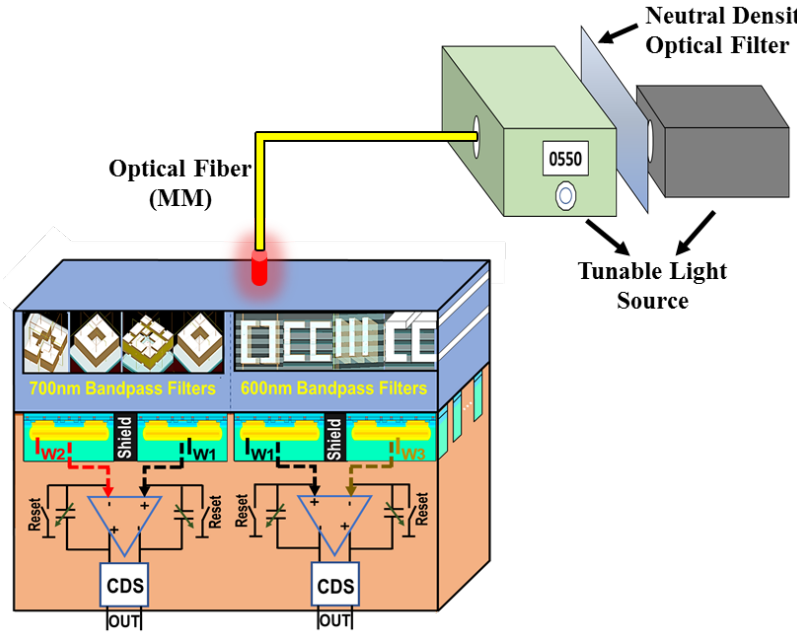

Figure 5.2: Test setup to measure the chip's electrical/optical characteristics.

As observed in Figure 5.3, the sensor can measure a minimum signal level of 1.05fA with >18dB SNR, using C_{TIA}=30fF and an integration time of 1 sec. The sensor noise is measured in dark conditions and during the reset and integration phases. The main noise contributor in the dark and during integration time is the reset switch of the C-TIA. The shot noise of this switch, resulting from its leakage off-current, can be minimized by adding more transistors in series to reduce the effective off-voltage across each transistor.

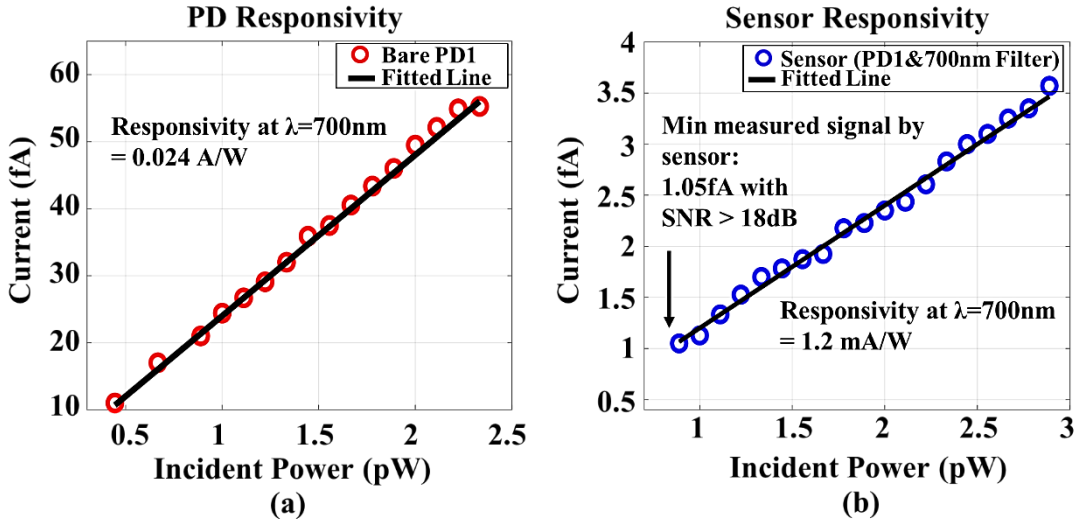

Figure 5.3: Measured responsivity of (a) Bare PD1 at 700nm. (b) Sensor at 700nm.

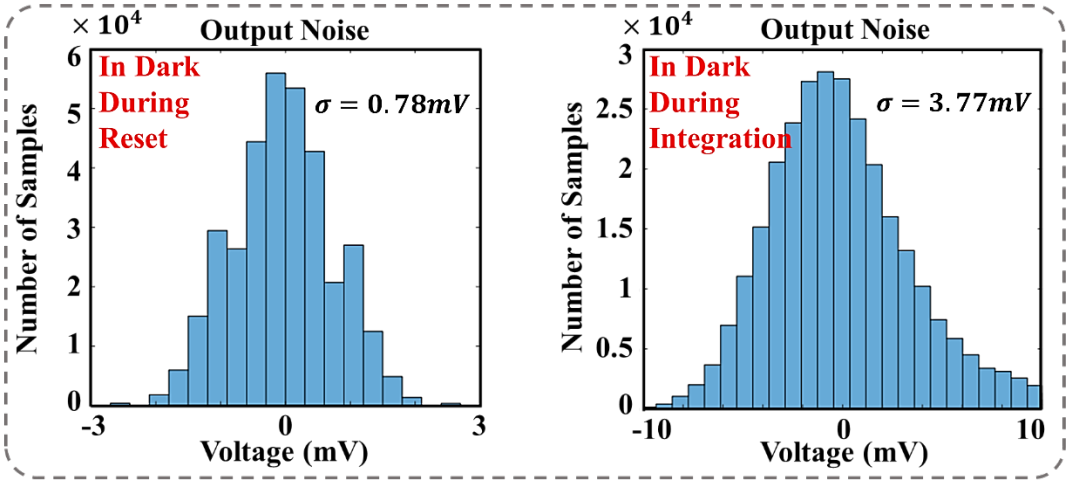

Figure 5.4: Measured noise histogram in the dark during reset and integration.

5.2 Optical Characterization

An unpolarized tunable light source with 6nm bandwidth and a tunable neutral density filter are used for optical measurements. The spectrum of the bare PDs and selected filters is measured by sweeping the light source, as shown in Figures 5.5 and 5.6. As expected, PD2 has higher rejection than PD1 at the lower wavelength range. The filter characterizations using PD1 show that 1D filters have a primary peak at the 600nm range and a second peak at around 700nm. In comparison, the 2D filters have a single peak at the 700nm range, confirming their polarization-insensitive response.

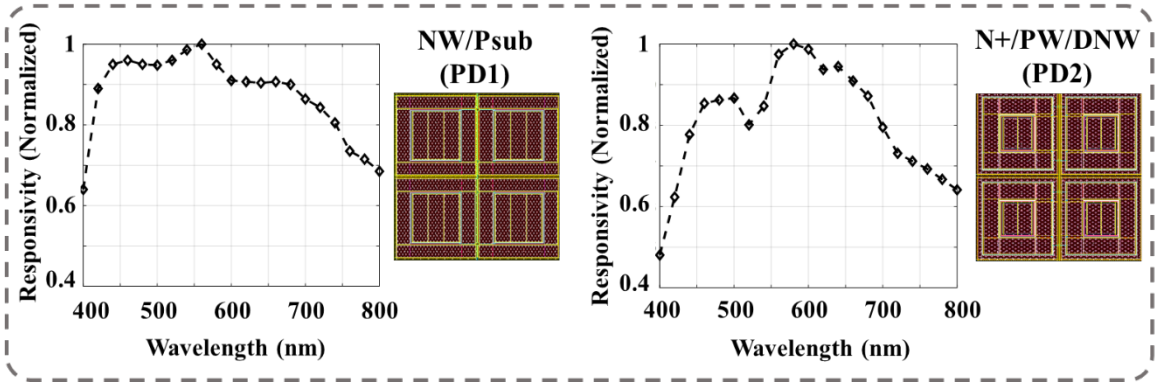

Figure 5.5: The measured spectrum of bare PD1 and PD2.

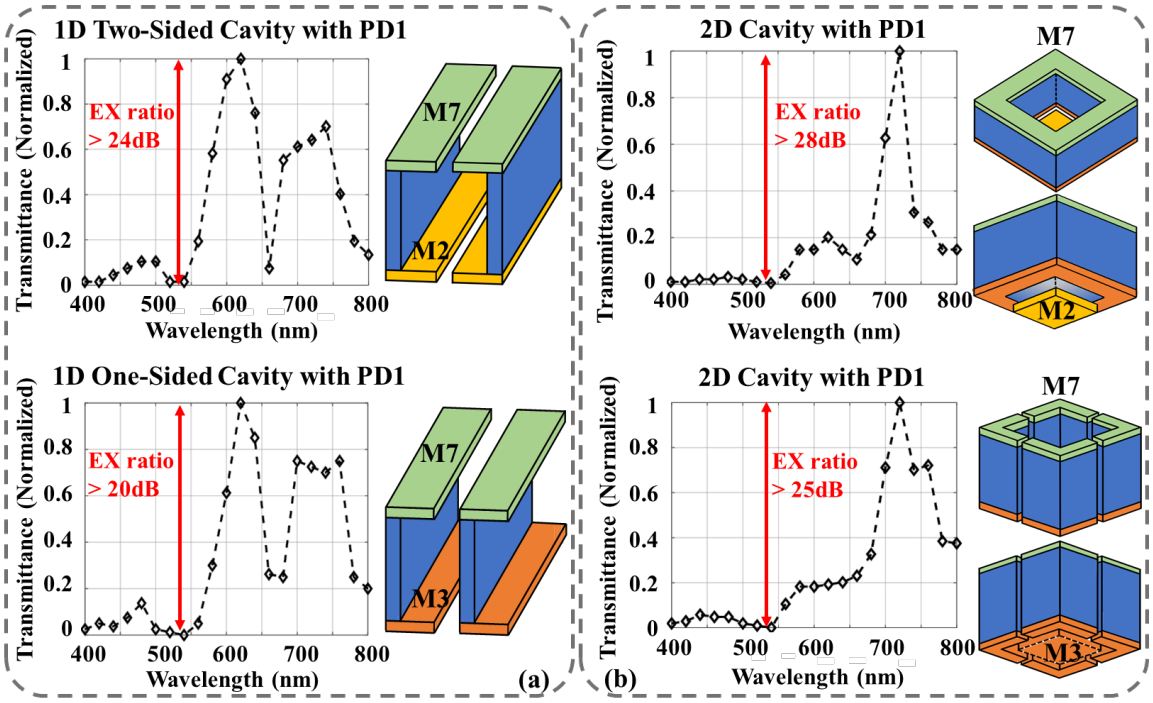

Figure 5.6: The measured spectrum of (a) 1D cavities on top of PD1. (b) 2D cavities on top of PD1.

Before proceeding to the biological experiments, the functionality of the sensor's differential optical measurement is verified using the setup shown in Figure 5.7. The input source power is split and varied by optical attenuators and coupled to two multimode (MM) optical fibers, each shining into one sensor column. In the presence of the LED excitation light from the side, we observe that the chip correctly detects the differential signal using on-chip optical filters and common-mode current removal realized by VCCS.

5.3 Biological Characterization

The setup for the biological measurements is shown in Figure 5.8. A triple-well microfluidic chamber with a 250um channel size and 5/10uL volume for each well is designed and fabricated using a 3D laser printer with bio-compatible resin. A fixture to place the LEDs for OD and fluorescence measurements and the MF chamber is also designed and fabricated in-house. The direct illumination of the fluorescence excitation light to the chip is minimized

by placing it on the side. On the other hand, the red LED for OD measurements is placed on top since this light should directly pass through the cell chamber.

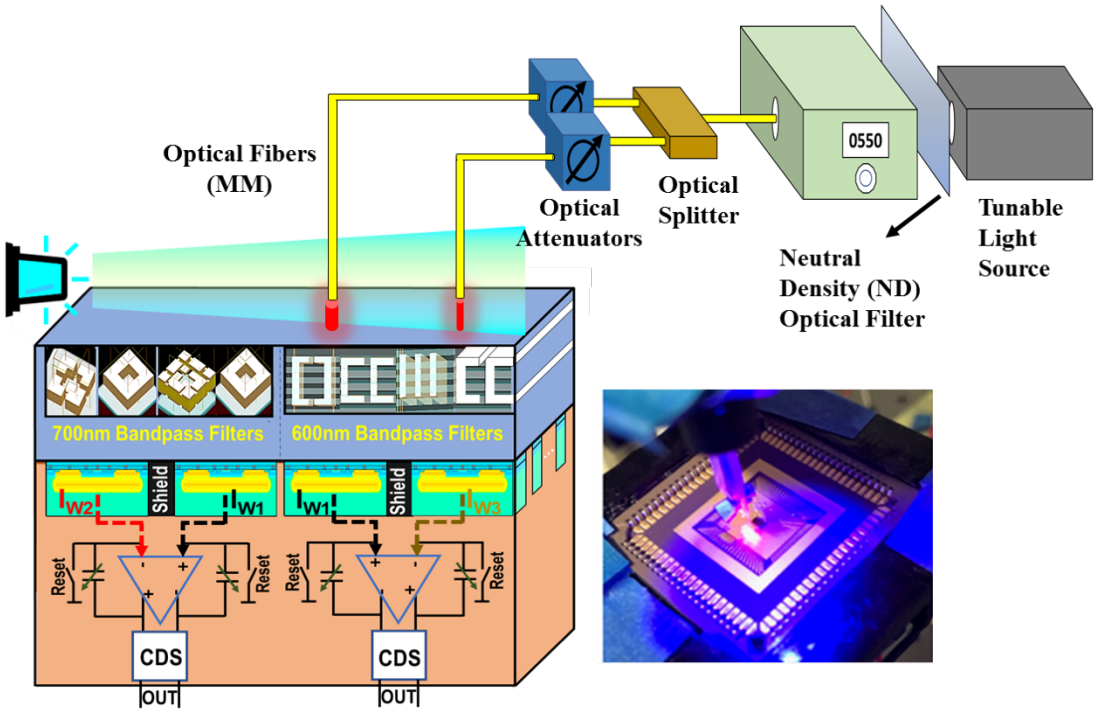

Figure 5.7: Test setup for the differential optical measurement.

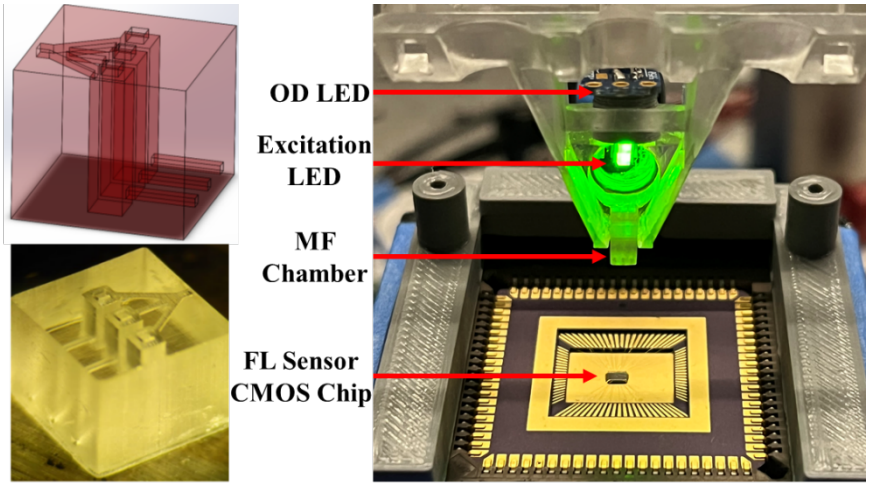

Figure 5.8: Design and fabrication of the MF chamber and the fixture for biological experiments.

5.3.1 Static Measurements

The first biological experiment is designed to detect a single fluorescent protein with low brightness in the 700nm range. A constitutive recombinant fluorescent protein named miRFP [57] with two excitation peaks at 388nm/674nm and an emission peak at 700nm is encoded in living *E. coli* bacterial cells for this experiment. To account for the non-uniform optical properties of the adjacent wells caused by the residual resin and manual cleaning process, we calibrated the setup using blank bacterial cells to establish the baseline. As shown in Figure 5.9, $Vout_1$ is the difference in the emission signal of the two control wells (W1 and W2). The center well (W1) is then replaced by the culture containing miRFP, and the emission is recorded as $Vout_2$. Based on the shown definition in the figure, the red bar indicates the fluorescence response of the miRFP.

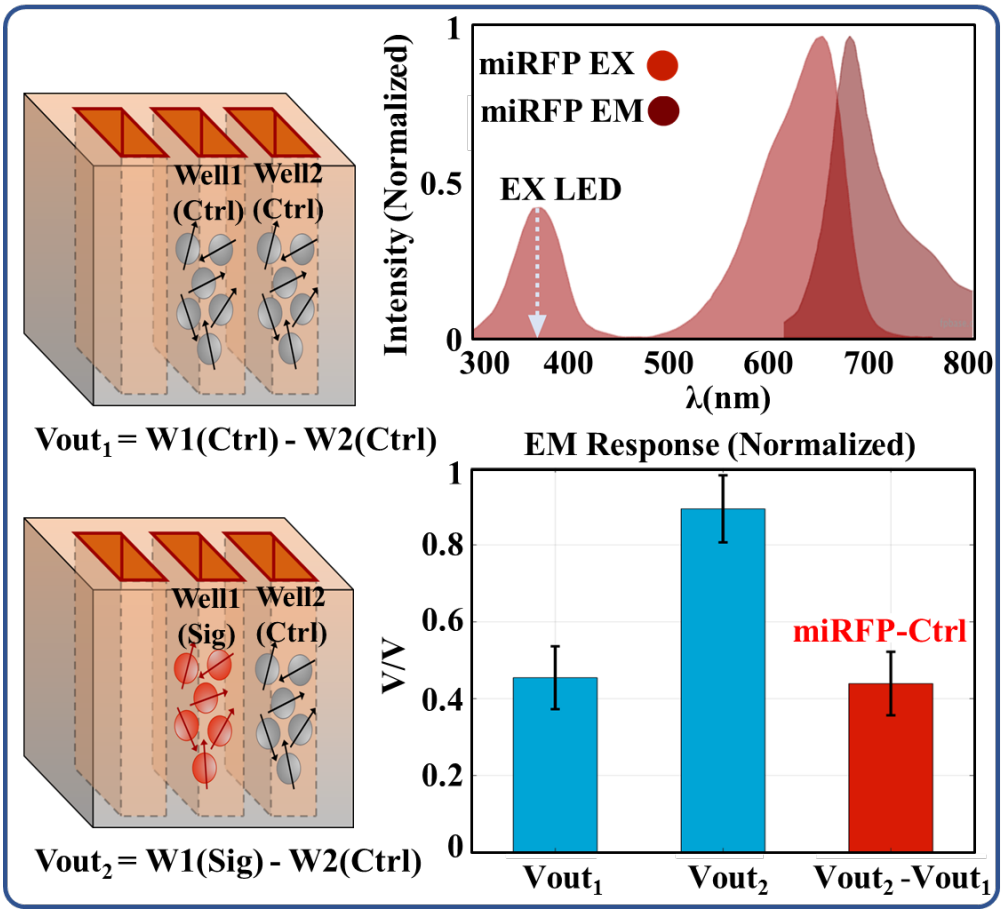

Figure 5.9: Single protein static measurement results.

The next experiment is designed to confirm the ability of the sensor to detect two biochemical signals reported by two fluorescent proteins. The possible crosstalk error can be minimized by selecting two proteins with distinct enough excitation bands and using narrowband LEDs. For this experiment, two plasmids encoding mCherry [88] and LSSmOrange [56] fluorescent proteins, under inducible promoters, are transformed into living *E. coli* cells. We measured the bacterial culture with four different induction profiles using chemical inducers: none, one, or both proteins were expressed (Figure 5.10). By exciting cultures using LED1 and LED2 and observing distinct columns, the expression of a protein in the mixture is deduced. The measured results show that LSSmOrange protein responds to LED1 and mCherry protein to LED2. Additionally, we observe that the signal of the non-responsive protein at each plot is around the baseline, and the response of the culture containing both biochemicals is around the signal of the responsive protein.

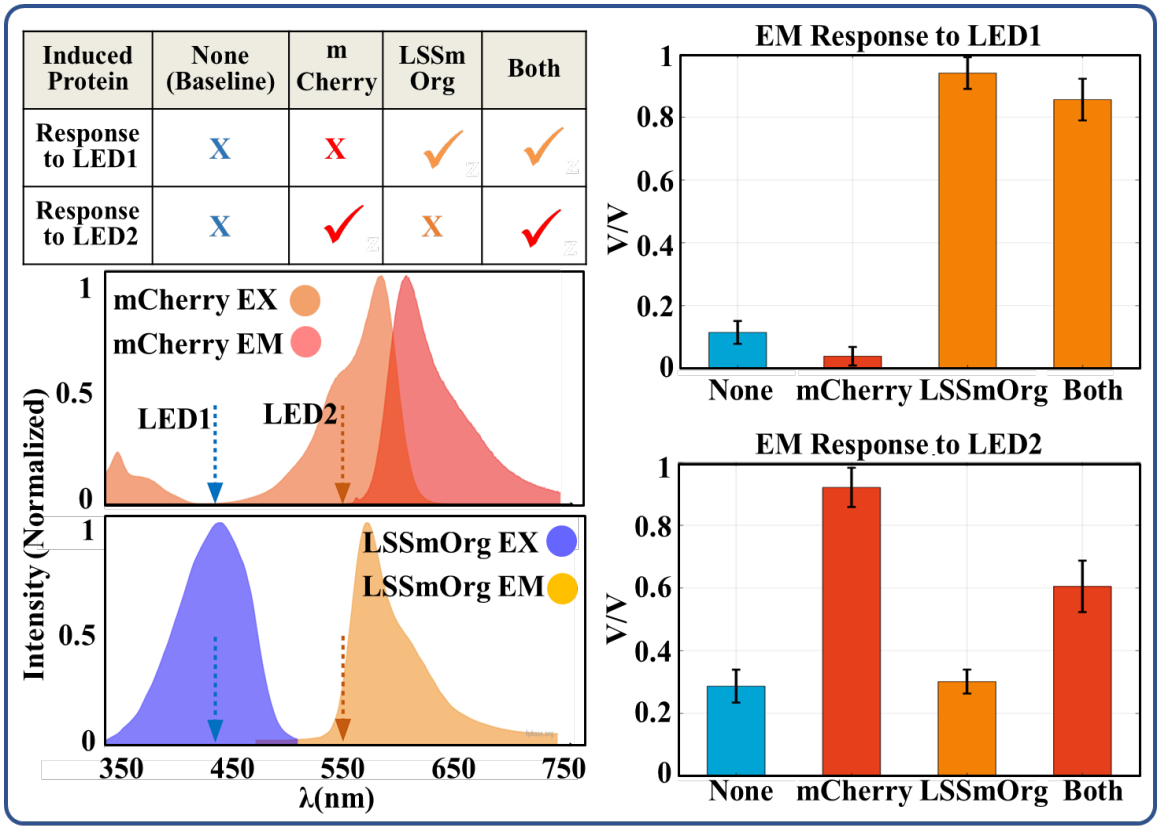

Figure 5.10: Measured results of distinguishing two biochemicals using two fluorescent proteins.

5.3.2 Dynamic Measurements

Observing gene expression dynamics in living cells requires measuring both bacterial cell growth and fluorescence signal dynamics in real-time. To minimize the delay caused by protein folding and maturation, we opted for super-folder YFP (sfYFP [89]), which has a rapid folding rate. Despite the emission peak of sfYFP not entirely being in the filter passband range, the strong brightness of this protein aids its detection in the non-peak wavelength of > 580nm (Figure 5.11). The collective response of multiple rows of the chip and the maximum gain settings are utilized to achieve a robust signal. Furthermore, we employed a 500nm LED for the excitation light, as this wavelength range is a strong dip in the measured filter spectrum and provides high optical filtering.

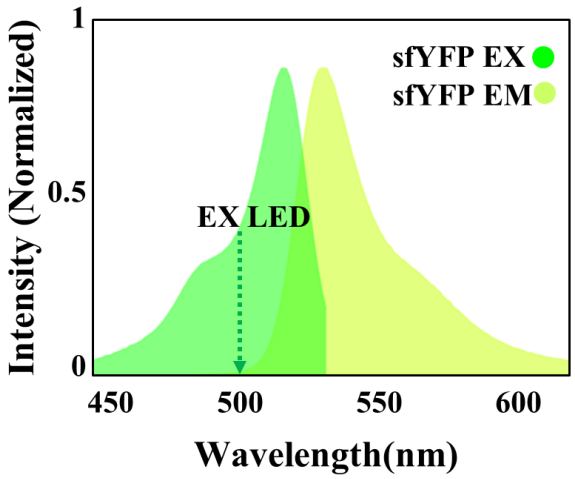

Figure 5.11: Spectrum of sfYFP.

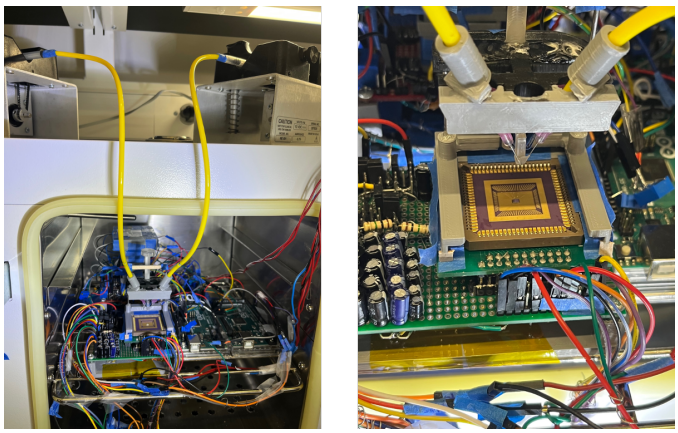

Figure 5.12: Dynamic measurement setup inside the incubator.

Modulating protein expression dynamics is critical in establishing a bidirectional communication link between cells and the CMOS chip. Optogenetic control encoded in the engineered *E. coli* cells allows us to control protein expression using light sources. Figure 5.13 shows that bacterial cells express sfYFP when exposed to a green light, and the fluorescent protein expression is minimal when exposed to a red light.

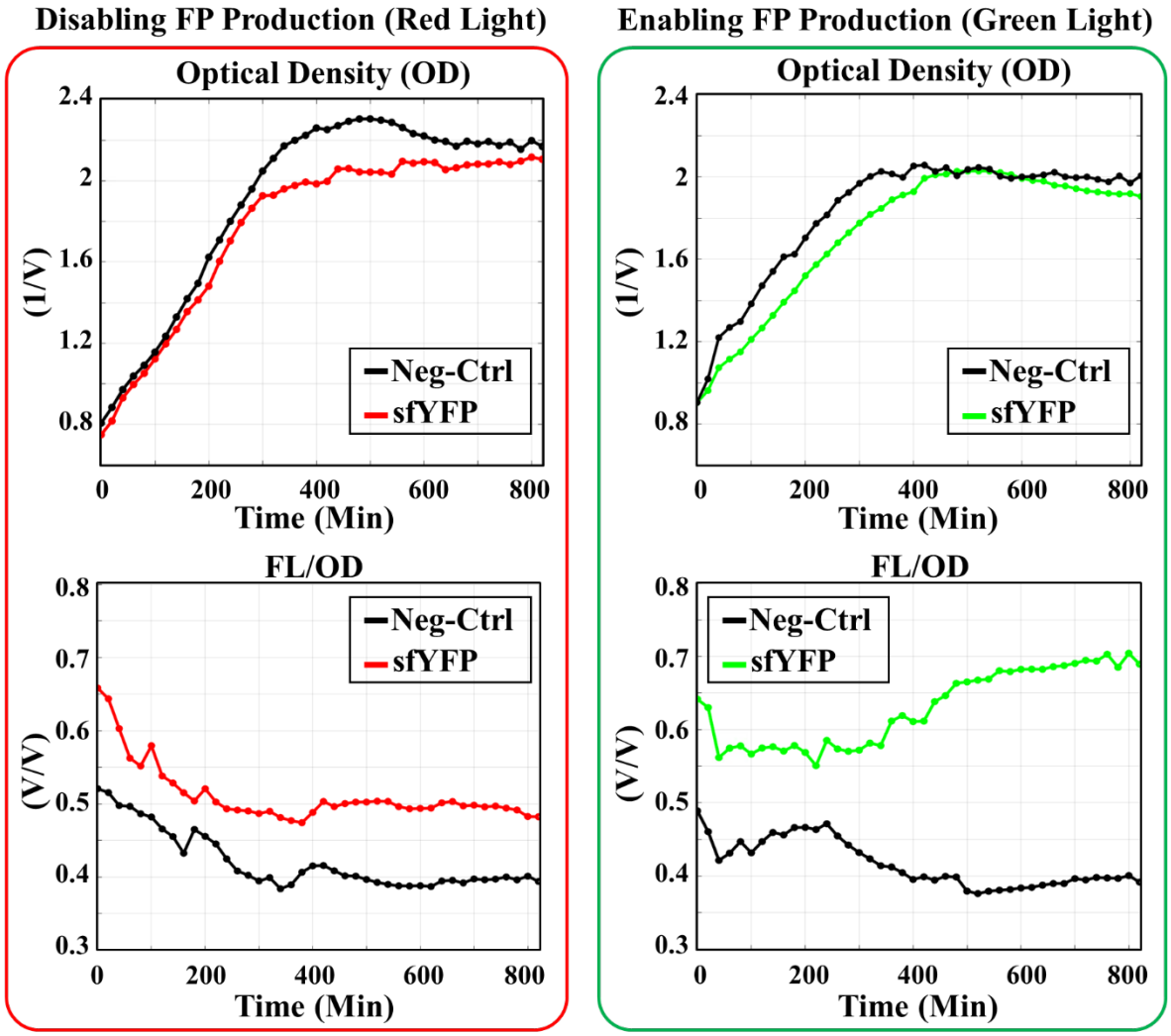

Figure 5.13: Measured results of OD and normalized fluorescence/OD expression when bacterial cells receive red/green lights.

This accomplishment demonstrates a potential to create an integrative autonomous sensing and payload delivery bioelectronic system. For instance, *in vivo* targeted drug delivery can be achieved by sensing a biochemical indicating inflammation in the gut. In response, appropriate optical signaling can activate medication production and delivery to treat the detected inflammation. Hence, this Silicon-Cell system can create a promising platform for developing novel therapeutic approaches.

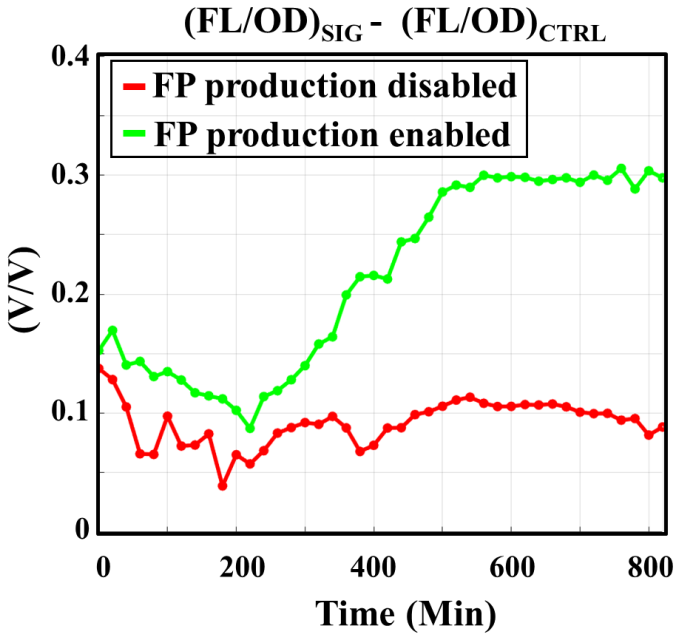

Figure 5.14: Measured results showing the feasibility of bidirectional communication with the cells by modulating their fluorescent protein production using optogenetic control.

In summary, this chapter presented the measured results of the integrated fluorescence sensor in the standard CMOS process. Table I shows the performance of this sensor in comparison with the prior art. Our work is the first fully integrated fluorescence sensor to use bacterial cells as biosensors and dynamically communicate with them. This is achieved by implementing optical filters in the suitable wavelength range to work with fluorescent proteins.

Table 5.1: Performance summary and comparison with the state of the art

Metric	[9] JSSC'2017	[50] JSSC'2022	[91] TBioCAS'2020	This Work
Technology	65nm	65nm	180nm	**65nm**
Detector Type	Fluorescence	Bioluminescence	Fluorescence	**Fluorescence**
Optical Filter (CMOS)	Yes (High-pass)	No	No	**Yes (Band-pass)**
Reporter Type	Qdot800 tags	Luminescence protein in bacterial cells	Qdot705 tags	**Fluorescent proteins in bacterial cells**
Measurement Type	Static	Static/Dynamic	Static	**Static / Dynamic (OD and FL signals)**
Excitation Source	405nm laser	N.A.	Laser (Blue)	**SMD LED**
PD Active Area	91.4 x 123 μm^2	1.24 x 1.24 mm^2	55 x 55 μm^2	**100 x 100 μm^2**
PD/Pixel Responsivity	22 mA/W (PD at 780nm)	N.R.	90.2 mA/W (1) (Pixel)	**24 mA/W (PD at 700nm)**
Power	66mW(2)	16.3µW(3)	3.5mW(4)	**Single Row:7.05mW(5) Three Rows:19.1mW(6)**
Output Noise(7)	1.31mV_{rms}	N.R.	4.5mV_{rms}	**3.846mV_{rms}**
Sensor Sensitivity	0.33fA	59fA	N.R.	**1.05fA**
Integration Time	1-10s	25.8s	10-50ms	**1s**
SNR	>20dB	N.R.	15.5dB	**18.3dB**

(1) Converted from reported pixel responsivity of 8.2V/pW.s, using Cfb=11fF and Tin=50ms.
(2) Reported for dual sensors.
(3) Capsule power for 2x2 array.
(4) Reported for 80 x 36 pixels array.
(5) Includes 1x (C-TIA + 4 buffers + 1/3 of a shared CDS) for 4 pixels.
(6) Includes 3x (C-TIA + 4 buffers) + 1x CDS for 12 pixels.
(7) Under dark condition.
N.A. – Not applicable, N.R. – Not reported.

Chapter 6

A FULLY INTEGRATED ADAPTIVE RECEIVER FOR RF OVER FREE SPACE OPTICS COMMUNICATION

6.1 Introduction

The ever-increasing demand for higher data rate communication has drawn significant attention to transmitting high-speed RF signals over optics. Using an optical carrier to transmit data has the advantage of accessing a very wideband channel since the strict regulation of the RF spectrum does not apply to the optical frequencies (Figure 6.1). Furthermore, the optical link has superior link security compared to the RF links since the optical beam is immune to electromagnetic interferences [91].

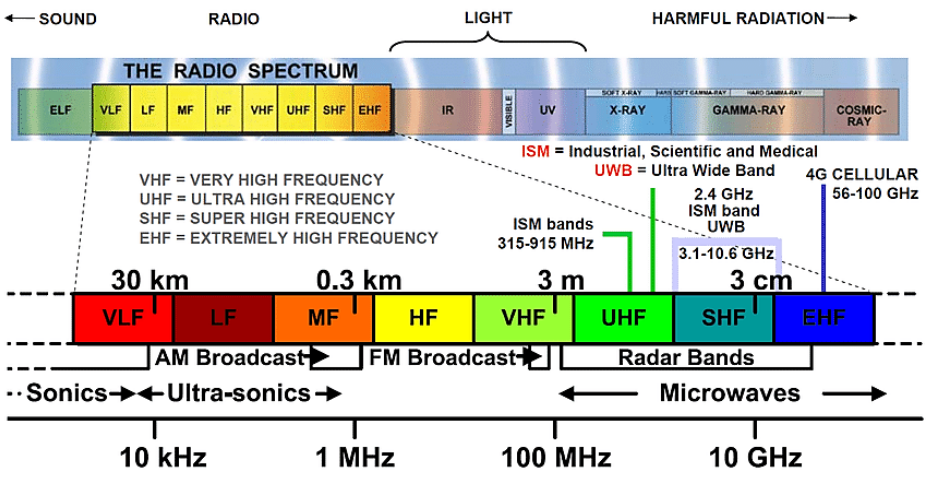

Figure 6.1: Strict regulation of spectrum for RF channels.

There are three main approaches to using optics as the communication medium. Based on the specific application and equipment availability, we can use RF over fiber (RoF), RF over free space optics (RoFSO), and Hybrid RF/Optics systems. With recent advances in digital signal processing (DSP), phase-modulated RoF links with coherent receivers have shown promising results [92]. However, in dense urban areas and remotely located settlements where the installation of optical fiber infrastructure is costly and time-consuming, RoFSO

has shown to be a superior candidate. Other applications of RoFSO include last-mile access and fiber backup plans. Specifically, for space-to-ground, ground-to-space, and inter-satellite links, RoFSO is the preferred choice with its high security, directivity (no multipath fading), and abundance of unregulated bandwidth (Figure 6.2).

Most of the published works on the RF over optics systems report experimental setups using off-the-shelf components to demonstrate the feasibility of the link [92,93,94]. Using intensity/ phase modulation and polarization multiplexing, [92] shows transmission of 4×2.5Gbps RF signals over 10km fiber. A coherent receiver and DSP are employed to eliminate the phase noise of the local laser, resulting in a BER of 10^{-3} for a minimum received power of -18dBm. A combined RoF and RoFSO system is presented in [93] to transmit the 64-QAM LTE-A signal with 100MHz of RF bandwidth, showing acceptable results with around 12dB FSO loss. Another work describes a millimeter-wave (mmW) and FSO hybrid system for transmitting a 4Gbps 16QAM signal [94]. Improved performance is reported for the hybrid link as FSO and mmW links exhibit complementary transmission characteristics under various weather conditions.

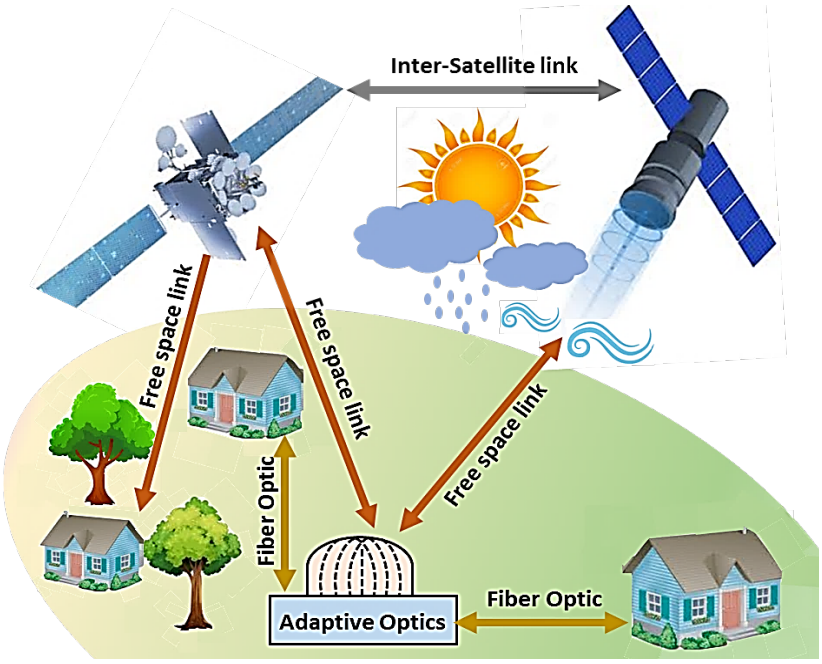

Figure 6.2: Free space optical communication applications.

This work implements a fully integrated and high-bandwidth receiver for RoFSO in a 28nm CMOS process. The adaptive receiver features multiple controlling loops to provide a wide dynamic range and enable the receiver to withstand significant variations of both average and peak optical power. This is required when the FSO receiver has a small aperture to save cost and area. We start the chapter by introducing FSO communication and the challenges of using the atmospheric channel as the medium. The design considerations and the proposed adaptive system is presented next. The detailed circuit design and simulation results will follow, and at the end, we will show the measurement results of the fabricated chip in 28nm CMOS.

6.2 Atmospheric Channel

Using free space as the communication channel for optical signals has several challenges that need to be studied and addressed for a practical FSO link design. This work focuses on designing an integrated adaptive receiver for the space-to-ground link, the most challenging FSO communication application. The challenges arise because, in this link, the optical beam reaches the earth's atmosphere when weakened after traveling a long distance from the originating satellite [95]. Hence, it is more susceptible to the distortions imposed by the atmospheric layers (Figure 6.3).

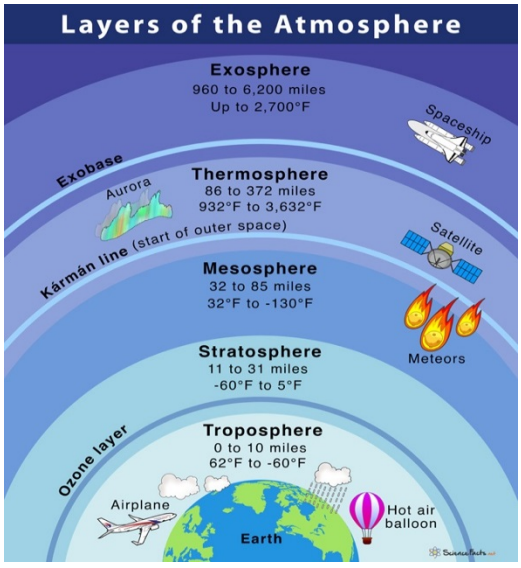

Figure 6.3: Several layers of the atmosphere.

The atmospheric channel causes severe distortions in the optical beam phase and intensity mainly due to turbulence effects and scintillation. Turbulence happens when the traveling beam faces air packets with random refractive indexes caused by non-homogeneities in the temperature and air pressure of the atmospheric layers [95]. These encounters cause random time-varying fluctuations in the wave front speed [96]. Hence, turbulence severely reduces the spatial and temporal coherence of the signal beam, leading to distortion in both the intensity and phase of the received beam [97]. As a result, the link error probability is affected, limiting the performance of the communication system and even causing a complete link blackout. As shown in Figure 6.4, the incoming beam wave front, after traveling through the atmosphere channel, is distorted so that it is no longer a plane when it reaches the receiver [98].

To reduce the beam aberration caused by turbulence, space-to-ground links need to employ adaptive optics (AO). As shown in Figure 6.5, this technology uses deforming mirrors in a closed-loop system to compensate for the wave front distortion [99].

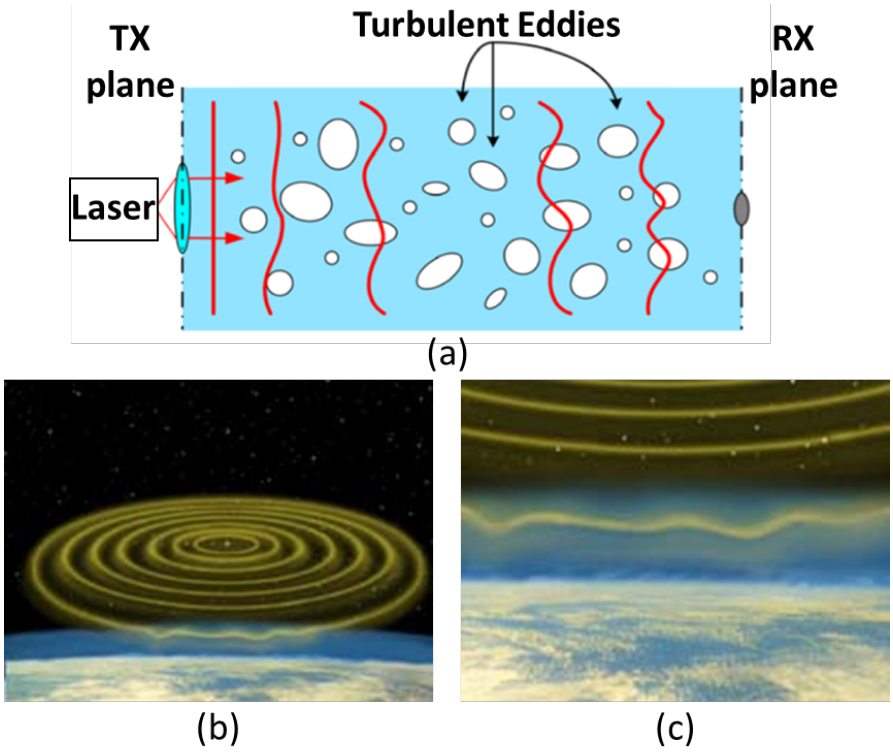

Figure 6.4: Distortion of the wave front by turbulent eddies in the atmosphere.

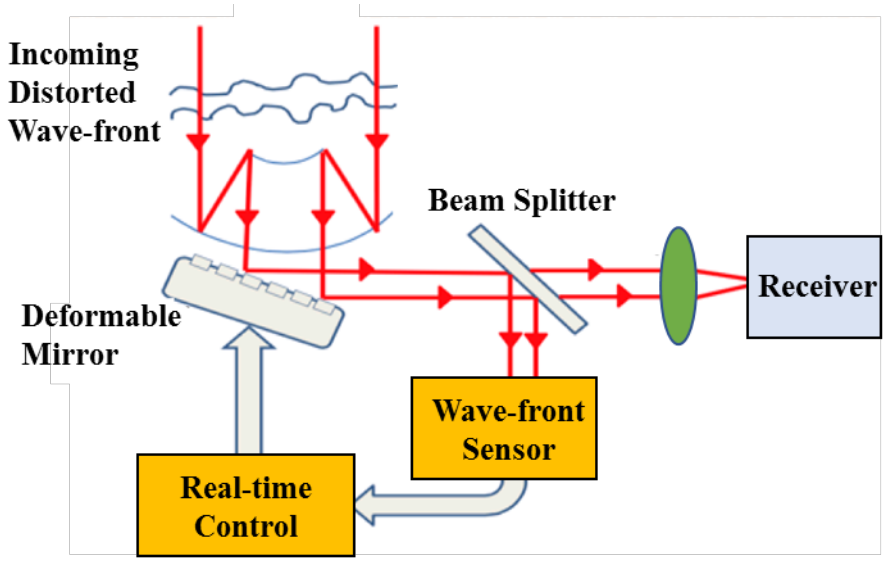

Figure 6.5: Adaptive optics block diagram.

Scintillation is the other significant challenge in the atmospheric channel. It refers to the attenuation and variation of the optical beam intensity primarily due to light scattering by air particles such as rain, snow, fog, and pollution [100]. As shown in Figure 6.7, the level of beam intensity attenuation can vary drastically based on the weather and pollution conditions of the day ranging from 0.06 dB/km to more than 12 dB/km.

The conventional remedy to compensate for scintillation effects is using the aperture averaging (AA) technique (Figure 6.8). By employing a considerable aperture size for the receiver at the ground station, the intensity fluctuation is reduced by averaging out the uncorrelated fluctuations at the receiver lens [101]. This is achieved at the expense of higher cost, larger space, and more background noise.

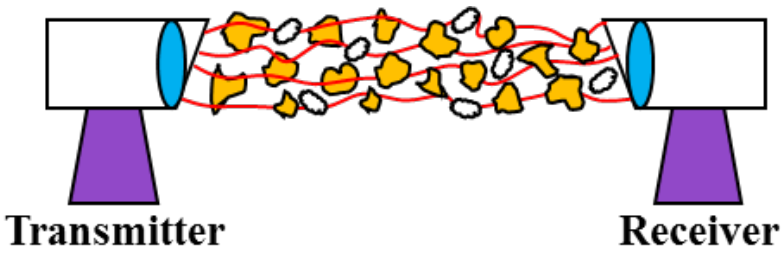

Figure 6.6: Variation in the wave intensity due to scintillation.

Figure 6.7: Difference in the visibility and optical wave intensity attenuation due to various weather conditions.

The other popular method for reducing the effect of scintillation is using the diversity technique in time, frequency, or space domains [102]. An array of small receiver apertures is employed to receive multiple copies of the mutually uncorrelated signals combined in the electrical domain, as shown in Figure 6.9. This method is also costly and bulky since the antenna separations must be greater than the optical wave coherence length (r_0) to ensure receiving uncorrelated copies of the signals.

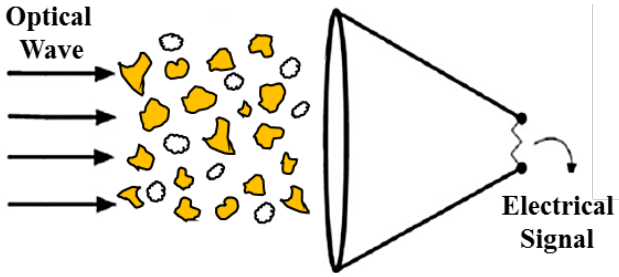

Figure 6.8: Concept of aperture averaging to reduce scintillation.

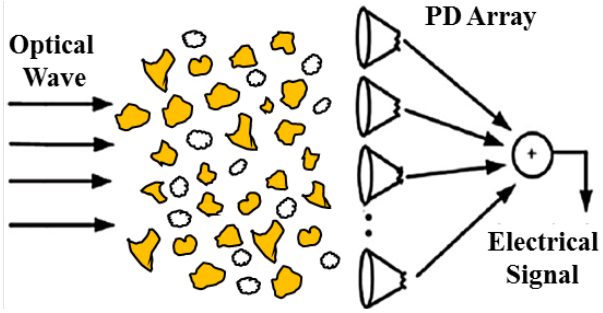

Figure 6.9: Concept of using diversity to reduce scintillation.

After studying the most critical challenges of free space optics and the conventional remedies to mitigate them, we aim to design an efficient adaptive receiver regarding cost and space. To start the design, with the help of the Jet Propulsion Laboratory (JPL) researchers, we analyzed the effect of turbulence and scintillation on the optical beam. Figure 6.10 shows the simulated scintillation effect from two aperture sizes with less intensity variation for the 1m diameter aperture due to aperture averaging. This distortion can be modeled as a slow, random multiplicative term with a coherence time in the msec range, which can be written in the following form:

$$P_r(u,t) = A(u,t).P_s(t) \tag{6.1}$$

in which P_r is the received optical signal, A(u,t) is the multiplicative stationary random process due to the scintillation, and P_s is the received beam in the ideal channel, i.e., A(u,t)=1. The frequency content of the scintillation shows the turning point ω_u around 2 Hz, which depends on the factors such as the amount of spatial averaging, aperture diameter, and wind velocity (Figure 6.11).

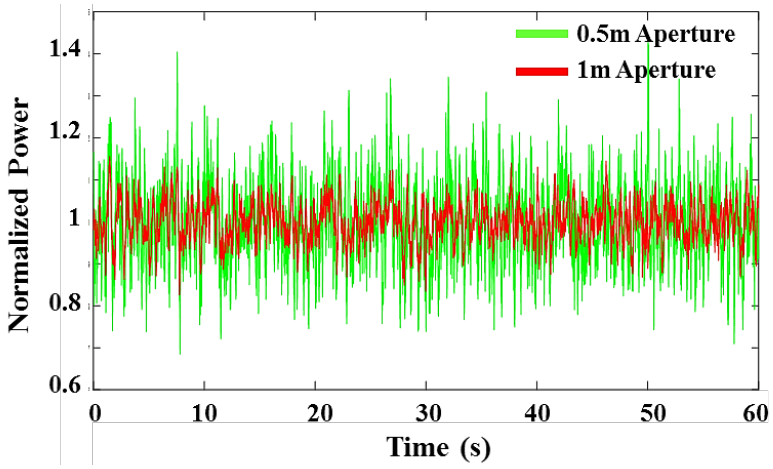

Figure 6.10: Transient simulation result of scintillation effect for two aperture sizes.

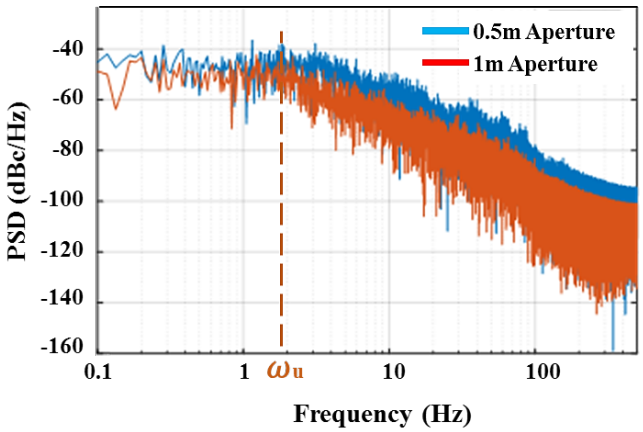

Figure 6.11: Spectrum of the scintillation effect for two aperture sizes.

6.3 System Level Design

The first step in designing the optical link is choosing the appropriate wavelength for the optical carrier. In addition to the scattering and absorption of the optical waves due to random and varying air particles, there are highly frequency-dependent molecular absorption lines mainly caused by water vapor and carbon dioxide [103]. As shown in Figure 6.12, in the broad spectrum of the practical optical band (1528-675nm), several molecular absorption lines can severely affect the transmission inside the atmospheric windows ranging from complete blockage to selective spectral sectioning of the signal's spectrum. Therefore, choosing the suitable wavelength for the FSO link is essential in ensuring the high quality of the link. 1550nm wavelength is the most common choice for free space optical communication due to the availability of high-power laser sources at this wavelength.

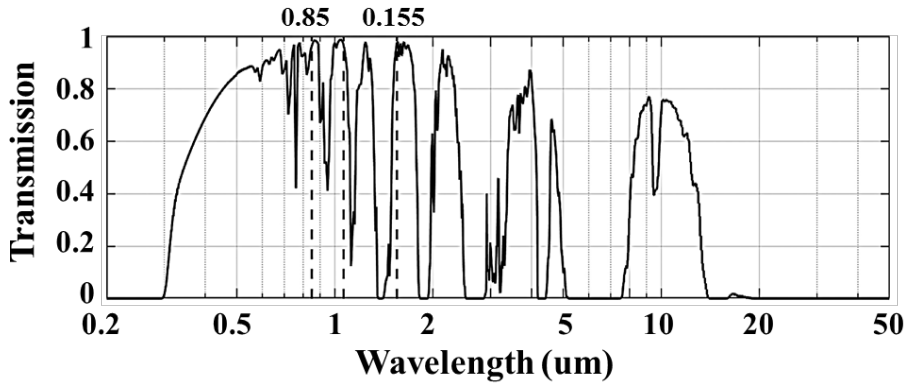

Figure 6.12: Spectral transmissivity of earth's atmosphere from sea level to space in zenith.

6.3.1 Modulation

The next step in designing the communication link is deciding the suitable modulation type. Like RF waves, the optical beam's intensity, phase, or frequency can be modulated to transmit the baseband or RF data. The type of channel, here the atmosphere, dramatically impacts this choice since, as previously discussed, atmospheric effects distort the quality of the beam's intensity and phase.

Intensity modulation/direct detection (IM/DD) is the most common modulation type for high-speed baseband optical communications due to its straightforward design, especially on the receiver side. The direct detection receiver includes a photodetector, trans-impedance amplifier (TIA), and heavy DSP to recover the digital data. However, in free space links with high-intensity variation, the performance of this link can be severely limited.

Using the phase of the optical beam (in addition to its intensity) can significantly increase the data throughput. Very high data rate systems using this modulation type and optical fibers have been reported [104,105,106]. On the receiver side, these systems must employ coherent detection to recover the signal from the beam phase. Besides being complex in the optical and DSP domain due to the optical carrier recovery and phase estimation, the main requirement of this modulation is having a perfectly coherent optical beam as a carrier. Since atmospheric turbulence significantly reduces the coherency of the beam, using phase modulation for FSO is not applicable.

Subcarrier intensity modulation (SIM) is a promising method in which a phase-modulated RF carrier modulates the intensity of the optical beam, resulting in both average and peak optical power being constant. These characteristics benefit a high scintillation channel since the information in the beam's intensity would be lost. Furthermore, with this modulation, there is no need for perfect phase alignment and coherency for the received optical beam. The choice of modulation type at the subcarrier level requires a trade-off between complexity, power, and bandwidth efficiencies. Differential PSK (DPSK) is selected in this work to avoid complex DSP for absolute RF phase estimation at the expense of a 3dB CNR

(carrier-to-noise ratio) penalty. Non-coherent demodulation of DPSK is done by comparing the phase of the received signal in any signaling interval with the preceding one. This is feasible in the turbulence condition since, atmospheric channel coherence time (~msec) is significantly longer than the typical duration of two consecutive data bits in the Gbps range.

The block diagram of the proposed system employing SIM is shown in Figure 6.13. At the transmitter side, a high-power laser generates an optical beam at 1550nm with P_0 average power. Then using an optical modulator, the intensity of the optical beam is modulated by signal m(t), an RF signal whose phase is used to transmit the baseband information x(t).

$$P_{out}(t) = P_0\{1 + \beta.m(t)\} \tag{6.2}$$

$$m(t) = Cos[\omega_{RF}t + \varphi(x(t))] \tag{6.3}$$

in which β is the intensity modulation depth, which, as we will discuss shortly, greatly impacts the system's CNR. Since the optical modulator needs an amplified RF signal to operate, a modulator driver block is required, which is a high-power RF amplifier. The generated optical signal P_{out} propagates in the atmospheric channel and reaches the receiver while distorted by A(u,t).

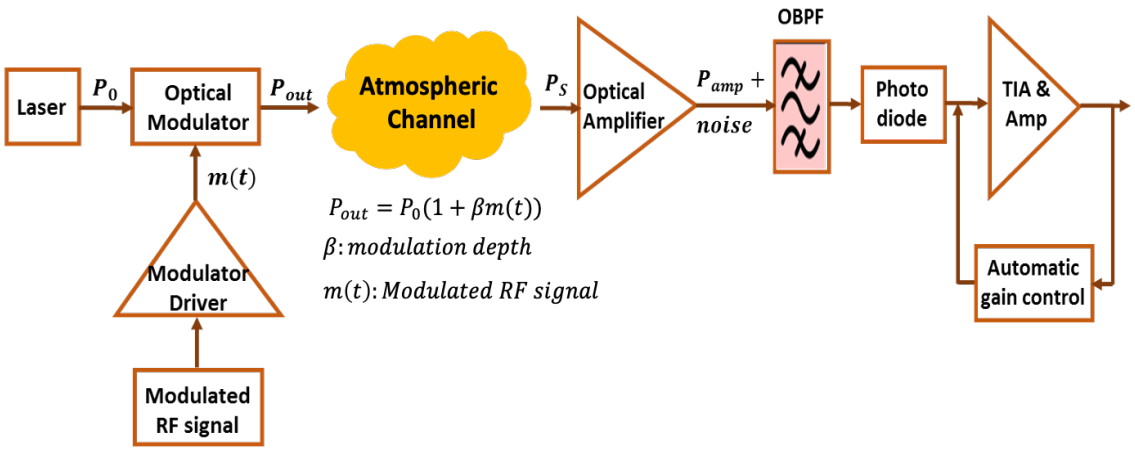

Figure 6.13: System-level block diagram of the proposed FSO link.

$$P_s(u,t) = A(u,t).P_{out}(t) \quad (6.4)$$

At the receiver side, due to the weak received optical intensity, the beam needs to be pre-amplified with an optical amplifier. A narrowband optical filter then filters the amplified signal to reduce the bandwidth of the integrated noise. Then, a high-speed photodiode converts the optical signal to an electrical current that enters the receiver circuitry. In the simplest form, the receiver includes a TIA to convert the current to voltage and recover the baseband data. In FSO communication, the receiver should be able to adapt to the varying channel conditions regarding signal intensity. Hence, an automatic gain control (AGC) loop is required to keep the receiver in the desired working condition.

Moreover, the receiver should be as wideband as possible to take advantage of the high bandwidth available for optical signals. The cost of having a wideband system is more noise as it gets integrated over a broader bandwidth range. Therefore, it is crucial to identify the most important noise sources in the design and optimize their behavior.

6.3.2 Noise Analysis

The proposed system with the relevant noise parameters for each block is shown in Figure 6.14. After being amplified in the optical amplifier (EDFA) with gain G and noise factor F_n, the optical beam is filtered to limit the optical bandwidth to a narrow range BW_{op}, reducing background noise. A PIN photodiode (PD) with responsivity R is employed to convert the optical signal to the electrical current, which is then processed by the variable gain TIA block. Defining the CNR at the input of TIA, equation (6.5) shows the ratio of the photocurrent power to the sum of the various integrated noise components. The shot noise of the PD, RIN noise of the laser, input-referred thermal noise of the CMOS chip, and amplified spontaneous emission (ASE) noise of the EDFA are the most important noise sources of the system [107]. As defined in (6.6), ASE noise has two components: Signal-ASE noise (dominant term) and ASE-ASE beat noise.

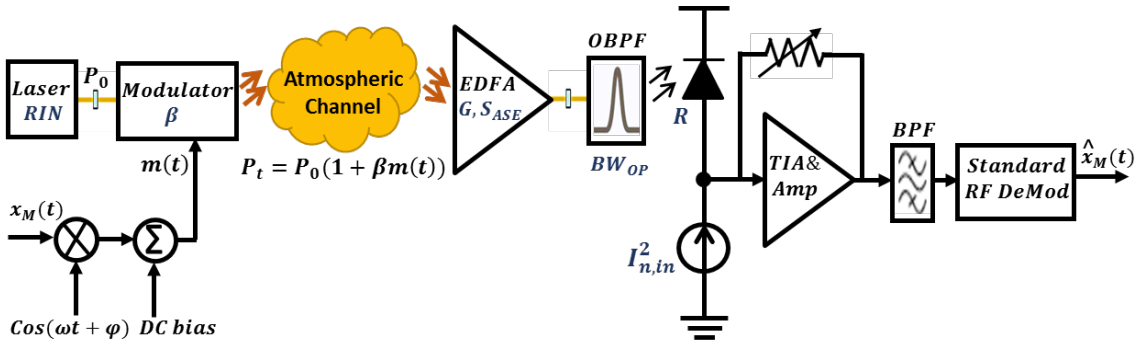

Figure 6.14: Noise parameters of the proposed FSO system.

$$CNR = \frac{½\,(G\beta R P_0)^2}{\left[2qRGP_0 + RIN(R\,G\,P_0)^2 + I^2_{n,in} + I^2_{n,ASE}\right]BW_{RF}} \tag{6.5}$$

$$I^2_{n,ASE} = R^2\left(2GP_0S_{ASE} + S^2_{ASE}BW_{op}\right) \tag{6.6}$$

in which S_{ASE} is the spectral power density defined as:

$$S_{ASE} = (G-1)\left(\frac{hc}{\lambda}\right)F_n \tag{6.7}$$

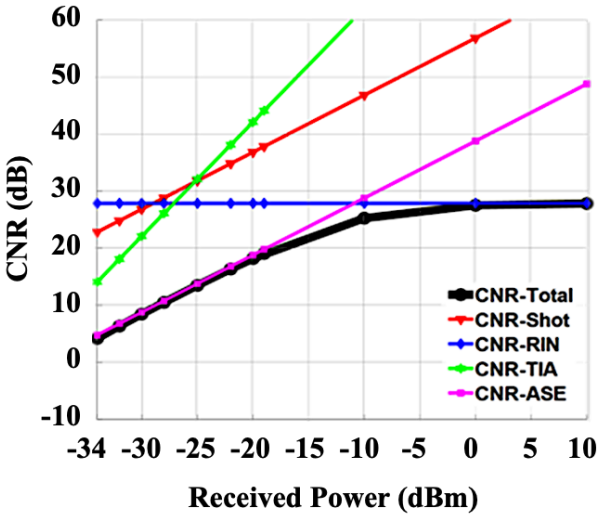

Parameters	Value
BW_{RF}	10 GHz
β	0.33
F_n	5 dB
λ	1550 nm
BW_{op}	0.1 nm
Laser RIN	-140 dBc/Hz

Figure 6.15: Partial CNRs due to various noise components and critical system parameters.

To evaluate the effect of each noise source independently, partial CNRs due to each noise component are plotted in Figure 6.15. Based on the main parameters of the system listed in Table I, it is shown that for low received optical power, the most dominant noise of the system is ASE noise, resulting in quantum-limited CNR_{QL}, as defined in (6.8).

$$CNR_{QL} = \frac{\frac{1}{4}\beta^2 P_0}{F_n\left(\frac{hc}{\lambda}\right) BW_{RF}\left(1 + F_n\left(\frac{hc}{\lambda}\right)\frac{BW_{op}}{2P_0}\right)} \tag{6.8}$$

Equation (6.8) shows that a large intensity modulation depth (β) greatly impacts achieving high CNR. To know the limitations of a large β, we should study the behavior of the optical modulator on the transmitter side.

The most common optical intensity modulator is the Mach-Zehnder modulator (MZM), an interferometric structure made from a material with a solid electro-optic effect (such as LiNbO3, GaAs, InP). Applying electric fields to the arms changes optical path lengths resulting in phase modulation. Combining two arms with different phase modulation converts phase modulation into intensity modulation [108] (Figure 6.16). The transfer function of the MZM (Figure 6.17) is cosine-like with heavily non-linear areas close to the nV_π points. To achieve the maximum linear range for the beam intensity modulation, the optimum bias point for the MZM is $V_\pi/2$, which gives us a span of less than V_π, limiting the modulation depth β to avoid strong non-linearity terms [109].

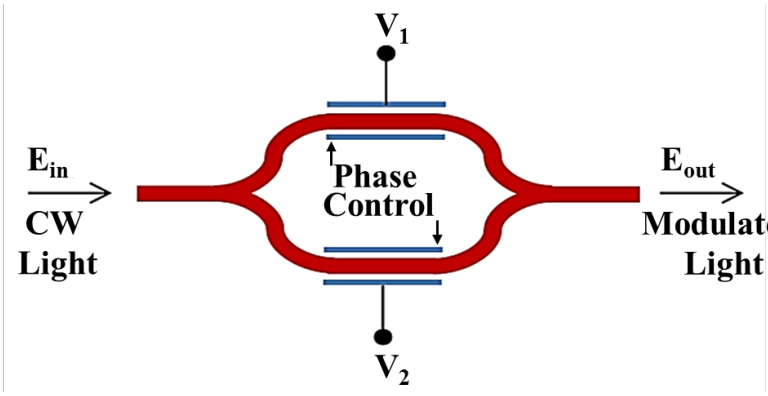

Figure 6.16: Working principle of the MZM modulator.

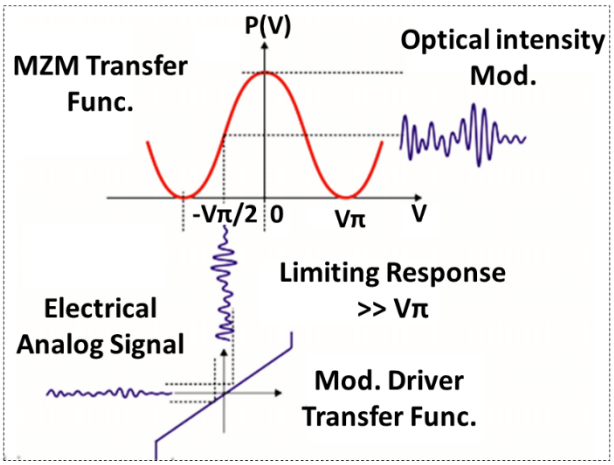

Figure 6.17: Analog modulation of the optical intensity and MZM transfer function.

Since the dominating noise source of the receiver is the optical amplifier, we will briefly discuss their behavior here. Erbium-Doped Fiber Amplifier (EDFA), which is the most common optical amplifier, is used in this work. The gain of these amplifiers is in the range of 10-30dB, which ideally should not change with the input power level. However, as shown in Figure 6.18, this is not the case in the optical amplifiers operating near the maximum output power. Hence, the amplifier must respond slowly enough so that its gain is determined by the average input power and not affected by fast changes imposed on the signal (for instance, due to data modulation) [110].

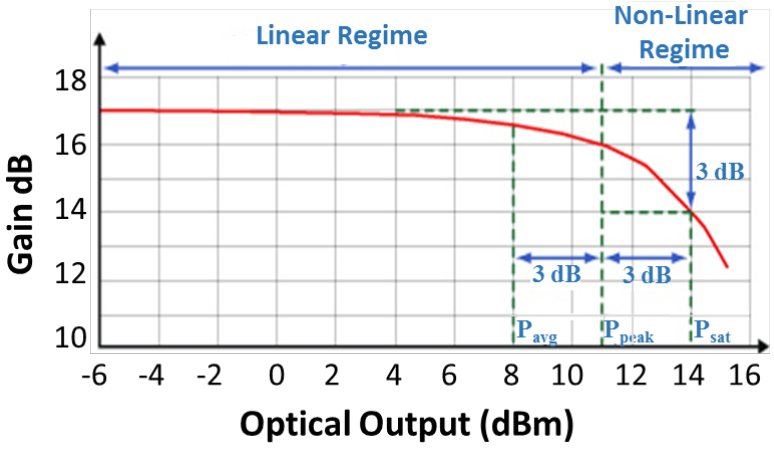

Figure 6.18: Typical transfer function of the optical amplifier.

6.3.3 Subcarrier Diversity

Diversity techniques are widely used in the RF domain to increase data throughput. In an FSO system with SIM modulation, applying channelization and diversity in the subcarrier domain to either increase the throughput or decrease the BER is efficient as it can be achieved using one optical front end and multiple RF subcarriers. For instance, time delay diversity (TDD), in which different subcarriers transmit delayed copies of the original data, can be used to avoid error bursts during deep fades (Figure 6.19).

By ensuring $\tau > \tau_0$, in which τ_0 is the coherence time of the channel, uncorrelated time copies of the data are received, which can be used in processing circuitry to recover data with lower BER. Additionally, SIM FSO can easily interface with analog/digital systems and employ any desired modulation schemes in the RF domain.

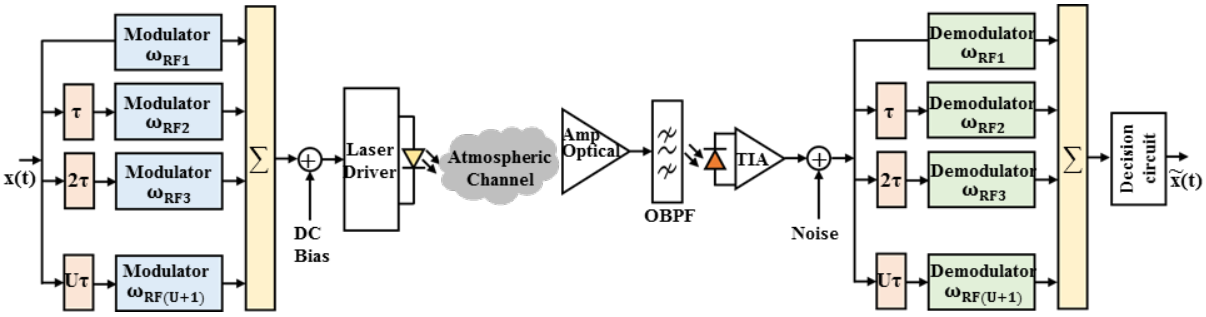

Figure 6.19: Applying a time delay diversity in the FSO SIM system.

6.3.4 Block Diagram Design

The block diagram of the adaptive FSO receiver is shown in Figure 6.20. Multiple adaptive loops are designed to compensate for significant variations in the beam intensity and ensure the receiver's wide dynamic range while avoiding significant non-linearity terms. For the received power of P_s, distorted by atmospheric channel $A(t)$, the received power P_r after amplification by EDFA is as below:

$$P_r(t) = G.P_s(t) + n_1(t) = G[A(t).P_{out}(t)] + n_1(t) \quad (6.9)$$

in which $n_1(t)$ is primarily the noise of the optical amplifier. A photodiode with responsivity R then converts the amplified and filtered optical signal to an electrical current I(t) and adds the noise of the electrical receiver ($n_2(t)$):

$$I(t) = R.P_r(t) + n_2(t) \tag{6.10}$$

Substituting the values of $P_r(t)$ and $P_{out}(t)$ from equations (6.1) and (6.2), results in:

$$I(t) = K_1.A(t).m(t) + K_2.A(t) + N(t) \tag{6.11}$$

In which $K_1 = R.G.P_0.\beta$, $K_2 = R.G.P_0$, and $N(t) = R.n_1(t) + n_2(t)$. Writing the electrical input current in the frequency domain shows the electrical signal has a low-frequency part mainly due to scintillation and a high-frequency part around the RF carrier frequency.

$$I(f) = K_1.A(f) * M(f) + K_2.A(f) + N(f) \tag{6.12}$$

Hence, we can safely remove the low-frequency part of the input current to avoid the saturation of the early electrical stages in case of receiving large input average power.

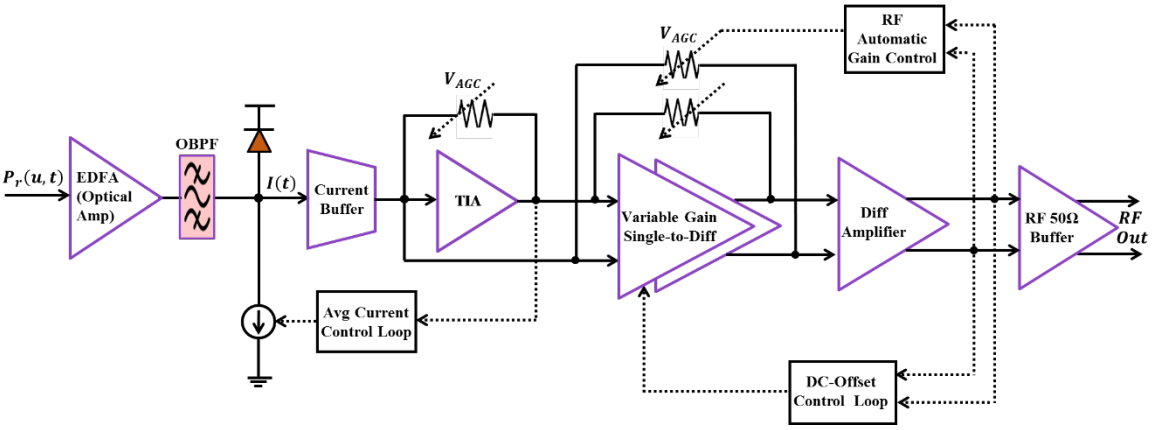

Figure 6.20: Block diagram of the proposed adaptive FSO receiver featuring several controlling loops to increase its dynamic range.

As shown in Figure 6.20, an average current control loop is designed to subtract the large DC current entering the buffer and hence keep the average of the signal at TIA output constant. The current signal is converted to voltage in a variable-gain TIA block, providing amplification and the required negative input for the single-ended to differential (STD) conversion in the next stage. The gain-controlling voltage is supplied by the automatic gain control (AGC) loop, which limits the high nonlinearity terms by keeping the output signal in a well-defined range. The differential block is used next for STD conversion and to provide additional variable gain while keeping the receiver wideband. The third loop is to achieve DC-offset cancellation and to keep the differential stages at their optimum bias points. Finally, a 50-ohm buffer is designed to interface the receiver with external measurement equipment.

6.4 Integrated Circuit Design

The circuit diagram of the first three blocks of the receiver, including the current buffer, variable-gain TIA, and the average current control loop, is shown in Figure 6.21. A commercial wideband PD converts the optical beam to the RF current. Being external, the PD should be wire bonded to the CMOS chip, and hence considering the electrical characteristics of the bonding wire is required. The compact model of the wire can be reduced to an inductance, $L_{wirebond}$, connected in series at the chip's input. The external PDs additionally suffer from large parasitic capacitance (C_{PD}) that can severely limit the receiver bandwidth. Hence, to avoid the input node being a dominant pole, the first electrical stage should provide a very low input impedance (Zin).

A current buffer with the regulated cascode (RGC) structure is designed as the first stage. Since the ASE noise of the EDFA dominates the noise of the system, the primary goal of the first electrical stage is to have minimum input impedance with the least power consumption. In the RGC circuit, the addition of an amplifier (M_3, R_3) in the feedforward path with a level-shift circuit (M_2, R_2) reduces the input impedance of the circuit ($1/gm_1$) by a factor of ($1 + gm_3R_3.gm_2R_2$) while leaving sufficient headroom at node V_x [111].

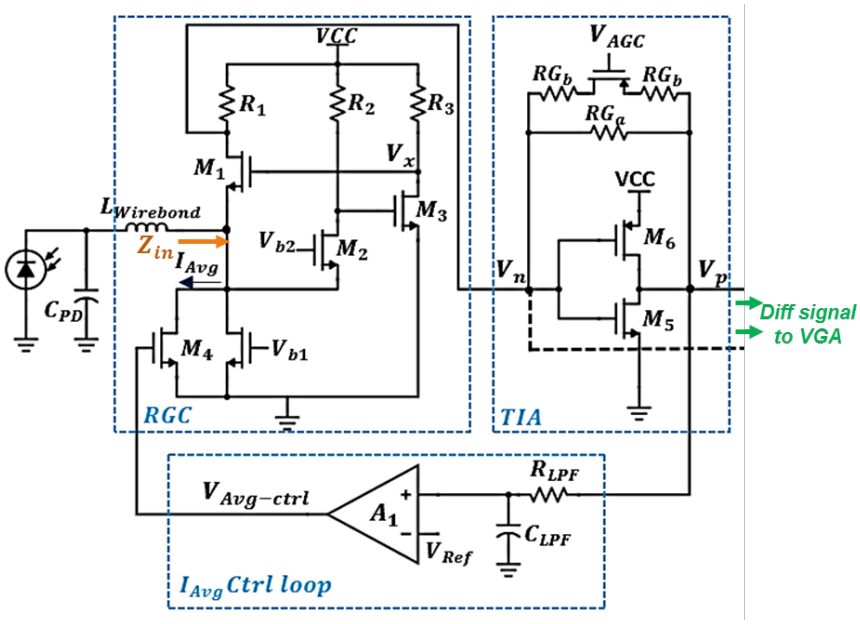

Figure 6.21: Detailed circuit diagram of the front end, including the current buffer (RGC), inverter-based variable gain TIA and automatic average current control loop.

The next stage is a trans-impedance (TIA) block to convert the current to voltage with a variable gain. Inverter-based TIA is a prevalent choice due to its simple and self-biased design. Its gain control is realized by a constant resistor in parallel with a PMOS and two series resistors. At high input signal level, the V_{AGC} is low, the PMOS is ON, and PMOS's ON resistance sets the gain. Since the nonlinearity of this transistor may appear for large input swings, the two resistors in series are used to improve the linearity of the combination. To take advantage of the differential design benefits in terms of linearity and common-mode noise rejection, it is desirable to convert the single-ended signal to differential (STD) early in the chain. The conventional method to create the negative input for STD conversion is using a replica TIA circuit. Due to added area, power, and noise to the system, this method is not desirable. An important benefit of the inverter-based TIA is the readily available negative input (V_{n}) without adding other blocks. As shown, the inverter input node can be used as the negative input for the STD conversion in the next stage [112].

In the case of large input photocurrent, the RGC gets saturated and causes signal distortion from the early stages. Hence, the average PD input current should be kept constant by

subtracting the excess incoming current from the RGC input node. The TIA (V_p) output voltage is an appropriate reference point for the average photocurrent control loop. Using a compact lowpass filter and the error amplifier A_1, $V_{Avg\text{-}ctrl}$ is generated to control the current of the voltage-controlled current source (M_4) in this loop.

Figure 6.22 shows the circuit diagram of the blocks that follow the TIA. To amplify the signal differentially while keeping the receiver wideband, a variable gain amplifier (VGA) based on the Cherry-Hopper (CH) circuit [113] is designed.

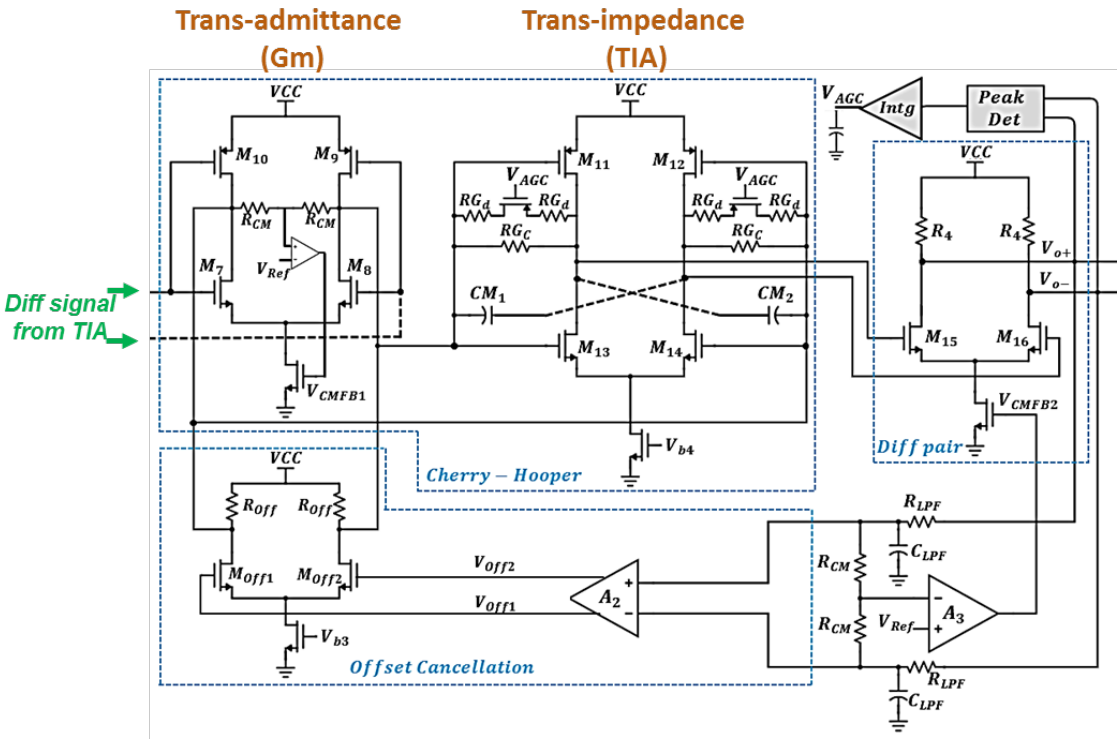

Figure 6.22: Detailed circuit diagram of the differential Cherry-Hooper amplifier, gain block, automatic gain control loop, and offset cancellation loop.

It comprises a differential trans-admittance (TAS) stage, which converts the TIA voltage to current, and a differential variable-gain trans-impedance stage for I-to-V conversion. The gain of the VGA is determined by gm of the TAS and variable RG_c of the trans-impedance. The two small negative Miller capacitances ($CM_{1,2}$) decrease the total capacitive load seen at the TAS output nodes, increasing the receiver's bandwidth with the minimum added area.

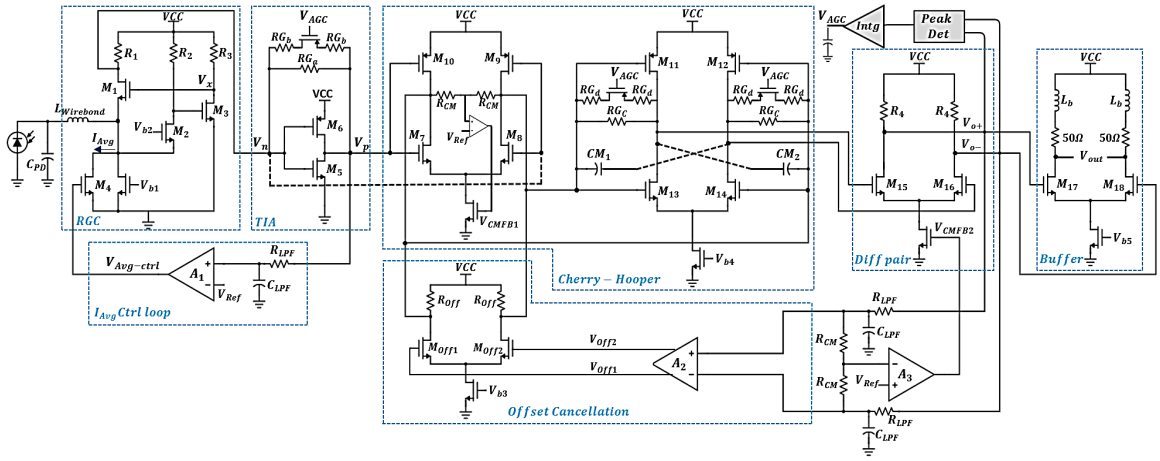

Figure 6.23: Detailed circuit diagram of the complete receiver.

Next, a differential gain stage is implemented, and its outputs ($V_{o+/-}$) are used for the peak detection circuit required for the automatic gain control (AGC) loop. The peak detector is a source-follower pair supplying the signal to the integrator block. Furthermore, the offset cancellation loop receives the average of $V_{o+/-}$ as the input and, after amplification by A_2, uses a differential GM stage ($M_{off1,2}$) to draw the corrective currents from the TAS circuit. Since the CH structure ensures low impedance at the TAS output nodes, additional loading by the offset cancellation circuit does not deteriorate the receiver's frequency response. Ultimately, a 50Ω buffer stage with inductive peaking is designed to interface the chip with the measurement equipment. Figure 6.23 shows the complete circuit diagram of the receiver at once.

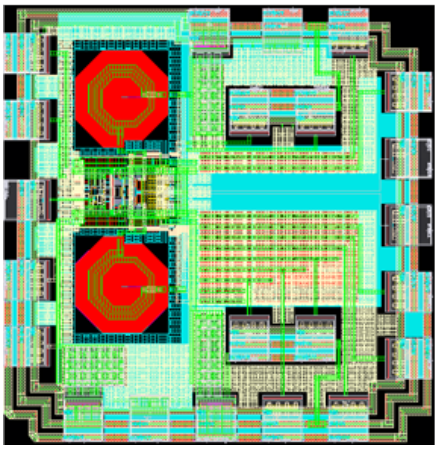

Figure 6.24: Layout of the FSO receiver in 28nm CMOS.

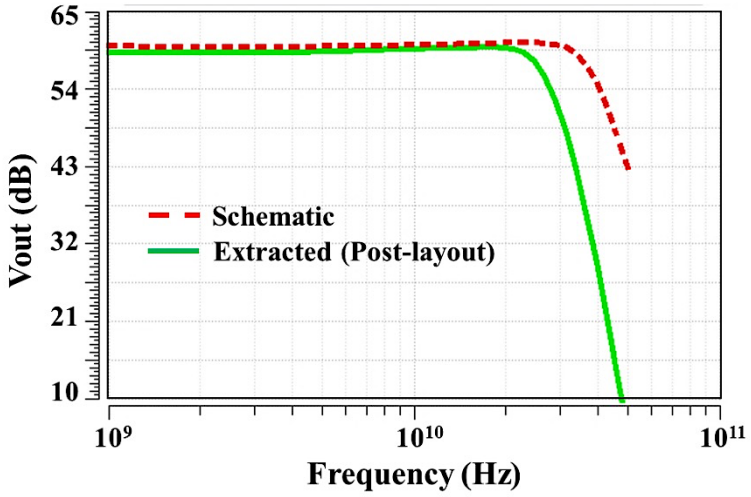

Figure 6.25: Simulated frequency response of the receiver in schematic and post-layout.

6.5 Simulation Results

The proposed adaptive receiver is designed in a 28nm CMOS process with a 1.2V supply voltage, and its layout is shown in Figure 6.24. The main parameters of the receiver are simulated at the schematic level and post-layout level after extracting the parasitic due to routing and circuit interconnects. In high-frequency circuits, the effect of parasitic capacitors in reducing the bandwidth is significant. As shown in the simulated frequency response plot in Figure 6.25, the 3dB bandwidth of around 38GHz in the schematic level reduces to 26GHz in post-layout simulation at the highest gain settings of the receiver.

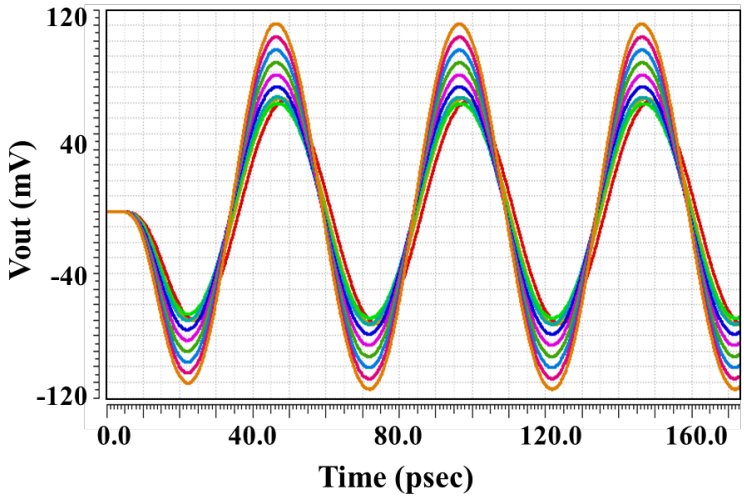

Figure 6.26: Simulated transient response of the receiver for an input range of 0.16-1.6mA.

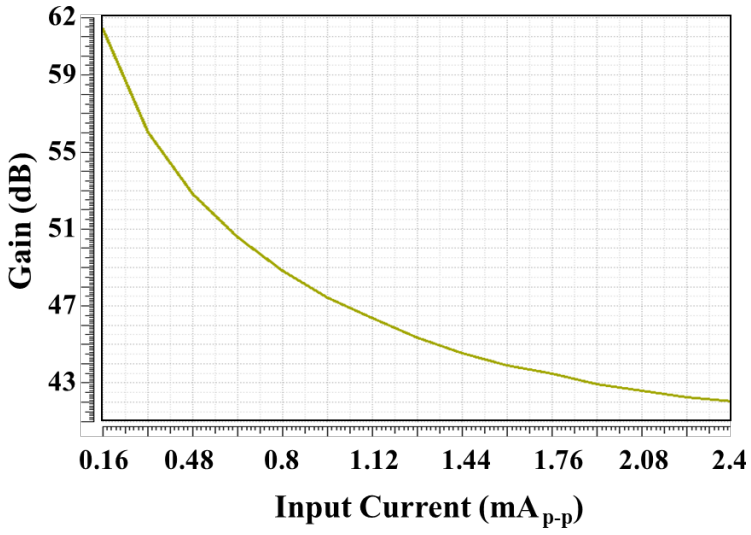

Figure 6.27: Variable gain of the receiver for an input range of 0.16-2.4mA.

The transient simulation of the receiver shows the differential output signal for an input range of 0.16mA-1.6mA (Figure 6.26). As seen, the output signal is not saturated or distorted and has low amplitude change due to the wide range of input current. This is achieved by employing an effective automatic gain-control loop that varies the system's gain up to 20dB to achieve a high dynamic range while minimizing the distortion (Figure 6.27).

The linearity of the receiver plays a significant role in preserving the quality of the signal, and it can be defined for both the amplitude and phase of the signal. There are multiple causes of nonlinearity in the FSO system, including the transmitter side (due to the optical modulator) and the receiver side (due to the optical amplifier and the receiver circuitry).

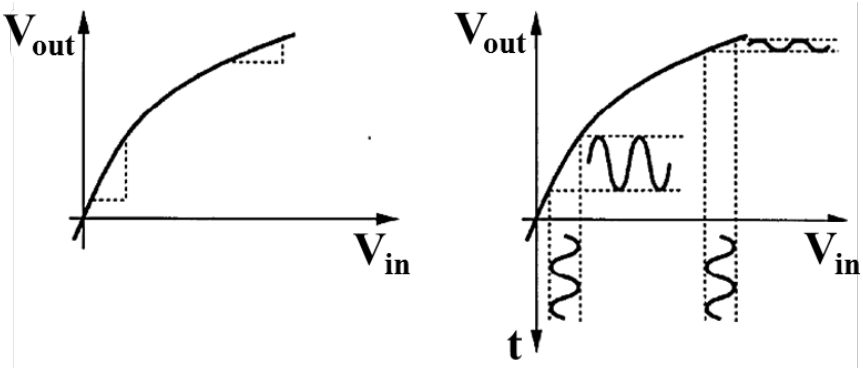

Figure 6.28: Concept of non-linearity in a circuit.

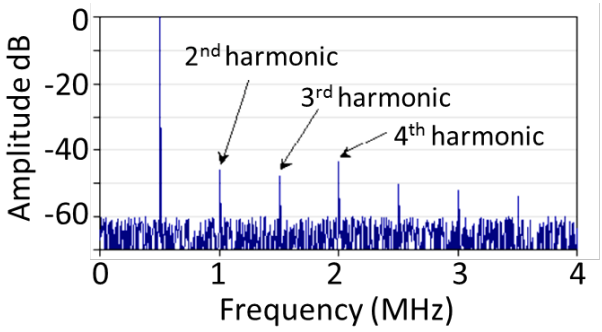

Figure 6.29: General spectrum of the signal passing through a non-linear system.

Therefore, it is essential to simulate and characterize the nonlinearity of the receiver. The input-output characteristic of the nonlinear system deviates from a straight line as the input swing increases. Hence, depending on the input DC level, the same input signal may result in different changes in the output, indicating variation in the small signal gain of the system. Moreover, significant signal distortion due to the saturation of the gain stages can happen, resulting in the output signal clipping. This amplitude nonlinearity of the system can be characterized by measuring the parameter named total harmonic distortion (THD), which is widely used to compare the linearity of different designs. THD is achieved by applying a sinusoid at the input and measuring the harmonic content of the output using the following equation.

$$THD = \frac{P_2 + P_3 + P_4 + \cdots}{P_1} = \frac{\sum_{n=2}^{\infty} P_n}{P_1} \tag{6.13}$$

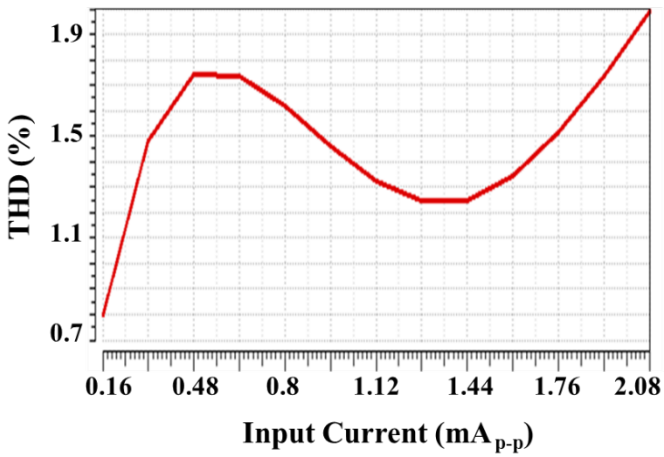

Figure 6.30: Simulated THD of the receiver for the input range of 0.16-2.08mA.

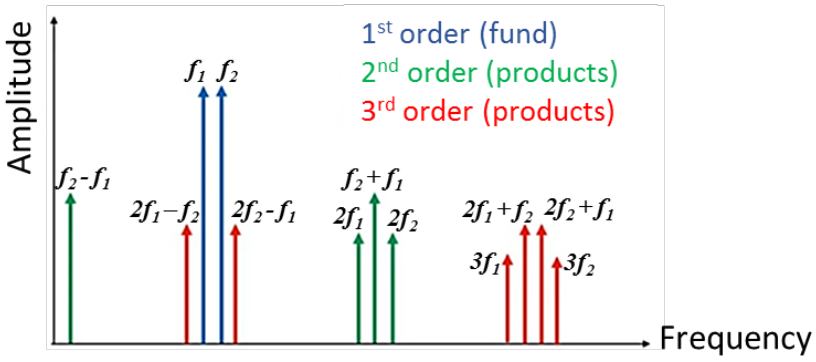

Figure 6.31: Definition of intermodulation distortion.

One of the differential design's benefits is improved linearity (free from even-order harmonics) while providing the same voltage gain and output swing. The plot in Figure 6.30 shows the simulated THD of the receiver in a wide range of the input current from 0.16 mA_{PP} to 2.08 mA_{PP}, which is less than 2%.

In addition to the primary signal harmonics, wideband receivers are vulnerable to intermodulation distortion (IMD) terms which occur when two or more signals are present in a non-linear system. If the input to a nonlinear system includes two main tones at f_1 and f_2 frequencies, in addition to each tone harmonics, the nonlinear system creates other output signals at $mf_1 \pm nf_2$ which can be at the receiver bandwidth, reducing the signal-to-noise and distortion ratio. As seen from the simulation results in Figure 6.32, in response to a wide range of the input signal of 0.16-2.56mA_{p-p}, the system's intermodulation and second harmonic terms remain lower than -30dB and -25dB, compared to the fundamental tone.

In a system with a wideband phase-modulated RF signal, the receiver's phase linearity is also of concern. Group delay is a parameter that characterizes the phase nonlinearity of a system. By ensuring a constant group delay up to the maximum frequency component of the signal, all frequencies of interest in the system undergo equal time delay; hence ideally, there won't be any phase distortion in the band of interest. The simulated plot in Figure 6.33 shows the group delay variation in the range of 4-20GHz is limited to 7psec.

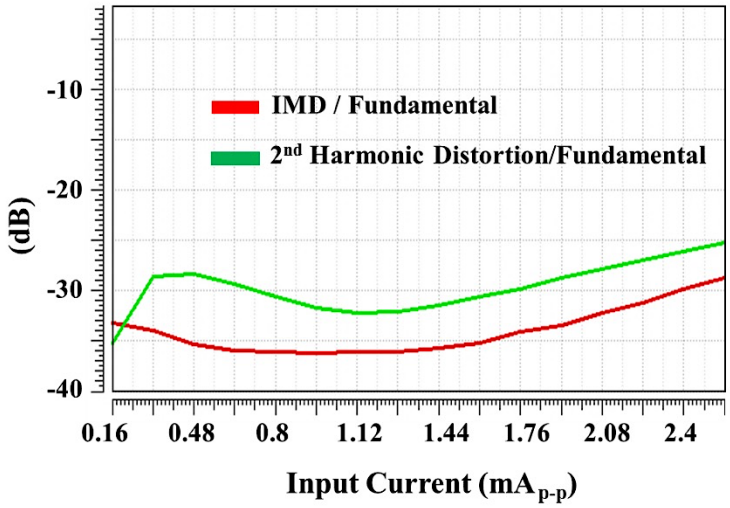

Figure 6.32: Simulated response of the receiver showing better than 30dB (25dB) rejection of IMD (2nd harmonic) vs. fundamental tone for the range of 0.16-2.4mA input current.

Finally, the receiver is simulated in response to a transient pulse in the input current, as shown in Figure 6.34. Even though the speed of the atmospheric channel is very slow (in the msec range), this simulation will show the system's stability in response to a step input. We see that the system is stable and well-behaved for the fast-changing current input with minimal shooting and ringing.

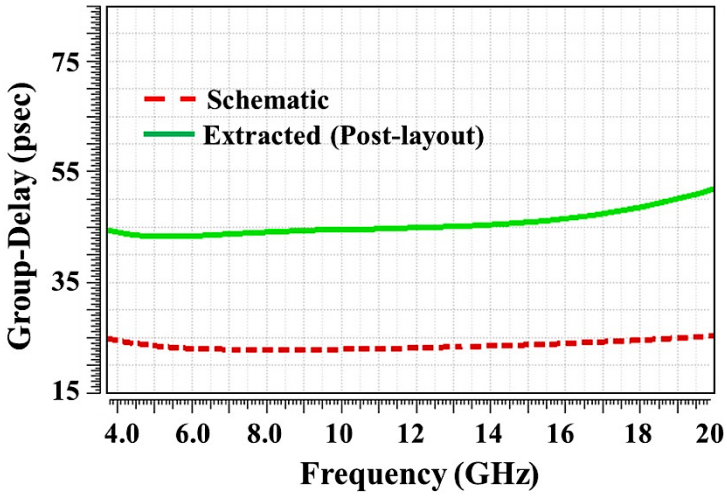

Figure 6.33: Simulated group delay of the receiver in schematic and post-layout.

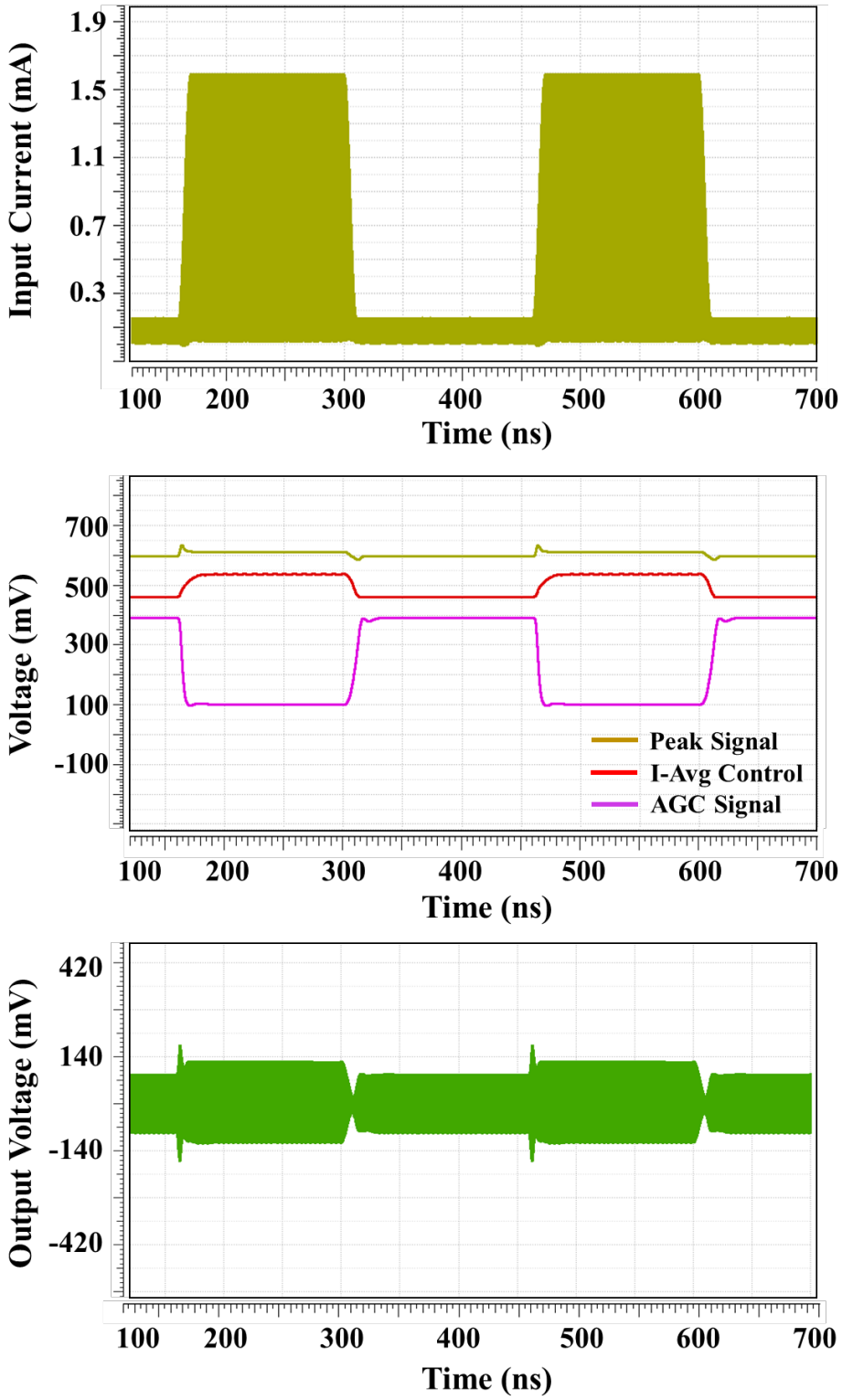

Figure 6.34: Step response simulation of the receiver showing stable and fast response to the sudden change in the input amplitude.

6.6 Measurement Results

The designed optical receiver is implemented in TSMC 28nm CMOS technology, and its chip micrograph is shown in Figure 6.35 (a). The area of the chip is 0.6×0.6 mm^2, as dictated by the pad count required for characterization purposes. The external PD as shown in Figure 6.35 (b) is a 16μm-detection-window InGaAs PIN chip with 0.7A/W responsivity. It has 80fF parasitic capacitance and is wire bonded to the input pad of the designed CMOS chip (Figure 6.35 (c)).

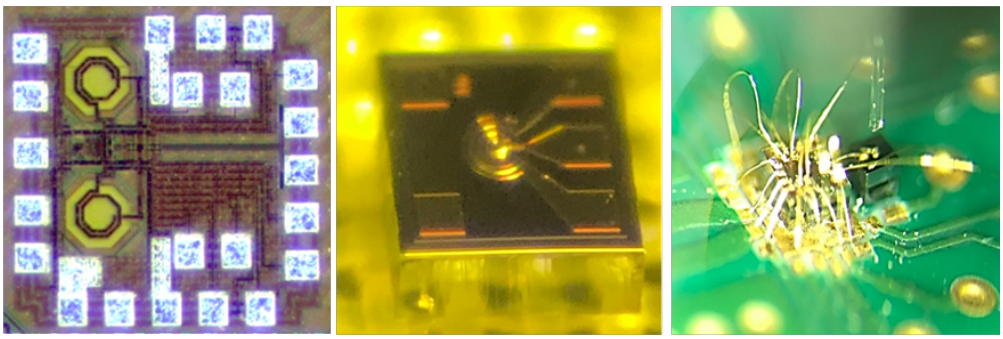

Figure 6.35: (a) Receiver chip micrograph, (b) external photodiode, (c) interface of the CMOS chip to the photodiode by wire bonds.

The measurement setup is shown in Figure 6.36. An arbitrary waveform generator (AWG) creates the 8Gbps DBPSK RF signal with 10 GHZ RF bandwidth with a pulse-shaping roll-off factor of 0.25. After amplification by a gain block, the RF signal is sent to the MZI optical intensity modulator to modulate the laser beam with 1dBm average power at 1550nm. A variable optical attenuator (VOA) is used before the EDFA to characterize the link tolerance to optical attenuation due to atmospheric effects. After the optical bandpass filter (to limit the ASE noise), another attenuator is used to model the possible long fiber loss. The RF current on the electrical receiver chip passes through the RGC and variable gain stages to provide differential RF voltage, which is then processed in MATLAB for demodulation and BER calculations.

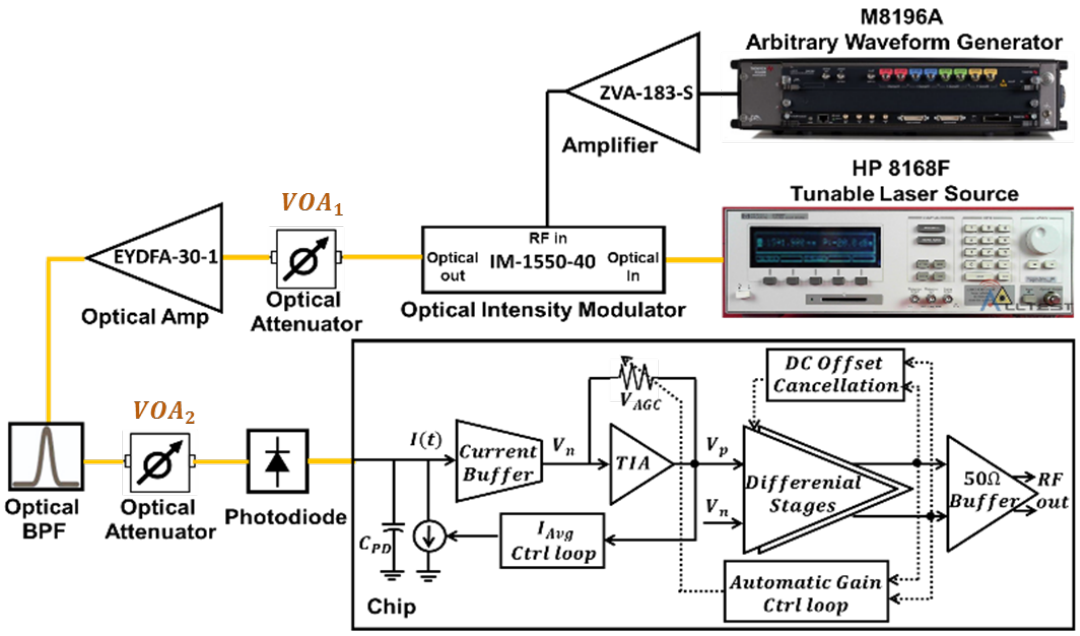

Figure 6.36: Measurement setup of the FSO receiver.

Figure 6.37 shows the measured AGC loop functionality. As the input current changes from 0.1mA to 2.4mA, differential gain varies over 21dB to limit output level variation to 5.2dB. The offset cancellation loop and the average current control loop work together to keep the DC value of the outputs near the optimum level, with a lower than ±15mV offset (Figure 6.38).

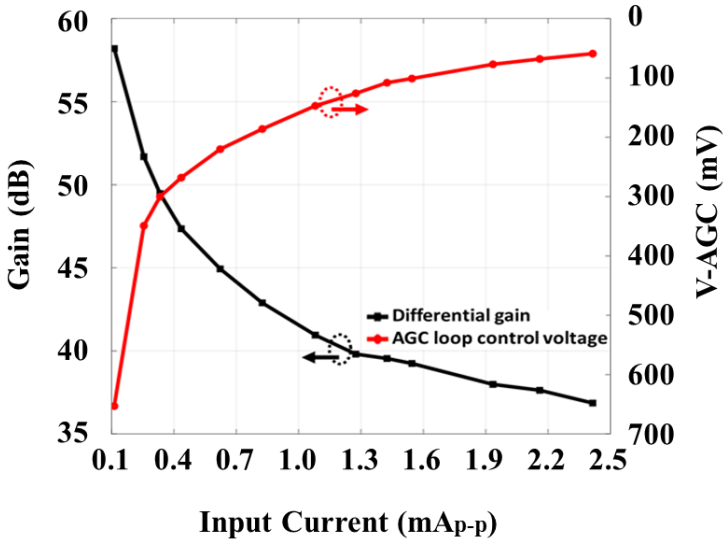

Figure 6.37: Measured response of the AGC loop.

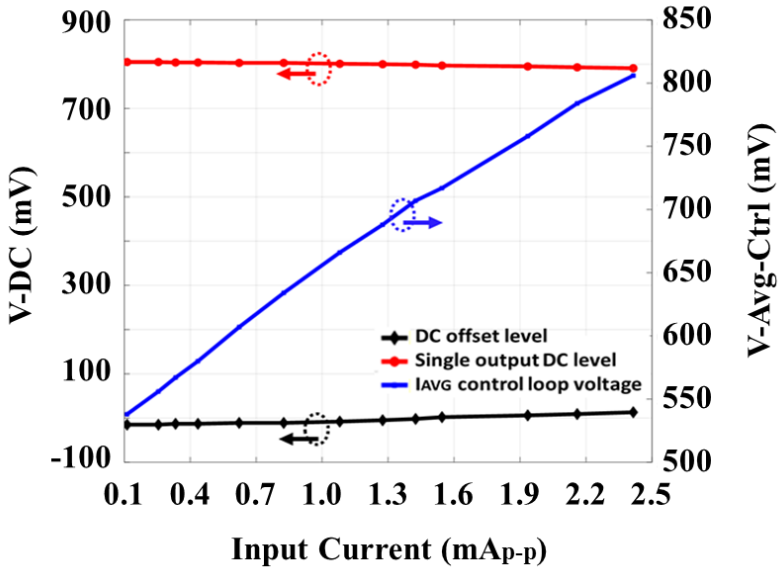

Figure 6.38: Measured response of the average current control loop and DC offset cancellation loops.

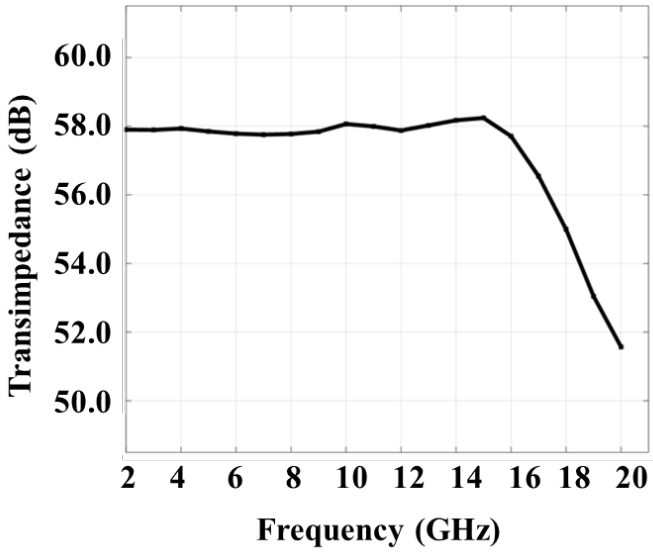

Figure 6.39: Measured frequency response of the CMOS chip.

The measured frequency response of the chip after compensating for the optical modulator's frequency response is shown in Figure 6.39. The measured 3dB frequency of the receiver is around 18GHz, with the flat frequency band of 3-13GHz suitable for the 8Gbps DBPSK signal transmission. The BER, as a function of the received power at the input of the optical

amplifier, is shown in Figure 6.40. For the received power of -28dBm and 8Gbps DBPSK data, the measured BER is $1 \times 1^{-4,}$ achieved without applying error correction codes. The BER improves as the data rate decreases or input power increases. Increasing the depth of intensity modulation (β) significantly improves CNR, as shown in (4). However, higher β leads to more nonlinearity in the optical modulator. By biasing the modulator at the optimum point to minimize second harmonic and filtering the higher order distortions, better error performance is achieved for a single-channel wideband signal.

Sample constellation diagrams and spectrum of the DPSK RF signals are shown in Figure 6.41. It is also shown that at the cost of higher required RF bandwidth for the same data rate of 8 Gbps, binary DPSK has superior BER performance compared to Quadrature DPSK. Table I compares this work with the previous RF over optics works, none of which include an integrated CMOS receiver. This design achieves a wide dynamic range operation and good BER while using non-coherent DPSK as subcarrier modulation. DPSK reduces complexity while having a 3dB CNR penalty compared to coherent PSK, which can be utilized to decrease BER further.

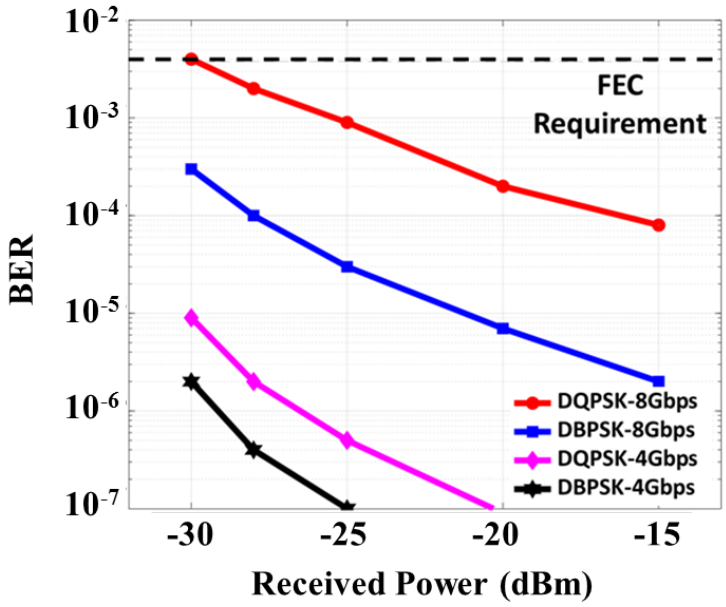

Figure 6.40: BER versus received optical power at different data rates and modulations.

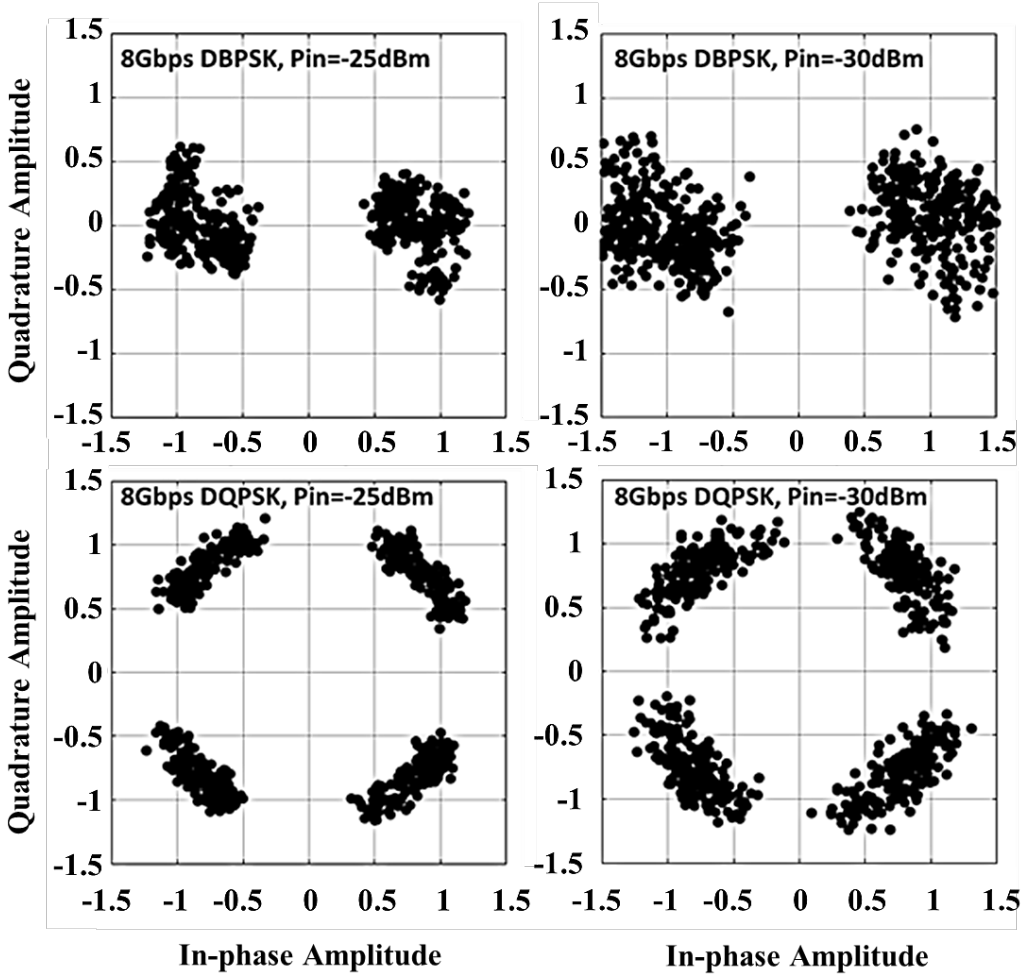

Figure 6.41: Constellation diagrams of the receiver for DBPSK and DQPSK modulations and 8Gbps data.

This chapter described an integrated optical receiver for RF over free-space optics, designed and implemented in a 28nm CMOS process. Using SIM and a direct detection scheme, high data rate optical communication is supported in a high-loss atmospheric channel. The receiver chip uses adaptive control loops to compensate for the atmospheric effects and extends the dynamic range. For a proof-of-concept demonstration, an 8Gbps non-coherent DPSK signal with an RF bandwidth of 10GHz is transmitted, resulting in a BER of 1×10^{-4} for a minimum received power of -30dBm and while consuming 19.2mW power at the receiver. The link performance is assessed by exposing the system to more than 26dB of optical loss, equivalent to 3.5km of free space distance under moderate visibility conditions.

Future work can improve BER by using a coherent modulation type at the subcarrier level or a subcarrier diversity scheme with a single optical front end and multiple RF channels.

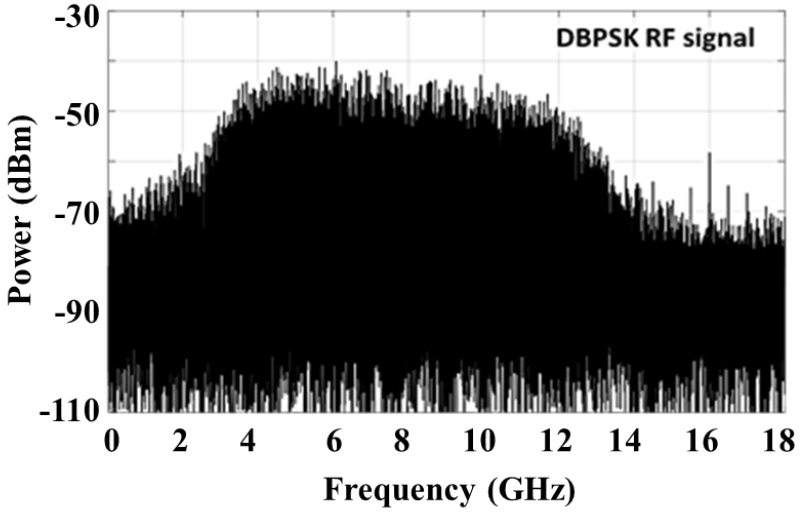

Figure 6.42: Measured spectrum of the DBPSK RF signal.

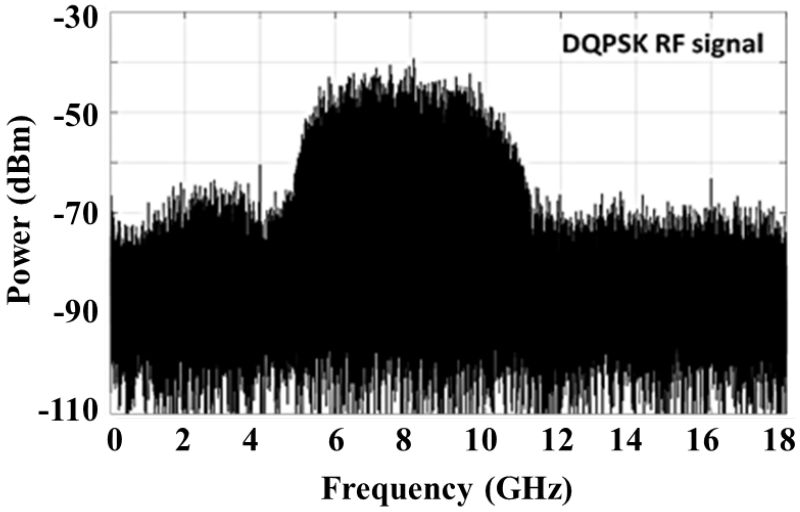

Figure 6.43: Measured spectrum of the DQPSK RF signal.

Table 6.1: Comparison of performance parameters of RF over optics systems

Ref.	Application	Modulation	Data Rate (Gbps)	Received Power	BER	Integrated Receiver	FOM
[93]	RoF	16QAM	4x2.5	-18 dBm	$1x10^{-3}$	No	0.63
[94]	RoF /RoFSO	SIM (64QAM)	0.6	-21 dBm	$2x10^{-3}$	No	0.075
[95]	mmW /RoFSO	SIM (16QAM)	4	-29 dBm	$1x10^{-5}$	No	3.2
This work	**RoFSO**	**SIM (DBPSK)**	**8**	**-28 dBm**	**$1x10^{-4}$**	**Yes**	**5.06**

Chapter 7

CONCLUSION

We, as humanity and our planet as our habitat, face new challenges that endanger us every day, from a fast-spreading pandemic that overwhelms the whole world's healthcare system to the devastating effects of global warming on our food and water resources and air quality. Despite the remarkable advances in various fields of science and technology, there is still a long road to pave for a truly portable and autonomous diagnostic and treatment solution for both medical and environmental applications. The key to achieving this goal is combining advances in multiple fields to open up new possibilities for device miniaturization and integrating the relevant functions. This dissertation presents a multidisciplinary integrated device for detecting and controlling biological elements/reactions based on fluorescence sensing. This device is the first of its kind to provide the necessary range of operating wavelengths to use the bacterial cells as natural biosensors and hence take advantage of the well-established tools in synthetic biology.

Using the CMOS process, replacing the bulky and expensive setup of the conventional fluorescence sensor with a portable solution is feasible. In this work, we show that the routing metal layers of the standard CMOS process, when designed in suitable nanostructures, can be used to manipulate electromagnetic fields to implement optical filtering in the wavelength of interest. The main limitation of the realized filters in the prior art, which limits their application in bacterial-based sensors, is the high loss of copper in the visible wavelength range. A new category of optical resonances is implemented in this work to minimize this metallic loss while realizing bandpass filters in the 600nm/700nm range. The lack of collimated light and focusing lenses requires the filters to be insensitive to the fluorescence's emission light's polarization and angle of arrival. Symmetrical cavity structures are proposed to achieve these requirements while satisfying the strict design rules of the CMOS process.

Even though the optical bandpass filters are achieved in the visible wavelength range and with a decent transmission level, the level of the resulted extinction ratio is not enough for most common fluorescent proteins with a very small Stokes shift. Therefore, an additional level of filtering is required, provided by a proposed bandpass photodiode design and by applying several techniques in the electrical domain. First, the sensor is designed fully differentially in both the footprint and the circuit design to make the remaining excitation light appear as a common mode signal which is rejected in the differential front end. Second, a digitally-controlled current source is implemented in the input node to draw the significant common mode signal to make the processing of the small differential signal more linear. Third, the circuit features low-leakage buffered switches to increase the circuit's sensitivity to the femto-amp level. Finally, the circuit provides a variable gain setting and correlated double sampling to reduce the front end's low-frequency noise components and offset.

Through comprehensive electrical, optical, and biological measurements, we characterized the sensor in terms of its responsivity, sensitivity, signal-to-noise ratio, and filters/photodiodes spectrums. The sensor can detect a signal amplitude of 1fA with better than 18dB SNR while consuming only 7mW of power. Several biological experiments, both static and dynamic, are performed to monitor the cell's growth behavior and their fluorescence expression dynamics. A proof of concept shows the sensor's feasibility in creating bidirectional communication between living cells and the CMOS chip.

In the last chapter of this dissertation, we present the design and implementation of an adaptive integrated receiver for transmitting RF over free space optics applications. The use of the atmosphere as the communication channel and optical wave as the signal carrier has advantages as follows. Such a system can be inherently very wideband since the strict regulation of the RF band does not apply to optical frequencies. The optical signal is immune to electromagnetic interference. It is very secure, and at the same time this like can be established in a short time and cost since there is no need for optical fiber infrastructures. Despite these benefits, the atmospheric link faces several challenges of distortions in the carrier beam. This work presents methods at the system level (modulation type) and circuit

level (adaptive automatic loops) to make such a link feasible while consuming low power and in a fully integrated way. The receiver is implemented in a 28nm CMOS process, and the measurement results show the successful transmission of 8Gbps data using differential PSK modulation with a bit error rate of 10^{-4} while receiving -28dBm received average power due to the atmospheric loss.

Future Directions

For the future development of the fluorescence sensor towards full technology maturity and massive point-of-care applications following improvements can be considered. First, a more efficient biological interface makes the seamless integration of the sensor and sample of interest user-friendly and reliable. A thin layer of PDMS can cover and protect the wire bonds of the chip, which enables using the hydrogels as bio-interface. Engineered reporter cells can be encapsulated in micron-size hydrogel bids to directly sit on surface of the sensor resulting in an increased sensitivity due to the reduction of the optical path.

For the device to be suitable for portable applications, reducing the power consumption of the sensor by optimizing the circuit blocks is a must. Furthermore, adding wireless data and power communication, and on-chip digitization is important for removing the external data acquisition unit and reducing overall size of the device to fit in a small ingestible pill. Another feature to consider is to make the VCCS tuning operation automatic, which can help find the optimum compensating current for the highest possible sensitivity in a short time.

In addition to healthcare applications, this device has so much potential in environmental sensing. In one such application, research is ongoing to use this technology for real-time monitoring of the bioavailable phosphorus (P) under the soil near the plant root. The P limitation can cause serious hardship for the plant to grow healthy, and therefore by using organic reporter bugs, efficient fertilization in the field can avoid product loss. In developing the sensor for this application, keeping the sensor low power while including the on-chip digitization and wireless data communication is more challenging. This is because the RF signal needs to travel through roughly 1 meter of soil, suffering high attenuation. Also, in

contrast to the healthcare application where the pill needs less than 24 hours of operation, under the soil sensor should survive weeks or even months on the included battery, necessitating a very low-power design. The other solution is to self-power the sensor through energy harvesting from biofuels which makes the operation of the sensor continuous without the need to replace the battery. Nonetheless, due to limited efficiency, the CMOS circuitry still needs to be carefully designed for optimum power consumption.

The other possible application of this sensor is to detect contaminations such as Arsenic which is toxic and can be present in unhealthy water. Experiments are ongoing to determine the minimum level of Arsenic that can be detected while the cells are in spores or vegetative states.

BIBLIOGRAPHY

[1] A. D. McNaught and A. Wilkinson, *Compendium of Chemical Terminology*, *2nd ed*, Oxford, UK: Blackwell Scientific Publications, 1997, Online version, 2019. [Online]. Available: https://goldbook.iupac.org/

[2] M. Zourob, S. Elwary, and A. P. F. Turner, *Principles of Bacterial Detection: Biosensors, Recognition Receptors, and Microsystems*. New York, NY, USA: Springer Science & Business Media, 2008.

[3] N. Bhalla, P. Jolly, N. Formisano, and P. Estrela, "Introduction to Biosensors," in *Essays Biochem*., vol. 60, no. 1, pp. 1-8, 2016.

[4] S. Scarano, S. Mariani and M. Minunni, "SPR-Based Affinity Biosensors as Innovative Analytical Devices," in *Journal of Lightwave Technology*, vol. 33, no. 16, pp. 3374-3384, 15 Aug.15, 2015.

[5] "About Chronic Diseases," National Center for Chronic Disease Prevention and Health Promotion, [Online]. Available: www.cdc.gov/chronicdisease/ about/index.

[6] L. Hong, *Nano Optical System-On-Chip in the Visible Range: From Biosensing to Security*, Doctoral Dissertation, Princeton University, 2021.

[7] Y. Yu, H. Y. Y. Nyein, W. Gao, and A. Javey, "Flexible Electrochemical Bioelectronics: The Rise of In Situ Bioanalysis," in *Advanced Materials*, vol. 32, no. 15, Aug. 2019.

[8] "Sixth Assessment Report, IPCC," Intergovernmental Panel on Climate Change, [Online]. Available: www.ipcc.ch/report/sixth-assessment-report-cycle/

[9] L. Hong, H. Li, H. Yang, and K. Sengupta, "Fully Integrated Fluorescence Biosensors On-Chip Employing Multi-Functional Nanoplasmonic Optical Structures in CMOS," in *IEEE J. Solid-State Circuits*, vol. 52, no. 9, pp. 2388–2406, Sep. 2017.

[10] H. Wang, Y. Chen, A. Hassibi, A. Scherer, and A. Hajimiri "A Frequency-Shift CMOS Magnetic Biosensor Array with Single-Bead Sensitivity and No External Magnet," in *IEEE Int. Solid-State Circuits Conf. (ISSCC) Dig. Tech. Papers*, Feb. 2009, pp. 438–439.

[11] I. H. Cho, D. H. Kim, and S. Park, "Electrochemical Biosensors: Perspective on Functional Nanomaterials for On-Site Analysis," in *Biomater. Res.* vol. 24, no. 6, Feb. 2020.

[12] G. Karki, "Biosensors: Components, Working Principle and Types", Molecular Biology, June 2020, [Online]. Available: https:// www.onlinebiologynotes.com/ biosensors-components-working-principle-and-types/

[13] D. Grieshaber, R. MacKenzie, J. Vörös, E. Reimhult, "Electrochemical Biosensors - Sensor Principles and Architectures," in *Sensors (Basel)*, vol. 8, no. 3, pp. 1400-1458, Mar. 2008.

[14] H. Li, X. Liu, L. Li, X. Mu, R. Genov, and A. J. Mason, "CMOS Electrochemical Instrumentation for Biosensor Microsystems: A Review," in *Sensors*, vol. 17, no. 1, Dec. 2016.

[15] R. Luxton, "Magnetic Biosensors," [Online]. Available: https://www.mdpi.com/ journal/biosensors/special issues/magnetic biosensors.

[16] G. Li, V. Joshi, R. L. White, S. X. Wang, J. T. Kemp, C. Webb, and S. Sun, "Detection of Single Micron-Sized Magnetic Bead and Magnetic Nanoparticles using Spin Valve Sensors for Biological Applications," in *Journal of applied physics*, vol. 93, no. 10, pp. 7557-7559, May. 2003.

[17] S. J. Han, H. Yu, B. Murmann, and N. Pourmand, "A High-Density Magnetoresistive Biosensor Array with Drift-Compensation Mechanism," in *IEEE Int. Solid-State Circuits Conf. Dig. Tech. Papers*, pp. 168-169, 2007.

[18] P. Liu, K. Skucha, M. Megens, and B. Boser, "A CMOS Hall-Effect Sensor for the Characterization and Detection of Magnetic Nanoparticles for Biomedical Applications," in *IEEE Trans. Magn.*, vol. 47, no. 10, pp. 3449-3451, 2011.

[19] Y. Liu, N. Sun, H. Lee, R. Weissleder, and D. Ham, "CMOS Mini Nuclear Magnetic Resonance System and Its Application for Biomolecular Sensing," in *IEEE Int. Solid-State Circuits Conf. Dig. Tech. Papers*, pp. 140-602, 2008.

[20] P.A. Besse, G. Boero, M. Demierre, V. Pott, and R. Popovic, "Detection of a Single Magnetic Microbead Using a Miniaturized Silicon Hall Sensor," in *Appl. Phys. Lett*., vol. 80, no. 22, pp. 4199-4201, Jun. 2002.

[21] O. Damborský, J. Švitel, J. Katrlík, "Optical Biosensors," in *Essays Biochem*., vol. 60, no.1, pp. 91-100, 2016.

[22] S. Samiksha, "Biosensors: Types and General Features of Biosensors," [Online]. Available: https://www.yourarticlelibrary.com/science/biosensors-types-and-general-features-of-biosensors/23331

[23] B. Jang, P. Cao, A. Chevalier, A. Ellington, and A. Hassibi, "A CMOS Fluorescent-Based Biosensor Microarray," in *IEEE Int. Solid-State Circuits Conf. Dig. Tech. Papers*, 436-437, 2013.

[24] R. R. Singh, D. Ho, A. Nilchi, G. Gulak, P. Yau and R. Genov, "A CMOS/Thin-Film Fluorescence Contact Imaging Microsystem for DNA Analysis," in *IEEE Trans. Circuits Syst. I: Regular Papers*, vol. 57, no. 5, pp. 1029-1038, May 2010.

[25] D. Ho, M. O. Noor, U. J. Krull, G. Gulak and R. Genov, "CMOS Tunable-Wavelength Multi-Color Photogate Sensor", in *IEEE Trans. on Biomed. Circuits Syst*., vol. 7, no. 6, pp. 805-819, Dec. 2013.

[26] E. A. Rodriguez, R. E. Campbell, J. Y. Lin, M. Z. Lin, A. Miyawaki, A. E. Palmer, X. Shu, J. Zhang, and R. Y. Tsien, "The Growing and Glowing Toolbox of Fluorescent and Photoactive Proteins," in *Trends Biochem. Sci.*, vol. 42, no. 2, pp. 111-129, Feb. 2017.

[27] T. C. D. Huang, S. Sorgenfrei, P. Gong, R. Levicky and K. L. Shepard, "A 0.18um CMOS Array Sensor for Integrated Time-Resolved Fluorescence Detection," in *IEEE J. Solid-State Circuits*, vol. 44, no. 5, pp. 1644-1654, May 2009.

[28] H. J. Yoon, S. Itoh and S. Kawahito, "A CMOS Image Sensor with In-Pixel Two-Stage Charge Transfer for Fluorescence Lifetime Imaging," in *IEEE Trans. Elec. Dev.*, vol. 56, no. 2, pp. 214-221, Feb. 2009.

[29] G. Patounakis, K. L. Shepard and R. Levicky, "Active CMOS Array Sensor for Time- Resolved Fluorescence Detection," in *IEEE J. Solid-State Circuits*, vol. 41, no. 11, pp. 2521-2530, Nov. 2006.

[30] D. Stoppa, D. Mosconi, L. Pancheri and L. Gonzo, "Single-Photon Avalanche Diode CMOS Sensor for Time-Resolved Fluorescence Measurements," in *IEEE Sensors J.*, vol. 9, no. 9, pp. 1084-1090, Sept. 2009.

[31] A. Manickam, A. Chevalier, M. McDermott, A. D. Ellington, and A. Hassibi, "A CMOS Electrochemical Impedance Spectroscopy (EIS) Biosensor Array," in *IEEE Trans. Biomed. Circuits Syst.*, vol. 4, no. 6, pp. 379-390, Dec. 2010.

[32] P. M. Levine, P. Gong, R. Levicky, and K. L. Shepard, "Active CMOS Sensor Array for Electrochemical Biomolecular Detection," in *IEEE J. Solid-State Circuits*, vol. 43, no. 8, pp. 1859-1871, Aug. 2008.

[33] D. A. Hall, R. S. Gaster, K. A. Makinwa, S. X. Wang, and B. Murmann, "A 256 Pixel Magneto-Resistive Biosensor Microarray in 0.18 μm CMOS," in *IEEE J. Solid-State Circuits*, vol. 48, no. 5, pp. 1290-1301, May. 2013.

[34] K. N. M. Daeffler, J. D. Galley, R.U. Sheth, L. C. Ortiz-Velez, C. O. Bibb, N. F. Shroyer, R. A. Britton, and J. J. Tabor, "Engineering Bacterial Thiosulfate and Tetrathionate Sensors for Detecting Gut Inflammation," in *Mol. Syst. Biol.*, vol. 13 (4):923, Apr. 2017.

[35] D. T. Riglar, T. W. Giessen, M. Baym, S. J. Kerns, M. J. Niederhuber, R. T. Bronson, J. W. Kotula, G. K. Gerber, J. C. Way, and P. A. Silver, "Engineered Bacteria Can Function in The Mammalian Gut Long-Term as Live Diagnostics of Inflammation," in *Nat. Biotechnol.,* vol. 35(7), pp. 653-658, Jul. 2017.

[36] M. Zourob, S. Elwary, and A. P. F. Turner, *Principles of Bacterial Detection:*

Biosensors, Recognition Receptors, and Microsystems. New York, NY, USA: Springer Science & Business Media, 2008.

[37] S. Leth, S. Maltoni, R. Simkus, B. Mattiasson, P. Corbisier, I. Klimant, O. S. Wolfbeis, and E. Csöregi, "Engineered Bacteria Based Biosensors for Monitoring Bioavailable Heavy Metals," in *Electroanalysis: An International Journal Devoted to Fundamental and Practical Aspects of Electroanalysis*, vol. 14, no. 1, pp. 35-42, Jan. 2002.

[38] S. Sharma, A. Telikicherla, G. Ding, F. Aghlmand, A. H. Talkhooncheh, M. G. Shapiro, and A. Emami, "Wireless 3D Surgical Navigation and Tracking System With 100μm Accuracy Using Magnetic-Field Gradient-Based Localization," in *IEEE Trans. Med. Imaging*., vol. 40, no. 8, pp. 2066-2079, Jul. 2021.

[39] A. Turner, I. Karube, and G. S. Wilson, *Biosensors: Fundamentals and Applications*. Oxford University Press, 1987.

[40] C. P. Zschiedrich, V. Keidel, and H. Szurmant, "Molecular Mechanisms of Two-Component Signal Transduction," in *J. Mol. Biol.*, vol. 428, no. 19, pp. 3752-3775, Sep. 2016.

[41] M. Moraskie, M. H. O. Roshid, G. O'Connor, E. Dikici, J.-M. Zingg, S. Deo, and S. Daunert, "Microbial Whole-Cell Biosensors: Current Applications, Challenges, and Future Perspectives," in *Biosensors and Bioelectronics*, vol. 191, Nov. 2021.

[42] A. Ivask, M. Virta, and A. Kahru, "Construction and Use of Specific Luminescent Recombinant Bacterial Sensors for the Assessment of Bioavailable Fraction of Cadmium, Zinc, Mercury, and Chromium in the Soil," in *Soil Biol. Biochem.*, vol. 34, no. 10, pp. 1439-1447, Oct. 2002.

[43] P. Banerjee, S. Kintzios, and B. Prabhakarpandian, "Biotoxin Detection Using Cell-Based Sensors," in *Toxins*, vol. 5, no. 12, pp. 2366-2383, Nov. 2013.

[44] G. Patterson, R. N. Day, and D. Piston, "Fluorescent Protein Spectra," in *J. Cell. Sci*., vol. 114, no.5, pp. 837–838, Jan. 2001.

[45] LibreTexts Chemistry, Jan 2023, Fluorescence [Online]. Available: chem.libretexts.org

[46] L. Song, E. J. Hennink, I. T. Young, and H. J. Tanke, "Photobleaching Kinetics of Fluorescein in Quantitative Fluorescence Microscopy," in *Biophysical Journal,* vol. 68, pp. 2588-2600, Jun. 1995.

[47] L. R. Joseph, *Principles of Fluorescence Spectroscopy*. New York, NY, USA: Springer, 2013.

[48] F. Widdel, "Theory and Measurement of Bacterial Growth," in *Grundpraktikum Mikrobiologie*, vol. 4.11, pp. 1-11, May. 2007.

[49] K. Saito, T. Nagai, "Recent Progress in Luminescent Proteins Development," in *Curr Opin Chem Biol*., vol. 27, pp. 45-51, Aug. 2015.

[50] Q. Liu, M. Jimenez, M. E. Inda, A. Riaz, T. Zirtiloglu, A. P. Chandrakasan, T. K. Lu, G. Traverso, P. Nadeau, and R. T. Yazicigil, "A Threshold-Based Bioluminescence Detector With a CMOS-Integrated Photodiode Array in 65 nm for a Multi-Diagnostic Ingestible Capsule," in *IEEE J. Solid-State Circuits*, vol. 58, no. 3, pp. 838-851, March 2023.

[51] D. Del Vecchio and R. M. Murray, *Biomolecular Feedback Systems*. Princeton, NJ, USA: Princeton Scholarship Online, 2017.

[52] M. T. Q. Duong, Y. Qin, S. H. You, and J. J. Min, "Bacteria-Cancer Interactions: Bacteria-Based Cancer Therapy," in *Exp. Mol. Med*., vol. 51, pp. 1–15, Dec. 2019.

[53] K. Ghoreschi, P. Thomas, S. Breit, M. Dugas, R. Mailhammer, W. van Eden, R. van der Zee, T. Biedermann, J. Prinz, M. Mack, and U. Mrowietz, "Interleukin-4 Therapy of Psoriasis Induces Th2 Responses and Improves Human Autoimmune Disease," in *Nat. Med*., vol. 9, pp. 40–46, Jan. 2003.

[54] S. Sharma, K. B. Ramadi, N. H. Poole, S. S. Srinivasan, K. Ishida, J. Kuosmanen, J. Jenkins, F. Aghlmand, M. B. Swift, M. G. Shapiro, G. Traverso, and, A. Emami, "Location-Aware Ingestible Microdevices for Wireless Monitoring of

Gastrointestinal Dynamics," in *Nat Electron*, Feb. 2023.

[55] J. Ru, Y. Huo, and Y. Yang, "Microbial Degradation and Valorization of Plastic Wastes," in *Front. Microbiol*., vol. 11, Apr. 2020.

[56] X. Xu, W. Liu, S. Tian, W. Wang, Q. Qi, P. Jiang, X. Gao, F. Li, H. Li, and H. Yu, "Petroleum Hydrocarbon-Degrading Bacteria for the Remediation of Oil Pollution Under Aerobic Conditions: A Perspective Analysis," in *Front. Microbiol*., vol. 9, Dec. 2018.

[57] D. M. Shcherbakova, M. A. Hink, L. Joosen, T. W. Gadella, and V. V. Verkhusha, "An Orange Fluorescent Protein with a Large Stokes Shift for Single-Excitation Multicolor FCCS and FRET Imaging," in *J. Amr. Chem. Soc*., vol. 134, pp. 7913-7923, Apr. 2012.

[58] K. D. Piatkevich, E. E. Jung, C. Straub, C. Linghu, D. Park, H. J. Suk, D. R. Hochbaum, D. Goodwin, E. Pnevmatikakis, N. Pak, and T. Kawashima, "A Robotic Multidimensional Directed Evolution Approach Applied to Fluorescent Voltage Reporters," in *Nat. Chem. Biol*., vol. 14, pp. 352-360, Feb. 2018.

[59] R. Y. Tsien, "The Green Fluorescent Protein," *Annual Review of Biochemistry,* vol. 67, no.1, pp. 509-544, 1998.

[60] Q. Wang, Z. Zhu, H. Gu, and Q. Tan, "Angle-Tolerant Hybrid Plasmonic Blue Filter with Polarization-Insensitivity and High Transmission," in *Optics Comm*., vol. 427, pp. 457-461, Nov. 2018.

[61] C. Yang, W. Shen, J. Zhou, X. Fang, D. Zhao, X. Zhang, C. Ji, B. Fang, Y. Zhang, X. Liu, and L. J. Guo, "Angle Robust Reflection/Transmission Plasmonic Filters Using Ultrathin Metal Patch Array," in *Adv. Opt. Mater*., vol. 4, no. 12, pp. 1981-1986, Sept. 2016.

[62] T. Wood, M. Naffouti, J. Berthelot, T. David, J. B. Claude, L. Métayer, A. Delobbe, L. Favre, A. Ronda, I. Berbezier, and N. Bonod, "All-Dielectric Color Filters Using SiGe-Based Mie Resonator Arrays," in *ACS Photonics*, vol. 4, no. 4, pp. 873-883, Mar. 2017.

[63] F. Shen, Q. Kang, J. Wang, K. Guo, Q. Zhou, and Z. Guo, "Dielectric Metasurface-Based High-Efficiency Mid-Infrared Optical Filter," in *Nanomaterials,* vol. 8, no. 938, Nov. 2018.

[64] Y. Horie *et al*., "Visible Wavelength Color Filters Using Dielectric Subwavelength Gratings for Backside-Illuminated CMOS Image Sensor Technologies," in *Nano. Lett*., vol. 17, no. 5, pp. 3159−3164, May. 2017.

[65] F. Aghlmand *et al*., "A 65nm CMOS Living-Cell Dynamic Fluorescence Sensor with 1.05fA Sensitivity at 600/700nm Wavelengths," in *IEEE Int. Solid-State Circuits Conf. (ISSCC) Dig. Tech. Papers*, Feb 2023, pp. 311–313.

[66] S. A. Maier, *Plasmonics: Fundamentals and Applications,* Berlin Heidelberg: Springer, 2007.

[67] S. A. Maier and H. A. Atwater, "Plasmonics: Localization and Guiding of Electromagnetic Energy in Metal/Dielectric Structures," in *J. Appl. Phys.*, vol. 98, 011101, Jul. 2005.

[68] F. Gildas and Y. Dan "Review of Nanostructure Color Filters," in *J. Nanophotonics,* vol. 13, no. 2, Jun. 2019.

[69] S. A. Maier, "Plasmonics: The Promise of Highly Integrated Optical Devices," in *IEEE J. Sel. Top. Quantum Electron*., vol. 12, no. 6, pp. 1671-1677, Nov/Dec. 2006.

[70] J. Jiang, X. Wang, S. Li, F. Ding, N. Li, S. Meng, R. Li, J. Qi, Q. Liu, and G. L. Liu, "Plasmonic Nano-Arrays for Ultrasensitive Bio-Sensing," in *Nanophotonics,* vol. 7, no. 9, pp. 1517-1531, Aug. 2018.

[71] A. S. M. Z. Kausar, A. W. Reza, T. A. Latef, M. H. Ullah, and M. E. Karim, "Optical Nano Antennas: State of the Art, Scope and Challenges as a Biosensor along with Human Exposure to Nano-Toxicology," in *Sensors,* vol. 15, no. 4, pp. 8787-8831, Apr. 2015.

[72] M. Février, P. Gogol, J. M. Lourtioz, and B. Dagens, "Metallic Nanoparticle

Chains on Dielectric Waveguides: Coupled and Uncoupled Situations Compared," in *Optics Express*, vol. 21, no. 21, pp. 24504–24513, Oct. 2013.

[73] Y. H. Jang, Y. J. Jang, S. Kim, L. N. Quan, K. Chung, and D. H. Kim, "Plasmonic Solar Cells: From Rational Design to Mechanism Overview," in *Chem. Rev*. vol. 116, no. 24, pp. 14982–15034, Dec. 2016.

[74] D. Fleischman, L. A. Sweatlock, H. Murakami, and H. Atwater, "Hyper-Selective Plasmonic Color Filters," in *Opt. Express*, vol. 25, no. 22, pp. 27386-27395, Oct. 2017.

[75] Y. Xu, J. Yue, M. Wang, X. Sun, and D. Zhang, "Tunable Narrow-Band Filter Based on Long-Range Surface Plasmon Polariton Waveguide Bragg Grating," in *Photonics*, vol. 9, no. 5: 344, May. 2022.

[76] H. Liu and Z. Sun, "Narrow-Band, Low-Sideband Plasmonic Filter of Asymmetric Bi-Layer Metallic Nanoslit Arrays," in *Opt. Express*, vol. 29, no. 9, pp. 13590-13599, Apr. 2021.

[77] W. L. Barnes, A. Dereux, and T. W. Ebbesen, "Surface Plasmon Subwavelength Optics," in *Nature*, vol. 424, pp. 824–830, Aug. 2003.

[78] S. Pi, X. Zeng, N. Zhang, D. Ji, B. Chen, H. Song, A. Cheney, Y. Xu, S. Jiang, D. Sun, and Y. Song, "Dielectric-Grating-Coupled Surface Plasmon Resonance from the Back Side of the Metal Film for Ultrasensitive Sensing," in *IEEE Photon. J.*, vol. 8, no. 1, pp. 1-7, Feb. 2016.

[79] E. Popov, S. Enoch, G. Tayeb, M. Neviere, B. Gralak, and N. Bonod, "Enhanced Transmission Due to Non-plasmon Resonances in One and Two-D Gratings," in *Applied Optics*, vol. 43, no. 5, pp. 999-1008, 2004.

[80] M. Neviere, E. Popov, R. Reinisch, and G. Vitrant, *Electromagnetic Resonances in Nonlinear Optics*, Netherlands: CRC Press, 2000.

[81] W. S. C. Chang, *Principles of Optics for Engineers: Diffraction and Modal Analysis.* Cambridge: Cambridge University Press, 2015.

[82] I. Avrutsky, E. M. Smith, S. Vangala, R. Gibson, J. R. Hendrickson, and J. W. Cleary, “Angle-and Polarization-Independent Mid-Infrared Narrowband Optical Filters Using Dense Arrays of Resonant Cavities,” in *Opt. Express*, vol. 27, no. 26, pp. 37481-37493, Dec. 2019.

[83] J. Zhou and L. J. Guo, “Achieving Angle-Insensitive Spectrum Filter with the Slit Nanoresonator Array Structure,” in *J. Nanophotonics*, vol. 9, Dec. 2015.

[84] A. Atef *et al*., “CMOS Transimpedance Amplifiers for Biomedical Applications: A Comparative Study," in *IEEE Circuits and Systems Magazine,* vol. 20, no.1, pp. 12-31, 2020.

[85] N. Yazdi, H. Kulah, and K. Najafi, “Precision Readout Circuits for Capacitive Microaccelerometers,” in *Sensors*, pp. 28-31, 2004.

[86] D. Van Labeke, D. Gérard, B. Guizal, F. I. Baida, and L. Li, “An Angle-Independent Frequency Selective Surface in the Optical Range,” in *Opt. Express*, vol. 14, no. 25, pp. 11945-11951, Sep. 2006.

[87] M. Atef and H. Zimmermann, “Integrated Photodiodes in Nanometer CMOS Technologies,” in *Optoelectronic Circuits in Nanometer CMOS Technology*, vol. 55, Springer, Cham, 2016.

[88] M. W. Seo, K. Kagawa, K. Yasutomi, Y. Kawata, N. Teranishi, Z. Li, I. A. Halin, and S. Kawahito, “A 10 ps Time-Resolution CMOS Image Sensor with Two-Tap True-CDS Lock-in Pixels for Fluorescence Lifetime Imaging,” in *IEEE J. Solid-State Circuits*, vol. 51, no. 1, pp. 141–154, Jan. 2016.

[89] N. C. Shaner, R. E. Campbell, P. A. Steinbach, B. N. Giepmans, A. E. Palmer, and R. Y. Tsien, “Improved Monomeric Red, Orange and Yellow Fluorescent Proteins Derived from Discosoma sp. Red Fluorescent Protein,” in *Nat. Biotechnol*., vol. 22, pp. 1567-1572, Nov. 2004.

[90] J. D. Pédelacq, S. Cabantous, T. Tran, T. C. Terwilliger, and G. S. Waldo, “Engineering and Characterization of a Superfolder Green Fluorescent Protein,” in *Nat. Biotechnol*., vol. 24, pp. 79-88, Sep. 2006.

[91] E. P. Papageorgiou, B. E. Boser, and M. Anwar, “Chip-Scale Angle-Selective Imager for In Vivo Microscopic Cancer Detection,” in *IEEE TBioCAS*, vol. 14, no. 1, pp. 91-103, Feb. 2020.

[92] F. Aghlmand *et al*., “An 8Gbps Adaptive Receiver for RF over FSO in 28nm CMOS,” in *2020 15th European Microwave Integrated Circuits Conference (EuMIC)*, Jan. 2021, pp. 49-52.

[93] X. Chen and J. Yao, "Data Rate Quadrupled Coherent Microwave Photonic Link," in *IEEE Photonics Technology Letters*, vol. 29, no. 13, pp. 1071-1074, 1 July1, 2017.

[94] J. Bohata *et al*., "24–26 GHz Radio-Over-Fiber and Free-Space Optics for Fifth-Generation Systems," in *Opt. Lett.*, vol. 43, no. 5, pp. 1035–1038, Mar. 2018.

[95] J. Zhang *et al*., "Fiber–Wireless Integrated Mobile Backhaul Network Based on a Hybrid Millimeter-Wave and Free-Space-Optics Architecture with an Adaptive Diversity Combining Technique, " in *Opt. Lett*., vol. 41, no. 9, pp. 1909–1912, 2016.

[96] Z. Xiaoming, and J. M. Kahn, “Free-Space Optical Communication Through Atmospheric Turbulence Channels,” in *IEEE Transactions on communications*, vol. 50, no. 8, pp. 1293-1300, Aug. 2002.

[97] K. Sunilkumar et al., “Free Space Optical Communication System Through Turbid Media with Pointing Errors,” in *Applications of Lasers for Sensing and Free Space Communications*. Optica Publishing Group, 2018.

[98] H. Kaushal, and G. Kaddoum, “Optical Communication in Space: Challenges and Mitigation Techniques,” in *IEEE Communications Surveys & Tutorials,* vol. 19, no.1, pp. 57-96, 2016.

[99] C. Pernechele, “Imaging | Adaptive Optics,” in *Encyclopedia of Modern Optics*, B. Guenther and D. Steel, eds.,1st ed. (Elsevier Academic, 2005),

[100] R. K. Tyson, and B. W. Frazier, *Principles of Adaptive Optics*. CRC press, 2022.

[101] D. Florian, “Scintillation Loss in Free-Space Optic IM/DD Systems,” in *Free-space laser communication technologies XVI*, vol. 5338, SPIE, 2004.

[102] M. C. Gökçe, and Y. Baykal, “Aperture Averaging and BER for Gaussian Beam in Underwater Oceanic Turbulence," in *Optics Communications*, vol. 410, pp. 830-835, 2018.

[103] S. S. Saket, S. G. Suresh, “Diversity Technique for a Free Space Optical Communication System: A Survey Report,” in *International Journal of Optical Sciences*, vol. 5, no. 2, 2019.

[104] D. Giggenbach and A. Shrestha, “Atmospheric Absorption and Scattering Impact on Optical Satellite-Ground Links,” in *International Journal of Satellite Communications and Networking*, vol. 40, no. 2, pp. 157-176, Oct. 2021.

[105] A. Barbieri *et al*., “OFDM Versus Single-Carrier Transmission for 100 Gbps Optical Communication,” in *Journal of Lightwave Technology,* vol. 28, no. 17, pp. 2537-2551, 2010.

[106] S. Kumar, S. Sharma, and S. Dahiya. "WDM-Based 160 Gbps Radio Over Fiber System with the Application of Dispersion Compensation Fiber and Fiber Bragg Grating," in *Frontiers in Physics,* vol. 9, 2021.

[107] L. Sharan, V, M. Agrawal, and V. K. Chaubey, “Performance Evaluation and Nonlinear Mitigation Through DQPSK Modulation in 32× 40 Gbps Long-Haul DWDM Systems," in *Journal of Optical Communications,* vol. 38, no. 3, pp. 297-307, 2017.

[108] G. Kweon, “Noise Figure of Optical Amplifiers,*”* in *Journal of Korean Phy. Soc*., vol. 41, no. 5, pp. 617-628, Nov. 2002.

[109] T. Kawanishi, “Precise Optical Modulation and Its Application to Optoelectronic Device Measurement,” in *Photonics*, vol. 8, no. 5, May. 2021.

[110] H. Taki, S. Azou, A. Hamié, A. Housseini, A. Alaeddine, A. Sharaiha, "On Optimizing the Operating Conditions of a Mach-Zehnder Modulator for IR-UWB

over Fiber Transmission," in *2015 5th International Conference on Digital Information and Communication Technology and Its Applications, DICTAP,* Apr. 2015.

[111] J. Bowers and H. F. Chou, "Optical Communication Systems | Wavelength Division Multiplexing," in *Encyclopedia of Modern Optics*, pp. 433-440, 2005.

[112] B. Razavi, *Design of Integrated Circuits for Optical Communications*, 1st ed. New York, NY, USA: McGraw-Hill, 2003.

[113] I. Ozkaya *et al*., "A 64-Gb/s 1.4-pJ/b NRZ Optical Receiver Data-Path in 14-nm CMOS FinFET," in *IEEE Journal of Solid-State Circuits*, vol. 52, no. 12, pp. 3458-3473, Dec. 2017.

[114] E. M. Cherry and D. E. Hooper, "The Design of Wide-Band Transistor Feedback Amplifiers," in *Proc. Inst. Electr. Eng.*, vol. 110, no. 2, pp. 375- 389, Feb. 1963.